8-9-2022

The Spectral Energy Distributions of Active Galactic Nuclei with Direct Black Hole Mass Measurements

Rachael Merritt

The Spectral Energy Distributions of Active Galactic Nuclei with Direct Black Hole Mass Measurements

by

Rachael L. Merritt

Under the Direction of Misty C. Bentz, PhD

ABSTRACT

Active galactic nuclei (AGNs) are powered by accretion of material onto their central supermassive black holes and are unique in that they emit radiation across the entire electromagnetic spectrum. Spectral energy distributions (SEDs) allow for a comparison of the energy that is emitted in each wavelength regime. Our goal is to construct the most accurate multi-wavelength SEDs by reexamining the near-IR to X-ray SEDs of 23 AGNs with reverberation mapped (RM) black hole mass measurements. These SEDs will allow us to constrain measurements, such as bolometric luminosity and accretion rate and, in turn, these measurements can be used to better understand physical processes of AGNs and how they influence the host galaxy. To improve on previous studies, this set of SEDs consists of simultaneous optical/UV/X-ray data taken by *XMM-Newton* and is supplemented by ground-based near-IR data to constrain the red tail. Using two-dimensional decompositions of high-resolution *Hubble Space Telescope* images, combined with galaxy spectral templates, we constrain and remove the host galaxy contribution and focus the SEDs on the accretion powered AGN flux. We also consider the impacts of internal reddening and the effects

of broad and narrow line region emission. Finally, given the highly variable nature of AGNs, we examine 4 objects from this sample with 200-300 simultaneous optical/UV/X-ray *Neil Gehrels Swift Observatory* observations and quantify how variability impacts the shape of the SEDs and the scatter in measurements of bolometric luminosity and accretion rate.

INDEX WORDS: Observational astronomy, Seyfert galaxies, Active galactic nuclei, Supermassive black holes, Spectral energy distributions

The Spectral Energy Distributions of Active Galactic Nuclei with Direct Black Hole Mass Measurements

by

Rachael L. Merritt

A Dissertation Submitted in Partial Fulfillment of the Requirements of

Doctor of Philosophy

in the College of Arts and Sciences

Georgia State University

2022

The Spectral Energy Distributions of Active Galactic Nuclei with Direct Black Hole Mass Measurements

by

Rachael L. Merritt

Committee Chair:	Misty C. Bentz
Committee:	D. Michael Crenshaw
	Edward M. Cackett
	Russel J. White
	Merida Batiste

Electronic Version Approved:

Office of Graduate Studies

College of Arts and Sciences

Georgia State University

August 2022

DEDICATION

I dedicate this dissertation to every person who has helped me reach this point. It would have been an impossible journey without all of the love and encouragement.

ACKNOWLEDGEMENTS

RLM and MCB gratefully acknowledge support from the NSF through grant AST-2009230. RLM gratefully acknowledges the support from the from the Georgia State University Graduate School through the Provost's Disseration Fellowship, as well as the Georgia Space Grant Consortium for their support through the GSGC Fellowship.

This work is based on observations obtained with XMM-Newton, an ESA science mission with instruments and contributions directly funded by ESA Member States and NASA. This work is based on observations obtained as part of the VISTA Hemisphere Survey, ESO Program, 179.A-2010 (PI: McMahon). We acknowledge the use of public data from the Swift data archive. This research has made use of the VizieR catalogue access tool, CDS, Strasbourg, France (Ochsenbein et al., 2000). This research has made use of the NASA/IPAC Extragalactic Database (NED), which is funded by the National Aeronautics and Space Administration and operated by the California Institute of Technology.

I would like to thank my colleagues in the Department of Physics and Astronomy, as well as Team Bentz members present and past. I would like to thank Kolja, Renee, Ben, and all of my friends and family for their unwavering support. I would like to thank my committee members, Drs. Merida Batiste, Russel White, Edward Cackett, and Mike Crenshaw for the time and care that you put into helping me reach this milestone.

Finally, I would like to thank my advisor, Professor Misty Bentz. Your intellect, kindness, and dedication to science and your students are immeasurable. I will never be able to express the amount of gratitude that I have for the time we have spent together.

TABLE OF CONTENTS

LIST OF TABLES

LIST OF FIGURES

Chapter 1

INTRODUCTION

1.1 *Active Galactic Nuclei - A History*

In the center of nearly every galaxy, there is a supermassive black hole (SMBH). Some of these black holes are quiescent, while others are actively accreting material. These active systems are known as Active Galactic Nuclei (AGNs). Though we now understand that SMBHs and their host galaxies coevolve (Heckman & Best, 2014), it took two separate journeys to reach this understanding - one to understand galaxies, and the other to understand black holes.

At the start of the 20th century the quest to determine the size of the Universe and how 'spiral nebulae' fit into that universe was in full swing. In 1909, Edward Fath observed a collection of spiral nebulae and globular clusters at Lick Observatory to 'test the correctness [...] that the spectra of the spiral nebulae are continuous and to increase our knowledge of these spectra in any manner possible' (Fath, 1909). What he found when he observed the spectrum of NGC 1068 was a composite spectrum containing both absorption and emission features. He noted emission features at wavelengths of 3733Å, 3878Å, 4363Å, 4959Å, and 5007Å (corresponding to [OII], [NeIII], and [OIII]; Kraemer & Crenshaw 1999), as well as indication of Hβ emission. Vesto Slipher confirmed the presence of these lines in 1913 and observed NGC 1068 again in 1917 at Lowell Observatory (Slipher, 1917) with a smaller slit. He determined the emission lines were not images of the slits, but rather small disks, meaning he was viewing spatially resolved emission from the object. He even observed evidence of rotation. The question about the place of spiral nebulae in the Universe came to a head in the 1920s. The Great Debate between Harlow Shapley and Heber Curtis

occurred in April 1920, with Shapley arguing that the spiral nebulae were small and inside the Milky Way, while Curtis argued for Immanuel Kant's 'island universes' (Kant, 1755), supporting the idea that the spiral nebulae were large, distant objects outside of the Galaxy. These arguments were published in the Bulletin of the National Research Council in 1921 (Shapley & Curtis, 1921). The question was resolved later in the 1920s by Edwin Hubble's observation of Cepheid variables in the Andromeda Galaxy. Cepheids have a well constrained period-luminosity relationship (Leavitt 1908; Leavitt & Pickering 1912), so with his observations Hubble was able to show that the spiral nebulae were much too distant to be part of the Milky Way (Hubble, 1929). It is also worth noting that while observing the spiral nebulae, Hubble saw the same composite spectra as Fath and Slipher in NGC 1068, NGC 4051, and NGC 4151 (Hubble, 1926).

In parallel to advances in our understanding of galaxies was a similar advance on the topic of black holes. First proposed in 1783 by John Michell (Michell, 1784), the study of black holes really took off after Einstein proposed his theory of general relativity in 1915. The same year, despite being on the Russian front during World War I, Karl Schwarzschild found a solution to Einstein's field equations that describe a spherically symmetric, non-rotating, uncharged black hole. This solution was modified by Reissner (1916) and Nordström (1918) to include charge. Unsure what to do with the Schwarzschild radius, the point where the solution arrives at a singularity, black holes were mathematically stuck until the late 1950s. However, that did not stop people from contemplating the existence of a physical limit of some kind at the Schwarzschild radius, and the possibility that some celestial objects might encounter this physical limit in their lifetimes. Studies of stellar remnants in the 1930s established upper limits on the masses of white dwarfs (Chandrasekhar, 1931) and neutron stars (Oppenheimer & Volkoff, 1939). After reaching these maximum masses, the remnant will collapse due to the mass overpowering the degeneracy pressure of the electrons in white dwarfs or the degeneracy pressure of neutrons in neutron stars. It is now known that collapsing white dwarfs are the progenitors of type Ia supernovae. It is also now known that if a neutron star passes its mass limit, it collapses into a black hole. And while the current understanding of black holes hadn't been reached yet researchers still had an idea that, to quote Doctor Who, 'wibbily wobbly

timey wimey stuff' was happening if a neutron star collapsed. Oppenheimer & Snyder (1939) proposed that Schwarzschild's radius was the point where time stopped for an external observer, i. e. the collapsing system is viewed frozen from the moment it arrives at this point.

Back in the area of galaxy studies, the next big step towards arriving at our current understanding of AGNs was brought about in the 1930s. While working at Bell Telephone Laboratories, Karl Jansky was studying sources of noise affecting radio communications. After eliminating identifiable sources, he was left with 'hiss type atmospherics', which he had initially associated with the Sun, but then noted they were correlated with both the rotation and the revolution of the Earth (Jansky, 1933). In 1935, Jansky reported that the strongest signal of this interference seemed to be coming from the Galactic center (Jansky, 1935). Unfortunately, with the exception of the impressive work done by Grote Reber in his backyard through the late 1930s and 1940s, this idea would be put on the back burner for a while. Switching to optical wavelengths, the next clue came from Carl Seyfert. Seyfert (1943) published spectra of several galaxies. He noted that the emission lines observed had different line strengths and widths, but there seemed to be two distinct categories of how the lines looked. One group, which would come to be called Seyfert 2 galaxies, had similarly broadened permitted and forbidden lines (e.g., NGC 1068), while the other, Seyfert 1 galaxies, (e.g., NGC 4151, NGC 7469) had narrow forbidden lines as well as very broad wings on the Balmer lines. Following Seyfert's observations in the optical wavelengths, the next advance would come following the end of World War II in the radio bands. With leftover radar equipment (and their scientists) no longer being used for battle, the equipment was repurposed and led to a boom in radio astronomy post-war. Large radio surveys were conducted through the mid-1940s and 1950s, resulting in the discovery and further study of strong radio sources. One of the most significant surveys was the Third Cambridge Catalogue of Radio Sources (3C). After Minkowski (1960) identified a radio source at a redshift of 0.46, the search for additional optical counterparts to radio sources began, which led to the discovery of quasi-stellar radio sources, or quasars. Schmidt (1963) determined the redshift of 3C 273 at z=0.158, indicating it was a very distant object. Smith & Hoffleit (1963) observed 3C 273 being variable on short time scales, indicating that the object had to be small to

account for the timescales of these variations. They also observed a jet and proposed the mass of the object in 3C 273 had to be on the order of 10^9 Solar masses ($M_\odot$) to provide adequate energy for the 'lifetime' of the observed jet.[1]. These observations led Smith & Hoffleit (1963) to the conclusion that 'these numbers suggest interesting energy requirements for 3C 273'.

To welcome black hole studies to the '60s, Finkelstein (1958) mathematically solved the confusion about Schwarzschild's radius, describing it as a 'perfect unidirectional membrane: causal influences can cross it but only in one direction', which defines our current understanding of a black hole's event horizon. Once the radius was understood, work by Kerr (1963) and Newman et al. (1965) provided solutions for rotating black holes, uncharged and charged respectively. The Kerr-Newman metric gives us our current definition of a black hole with three fundamental properties - mass, spin, and charge - and at this point in time, the paths of galaxy research and black hole research began to merge. In 1964, both Edwin Salpeter and Yakov Zel'dovich proposed SMBHs as a potential power source for quasars. This was solidified by Lynden-Bell (1969), who theorized the thermal and particle emissions of an accreting SMBH were reasonable explanations for the 'incredible phenomena of high-energy astrophysics, including galactic nuclei, Seyfert galaxies, quasars and cosmic rays'. An in-depth overview of how AGN models involving black holes evolved in the literature is provided by Rees (1984).

The final piece of the AGN puzzle was found in the X−rays. In 1962, a Geiger counter was launched from White Sands in New Mexico and it discovered background X−rays, as well as a large X−ray peak near the Galactic center (Giacconi et al., 1962). Additional small experiments were conducted throughout the remainder of the 1960s. The first dedicated X−ray mission, *Uhura*, was launched in 1970 and reported X−rays from a few Seyfert galaxies, but it was data from *Ariel V* (Elvis et al., 1978) that established that strong X-ray emission was a general characteristic of Seyfert galaxies. A full overview of the history of AGNs observations, including gamma rays and the infrared, is provided by Shields (1999).

[1]The mass of 3C 273 aka PG 1226+093 is very close to a billion Solar masses!

Based on decades of work, we now know that AGNs are accreting black holes that live in galaxy nuclei, and AGN emission is visible across the electromagnetic (EM) spectrum, from radio waves to gamma rays. But a mystery still remained about why Seyfert 1s and Seyfert 2s showed different emission line characteristics. Osterbrock (1978) proposed that the two types of Seyferts are the same basic object but viewed from different perspectives. Work in the 1980s-1990s provided evidence confirming Osterbrock's proposition and led to the development of the Unified Model of AGNs, which represents much of our current understanding of AGN anatomy.

1.2 *AGN Components*

The first review of emerging Unified Models for AGNs was compiled by Antonucci (1993). The main constituents of an AGN, from center outward, are: the supermassive black hole, X−ray corona, accretion disk, broad line region, torus, and narrow line region. An overall schematic of an AGN, along with distance scale for perspective, can be seen in Figure 1.1.

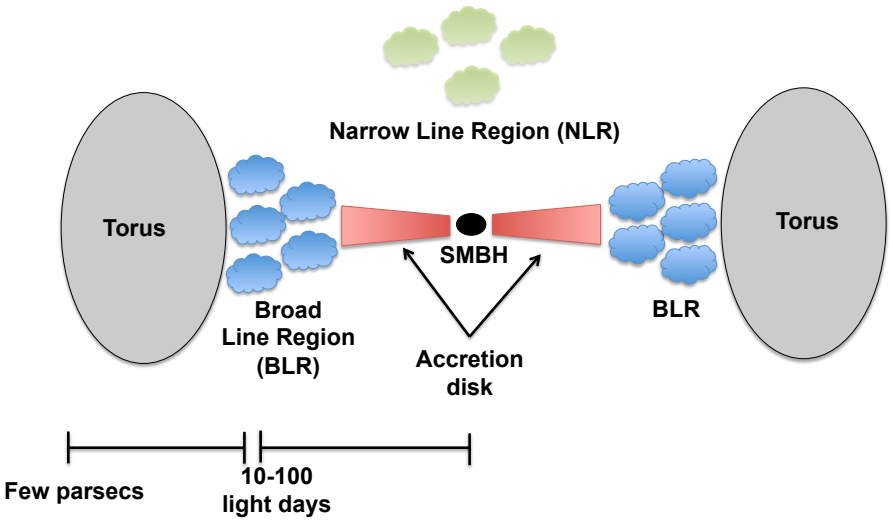

Figure 1.1: Schematic of AGN. Image credit: Claudio Ricci

Beginning with the central engine - which we define as the SMBH, X−ray corona, and accretion disk - AGNs are fueled by the accretion of materials onto the central SMBH. Supermassive black holes are generally defined as having mass greater than 10^6 $M_\odot$, although there is a growing list of AGNs that have been found to have SMBH masses on the order of 10^5 $M_\odot$, like NGC 4051, NGC 4395, UGC 06728[2]. The amount of energy emitted by the accretion process is defined (Peterson, 1997) as:

$$L = \eta \dot{M} c^2 \tag{1.1}$$

where L is luminosity, η is the accretion efficiency, $\dot{M}$ is the mass accretion rate, and c is the speed of light. The accretion efficiency is typically assumed to be $\sim$10%.

The exact nature of the accretion disk is not fully understood. The geometrically thin accretion disk from Shakura & Sunyaev (1973) is the most commonly applied model, but there are also models that propose slim or thick disks (e.g., Abramowicz et al. 1988). Reverberation mapping campaigns have helped confirm there is no 'one-size-fits-all' accretion disk model. Some campaigns have observed temperature profiles that do not match the Shakura and Sunyaev thin disk model (e.g., Fausnaugh et al. 2017). Additionally, the disk structure depends on the presence or absence of jets, the strength of magnetic fields, and the accretion rate (Peterson, 1997). Cackett et al. (2020) demonstrated the complicated nature of the accretion disk of the highly accreting AGN Mrk 142, which displays properties of both thin and slim disks. The accretion disk is also influenced by the X−ray corona (not shown in Figure 1.1). Padovani et al. (2017) describe this corona as an 'atmosphere above the accretion disk'. The corona is thought to be a region near the black hole where slightly relativistic electrons inverse Compton scatter UV photons from the accretion disk to X−ray energies (Haardt & Maraschi, 1991), but its geometry and the details regarding the effects that the corona and accretion disk have on each other (e.g., Proga 2005) remain a mystery.

On scales that are just beyond the corona and inner accretion disk (10s-100s light days) is the broad line region (BLR). The BLR is a region of gas that is photoionized by the energy coming

[2]Masses are from the AGN Black Hole Mass Database - `http://www.astro.gsu.edu/AGNmass/`

from the central engine. The Doppler-broadened emission lines, which are visible in the spectra of Seyferts 1s but not Seyfert 2s, arise from this region. These broad emission lines are useful tools for probing the central engine. First, the broadened lines combined with light travel time through the region can be used to obtain reverberation mapped mass measurements of the supermassive black hole hole (see Cackett et al. 2021 for a recent review). Second, profiles of the emission lines from the BLR can provide kinematic information and line ratios can provide other details (e.g., density, temperature) about the region (Peterson, 1997).

The boundary of the BLR is the torus. It is often depicted as a 'dusty donut', but the exact shape is not clear. The inner radius of the torus depends on the luminosity of the central source and can be as close as a few light months for low luminosity AGNs. The outer radius is a bit more complicated. Due to the 'clumpy' nature of the torus, it is difficult to model. Estimates for the outer radius range from a few parsecs to two-component torus models that have a diffuse region that extend hundreds of parsecs (Elitzur 2006; Hönig 2019). It is expected the torus is the mechanism that obscures the BLR in Seyfert 2s. Broad line emission from Seyfert 2s has been observed with spectropolarimetry (e.g., Antonucci & Miller 1985; Heisler et al. 1997; Du et al. 2017), with the dust of the torus providing a medium that scatters some BLR light into the observer's line of sight. As demonstrated in Figure 1.2, depending on the inclination of the AGN to the observer's line of sight, the torus may block the BLR from the observer. This region is dusty, being located outside of the dust sublimation radius of the central engine, therefore, while the torus may block our view of emission from the central engine and the broad line region, it emits thermal (infrared) radiation from warm dust (Kishimoto et al., 2007). The NIR wavelengths are emitted from the inner wall of the torus, near the dust sublimation radius, while longer infrared emission comes from more shielded dust further out in the torus.

The final AGN component is the narrow line region (NLR), which is the source of narrow emission from both permitted and forbidden transitions. The NLR extends from the inner $\sim$parsec of the AGN to 100s of parsecs beyond, and thus it is the only AGN component that may be spatially resolved. The NLR is an important region because it can shed light on AGN feeding and feedback,

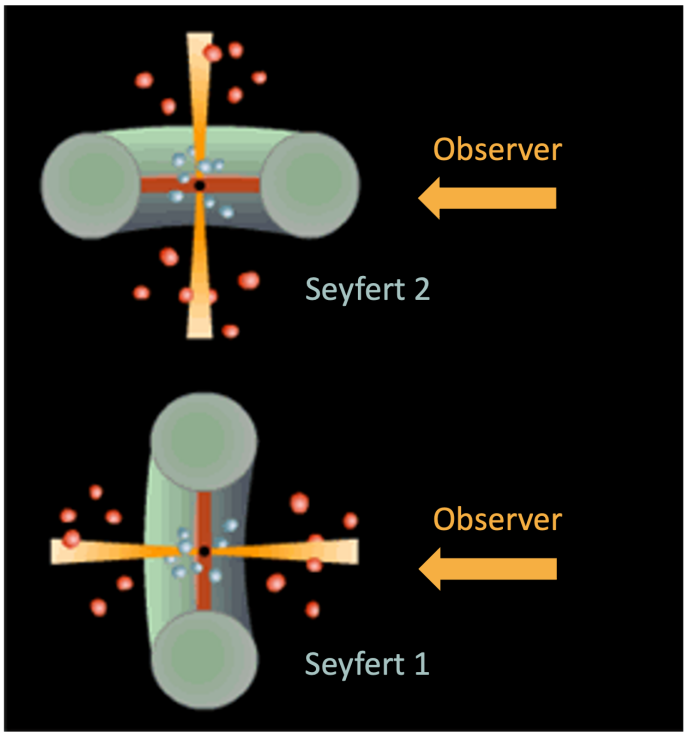

Figure 1.2: Seyfert galaxies are classified as Seyfert 1s or Seyfert 2s based on the inclination of the AGN and/or host galaxy to the observer, which determines if the torus (shown in green) obscures the BLR (shown as blue circles) from the observers line of sight. Image adapted from Brooks/Cole Thomson Learning

or how materials inflow to the AGN and how the energy radiated away from the AGN (outflows) can disrupt nearby gas reservoirs in the host (Peterson, 1997). The kinematics in the NLR can provide information about how the AGN luminosity and associated outflows may influence the host galaxy, for example by triggering or shutting down star formation (Meena et al. 2021; Revalski et al. 2021).

An additional part of AGNs anatomy that may sometimes be present is a jet. All AGNs emit in the radio wavelengths due to synchrotron radiation (Padovani et al., 2017) caused by relativistic electrons interacting with a magnetic field. The strength of that emission varies between radio-quiet and radio-loud sources. Radio-loud AGNs can produce collimated radio jets and lobes that extend throughout or even beyond the host galaxy (see Figure 1.3) which then contribute significantly to the bolometric luminosity of the system (Wilson & Colbert, 1995). The bolometric luminosity ($L_{\rm bol}$)

is the luminosity over the entire electromagnetic spectrum:

$$L_{bol} = 4\pi F d^2 \tag{1.2}$$

where F is the total flux and d is the distance to the object. The radio emission from radio-quiet sources is a minimal contributor to $L_{\rm bol}$. When a jet is pointed directly along an observer's line of sight, relativistic beaming magnifies the intrinsic luminosity and causes the source to appear brighter than it actually is.

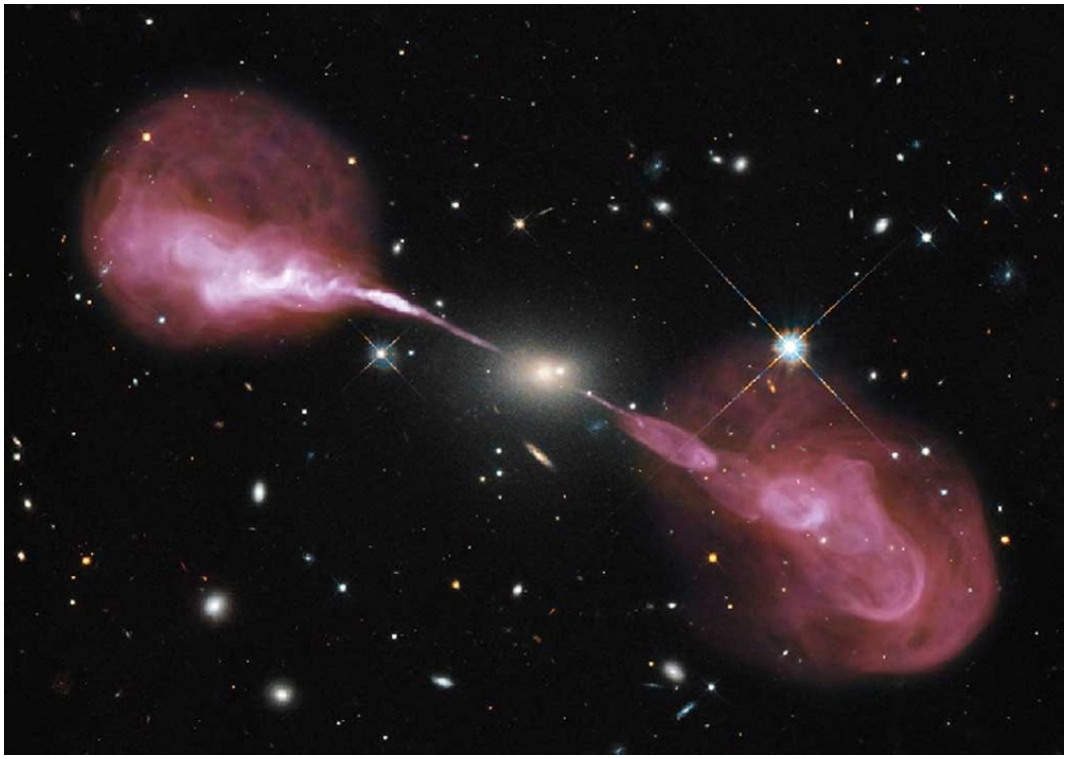

Figure 1.3: Combined radio and optical image of 3C 348. The galaxy is shown in optical wavelengths in the center of the image in yellow and the radio jets and lobes are shown in pink. Image credit:NASA/ESA/S. Baum and C. O'Dea (RIT)/R. Perley and W. Cotton (NRAO/AUI/NSF)/Hubble Heritage Team (STScI/AURA)

1.3 *AGN Spectral Energy Distributions*

As we have established, AGNs are comprised of many separate components that cover very different spatial scales. Furthermore, AGN emission is detected at all wavelengths across the electromagnetic spectrum. Spectral energy distributions, or SEDs, describe the amount of flux emitted at each wavelength and can be useful tools for studying AGN energetics. Each of the components of the AGN contributes to specific wavelengths in the SED. The torus, which is comprised of warm dust, dominates in the IR at wavelengths $\gtrsim 1.0$ μm, while the accretion disk, BLR, and NLR comprise the bulk of the optical-UV emission, and the corona dominates the X-ray wavelengths. Figure 1.4 demonstrates how these different regions of emission may together create the typical shape of an AGN SED.

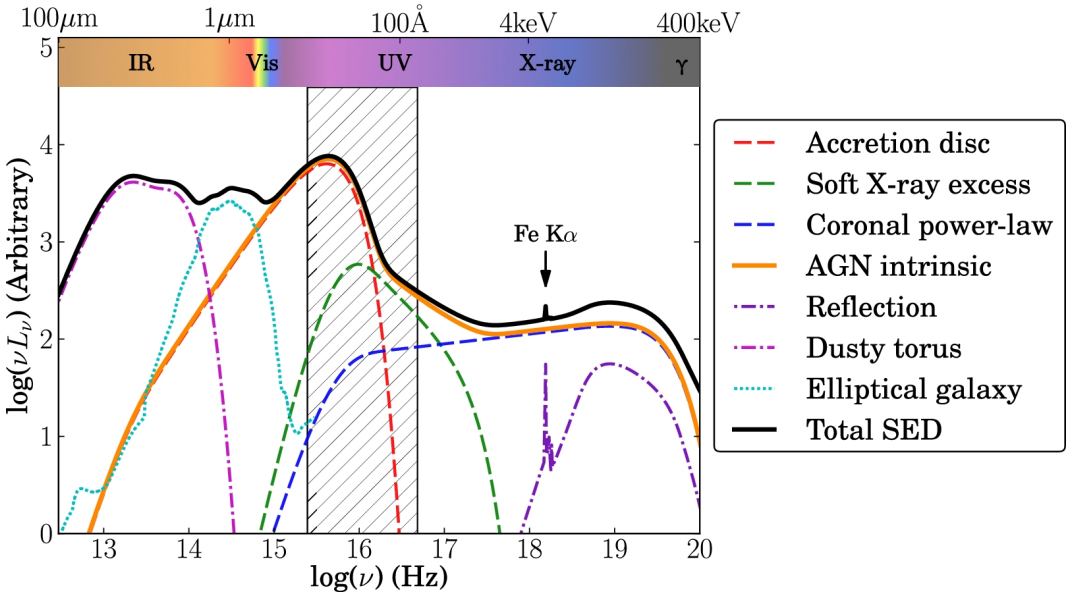

Figure 1.4: Schematic of an AGN spectral energy distribution from Collinson et al. (2017). The solid black line is the total SED shape. Dashed lines indicate intrinsic emission and dash-dot lines indicate reprocessed emission. The boxed, hatched area indicates the region where the intergalactic medium absorbs a significant fraction of energy and thus is generally not able to be directly observed. The dotted cyan line indicates stellar emission from an elliptical galaxy, which is external to the AGN system.

It is expected that the accretion disk flux peaks in the extreme UV (EUV), however we are unable to we are unable to directly observe this peak. EUV photons reside in an energy range

that makes them very susceptible to absorption by neutral gas in the intergalactic medium (IGM). At higher energies, there is a significant contribution from the soft X−ray excess (soft meaning energies less than 2 keV). It is not clear where this soft excess comes from, though it must be close to the corona and inner edge of the accretion disk, but it does seem to correlate positively with the accretion rate and is possibly caused by warm Comptonization (Gliozzi & Williams, 2020). There is also a transition just past 1 μm, where the dust sublimation boundary is expected to be and where the thermal emission from dust in the torus becomes the dominate flux source over the emission from the accretion disk (Sanders et al., 1989).

In addition to their shapes describing the relative contributions of various AGN components to the total energetics of the system, SEDs can provide additional information. By integrating under the SED, the total flux emitted by the system can be constrained and used to determine the bolometric luminosity. Once the bolometric luminosity is obtained, bolometric corrections can be calculated for various bandpasses, where a bolometric correction is defined as the ratio of the bolometric luminosity and the luminosity of a particular bandpass. This ratio may then be used to estimate the total luminosity over the electromagnetic spectrum from observations covering a limited range of wavelengths.

The other luminosity that needs to be considered is the Eddington luminosity. The Eddington luminosity is the maximum luminosity an object can have before the radiation pressure overpowers gravitational force:

$$L_{Edd} = \frac{4\pi G M m_p c}{\sigma_T} \tag{1.3}$$

and depends on the mass of the object, M, and the following constants: the gravitational constant (G), proton mass ($m_{\rm p}$), the speed of light (c), and the Thomson cross section ($\sigma_{\rm T}$). Taking the ratio of the bolometric and Eddington luminosities, the Eddington ratio ($\lambda_{\rm Edd}$) can be calculated. The Eddington ratio provides a comparison of the system's accretion rate relative to its maximum possible value (assuming spherical accretion).

There have been numerous studies focusing on the SEDs of quasars and AGNs. One of the first large studies was the Atlas of Quasar Energy Distributions (Elvis et al., 1994). Since then, there have been additional quasar SED studies (e.g., Richards et al. 2006; Elvis et al. 2012), SED studies specific to Seyferts (e.g., Alonso-Herrero et al. 2003; Brown et al. 2019), and SED studies that focus on AGNs with black hole mass measurements from reverberation mapping (e.g., Vasudevan & Fabian 2009; Kilerci Eser & Vestergaard 2018). The goal of any scientific endeavor should be to be both precise and accurate. However, if measurements are taken and known biases are not removed, it is possible to be precise while still being inaccurate. When constructing an AGN SEDs, there are several complicating factors that must be considered. The first is that AGNs reside in host galaxies and are observed through an aperture. In addition to the AGN, as shown in Figure 1.5, even with apertures that are on the order of 5-10″, there is a significant amount of host galaxy starlight that is also collected. The host galaxy can contribute anywhere from 20-70% of the total flux observed,

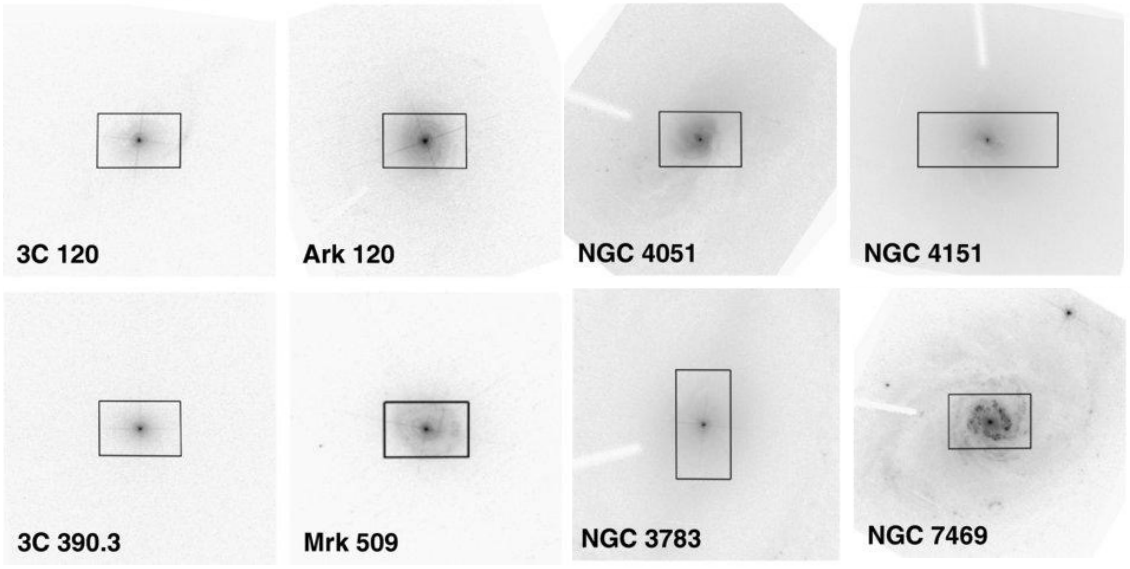

Figure 1.5: *Hubble Space Telescope* images (25″ × 25″) of a small collection of objects in our sample overlaid with ground-based spectroscopic monitoring apertures (shown in black) from Bentz et al. (2009).

even through relatively small apertures. Not removing the host galaxy contribution will bias any measurements or relationships based on the flux or luminosity (e.g., Bentz et al. 2006; Bentz et al.

2009). Therefore, in order to get an accurate understanding of an AGN, the emission from the host galaxy must be removed, however this step is overlooked in many studies.

After removing the host galaxy contribution, the second consideration is the AGN itself. A great deal of time and energy was put into creating maps and reddening curves to reduce the reddening caused by our Galaxy when looking outwards, so it should be expected that there is a similar issue when looking into other galaxies. Even if the host galaxy emission is removed, there is still internal reddening from the host and reddening intrinsic to the AGN structure itself (Gaskell & Benker 2007, Baron et al. 2016). Internal reddening will decrease the observed flux, especially at shorter wavelengths.

Also, while an important tool for understanding physical processes and fundamental properties of AGNs, studies that use AGN SEDs to understand the central engine must account for line emission from the BLR and NLR. While this line emission is intrinsic to the system, it is reprocessed emission, as is the IR emission from the torus.

Fourth, AGNs are variable objects, with variations happening on timescales of minutes to years and at all wavelengths (see Ulrich et al. 1997 for a review of AGN variability). AGNs are most variable in the X−ray wavelengths, with significant changes being observed in less than an hour (Gaskell & Klimek, 2003). At optical/UV wavelengths, variations typically occur on days to months timescales, with fairly large changes in amplitude (Gaskell & Klimek, 2003). The variations in these wavelengths appear to be correlated. They are seen first in the blue and then closely follow at redder wavelengths. However, whether the relationship seen in optical/UV is correlated with the X−rays is not entirely clear (e.g., Edelson et al. 2019). Despite being at much shorter wavelengths, X−ray variability has been observed to lead the optical/UV variations, lag behind the optical/UV, and show no correlation at all with the optical/UV, making the matter fairly complicated. In the NIR, variations occur on months timescales or longer (Lyu & Rieke, 2021), with amplitudes in variability being much smaller at these longer wavelengths (Sánchez et al., 2017). If SEDs are constructed without simultaneous observations, particularly in the optical/UV/X−ray wavelengths, the snapshots

observed at different wavelengths may be in unrelated high or low states, or anywhere in between, adding a source of error for any of the values obtained from that SED.

1.4 *Outline of Dissertation*

Our goal is to construct the most accurate multi-wavelength SEDs focusing on the accretion-driven flux from the central engine of a sample of AGNs. Our sample consists of AGNs with reverberation mapped black hole masses. We chose objects with RM masses for two reasons. First, the objects in the RM sample have well-constrained and direct mass measurements. As mentioned earlier in this chapter, mass is a fundamental property of a SMBH, so having well-constrained mass values helps to better constrain any measurement dependent on mass, like the Eddington luminosity. Second, due to these well-constrained mass measurements, the RM sample has been well studied and these objects have a wealth of supporting observations, like variability and distance studies (e.g., Edelson et al. 2019; Robinson et al. 2021). Combining these two factors, the RM sample remain popular objects for study, and so our results will be useful to a large number of people. To improve on previous studies, we will take steps to minimize the biases and uncertainties typically found in SED measurements, which include:

1. SEDs will be made from simultaneous optical/UV/X-ray data.
2. The simultaneous data will be supplemented by ground-based near-IR data to constrain the red tail of the SED.
3. Host galaxy starlight will be removed.
4. The reddening intrinsic to the AGN will be accounted for.
5. Emission from the BLR and NLR will be removed.
6. Distances that are not dependent on redshift will be adopted when available.

Many of the AGNs in our sample are nearby ($z < 0.1$) and their redshifts may be strongly affected by the gravitational force of neighbor galaxies and/or clusters, motivating the use of redshift

independent distance measurements whenever possible. Finally, given the highly variable nature of AGNs, we will examine 4 objects from our sample with 100+ simultaneous optical/UV/X-ray observations and quantify how variability impacts the shape of the SEDs and the scatter in measurements of bolometric luminosity and accretion rate.

With careful attention to these details, we will minimize the biases and uncertainties in the measurements that are typically derived from AGN SEDs. These measurements include bolometric luminosity, accretion rate, and bolometric corrections. We will also test existing relations that are frequently used by the community to estimate AGN properties when full SEDs cannot be constructed. Chapter 2 of this dissertation will cover the source selection, data reduction, removal of the host galaxy and other contributions, and SED construction. Chapter 3 will study the influence of variability on the SED shape and the quantities that are derived from the SED. Chapter 4 will discuss our results and their implications in the context of other published studies and Chapter 5 will summarize our findings and outline future work.

Chapter 2

XMM-NEWTON SOURCE SELECTION, DATA REDUCTION, AND SED CONSTRUCTION

2.1 *Source Selection and Data Reduction*

2.1.1 *Source Selection*

We began our sample selection with the simultaneous X−ray, UV, and optical observations from *XMM-Newton* (*XMM*) of 29 reverberation mapped AGNs collected by Vasudevan & Fabian (2009). The X−ray data was taken by the European Photon Imaging Camera (EPIC) instrument, which consists of 3 CCD cameras, two metal oxide semiconductor (MOS) arrays and one p-n junction (pn) array. EPIC covers *XMM*'s $30'$ square field of view (FOV) and is well calibrated in the $0.5-10$ keV energy range. The optical/UV data was taken by the Optical Monitor (OM) instrument. The OM is a modified Ritchey Chrétien telescope with a 30 cm diameter primary mirror. It has a $17'$ square FOV that sits in the center of the X−ray FOV and has six broadband filters that cover a wavelength range of $1700-5800$ Å, as well as a white filter, two grisms, and a field expander (Mason et al., 2001). The effective area plots of the two *XMM* instruments used can be seen in Figure 2.1.

While all of the objects in the sample of Vasudevan & Fabian (2009) included X−ray observations, they did not include a consistent number of optical and UV filters. We therefore required that a set of simultaneous observations must include at least two of the six broadband optical/UV filters available in order to constrain the optical/UV tail of the SED. With some sources, we were able to satisfy these criteria with a different set of XMM observations than was used by Vasudevan & Fabian (2009) while for other sources, no suitable data were available and so the AGN was dropped

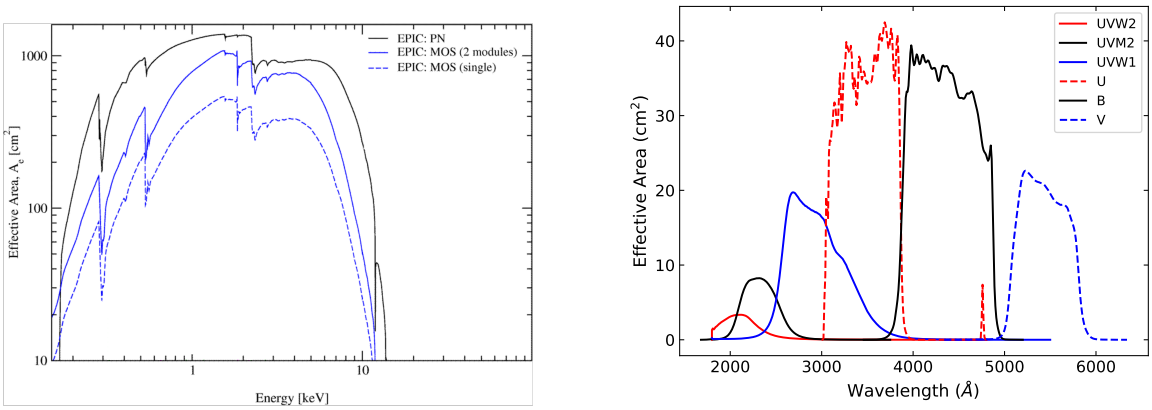

Figure 2.1: Effective area plots of *XMM-Newton*'s EPIC (left) and Optical Monitor (right) instruments. EPIC figure adapted from the *XMM-Newton* Users Handbook and the OM figure was creating using data from the SVO Filter Profile Service.

from our sample. This eliminated 11 objects from the original sample. We also searched the *XMM* archive for additional RM AGNs from the compilation of Bentz & Katz (2015) with observations that met our criteria but were not included in the study of Vasudevan & Fabian (2009), adding an additional 5 objects and giving us a final sample of 23 objects. Some sources had more than one *XMM* observation that fulfilled our criteria. These observations often had more filters than the observations used by Vasudevan & Fabian (2009) and provided us an opportunity to observe changes in the SEDs due to variability. The objects in our sample cover an approximate RA and Dec range of 0h to 23h and -38° to $+80^\circ$, with an approximate redshift range of $z = 0.002 - 0.158$. RA, Dec, and redshift values for each object, along with the *XMM* observation IDs, dates, and which OM filters were available for each observation, are listed in Table 2.1.

2.1.2 *Data and Supplemental Information*

XMM-Newton data All *XMM-Newton* data used in this study are archival and downloaded from the *XMM–Newton* Science Archive (XSA)[1]. Observation IDs and observation dates are listed in Table 2.1. For this analysis, like Vasudevan & Fabian (2009), we only utilize the X–ray data from the pn camera due to its superior sensitivity. As shown in the left panel of Figure 2.1, the

[1] `https://nxsa.esac.esa.int/nxsa-web/`

Table 2.1. Source List

Object	RA	Dec	Redshift	XMM ObsID	XMM ObsDate	OM Filters
Mrk335	00:06:19.5	+20:12:10	0.02579	0510010701	2007-07-10	B,U,W1,M2,W2
				0600540501	2009-06-13	V,B,U,W1,M2,W2
				0780500301	2018-07-11	V,B,U,W1,M2,W2
Mrk590	02:14:33.5	−00:46:00	0.02639	0109130301	2002-01-01	V,B,U,W1,M2,W2
				0201020201	2004-07-04	B,U,W1,M2,W2
3C120	04:33:11.1	+05:21:16	0.03301	0109131101	2002-09-06	V,U,W1,M2,W2
				0152840101	2003-08-26	V, UVW1
Ark120	05:16:11.4	−00:08:59	0.03271	0721600501	2014-03-24	V,B,U,W1,M2,W2
Mrk6	06:52:12.2	+74:25:37	0.01881	0305600501	2005-10-27	U,W1,M2,W2
Mrk79	07:42:32.8	+49:48:35	0.02219	0502091001	2008-04-26	B,W1,M2,W2
Mrk110	09:25:12.9	+52:17:11	0.03529	0201130501	2004-11-15	V,B,U,W1,M2,W2
				0840220801	2019-11-05	V,B,U,W1,M2,W2
NGC3227	10:23:30.6	+19:51:54	0.00386	0844341401	2019-12-05	V,B,U,W1,M2,W2
NGC 3783	11:39:01.7	−34:44:19	0.00973	0780860901	2016-12-11	V,B,U,W1,M2, W2
NGC4051	12:03:09.6	+44:31:53	0.00234	0157560101	2002-11-22	B,U,W1,M2,W2
NGC4151	12:10:32.6	+39:24:21	0.00332	0143500101	2003-05-25	V,B,U,W1,M2, W2
				0761670101	2015-11-12	V,B,U,W1,M2,W2
PG1226+023	12:29:06.7	+02:03:09	0.15834	0414190101	2015-07-13	V,B,U,W1,M2,W2
NGC4593	12:39:39.4	−05:20:39	0.00900	0109970101	2000-07-02	W1,W2
NGC4748	12:52:12.4	−13:24:53	0.01463	0723100401	2014-01-14	U,W1,M2
Mrk279	13:53:03.4	+69:18:30	0.03045	0302480401	2005-11-15	U,W1,M2,W2
NGC5548	14:17:59.5	+25:08:12	0.01718	0109960101	2000-12-24	U,W1,W2
Mrk817	14:36:22.1	+58:47:39	0.03146	0601781401	2009-12-13	W1,M2
3C390.3	18:42:09.0	+79:46:17	0.05610	0203720201	2004-10-08	U,W1,M2,W2
Zw229-015	19:05:25.9	+42:27:40	0.02788	0672530301	2011-06-05	W1,W2
NGC6814	19:42:40.6	−10:19:25	0.00521	0764620101	2016-04-08	V,B,U,W1
Mrk509	20:44:09.7	−10:43:25	0.03440	0306090401	2006-04-26	W1,M2,W2
				0601391101	2009-11-20	V,B,U,W1,M2,W2
PG2130+099	21:32:27.8	+10:08:19	0.06298	0150470701	2003-05-16	U,W1,M2,W2
NGC7469	23:03:15.6	+08:52:26	0.01632	0760350301	2015-11-24	V,B,U,W1,M2,W2

Note. — *XMM-Newton* OM ultraviolet filters - $UVW1$, $UVM2$, $UVW2$ - are abbreviated to W1, M2, and W2, respectively.

effective area of the pn camera is higher than the combined effective area of the MOS cameras. The observation dates of these data range from July 2000 to November 2019.

Near-infrared data The reddest observations available from *XMM* are in the *V* band, which peaks at ∼5500Å, leaving the red tail of the SED relatively unconstrained. To ensure a good fit, we supplemented the *XMM* observations with near-infrared (NIR) photometry. Around 1 μm, the emission from the accretion disk and the torus are expected to be roughly comparable (Padovani et al., 2017), and at longer wavelengths the emission from the torus dominates, so we set ∼1.6 μm (*H* band) as the reddest wavelength we will constrain in our study of the central engine. The near-infrared observations were collected in multiple observing programs using the WIYN High-Resolution Infrared Camera (WHIRC) on the 3.5-m WIYN telescope at Kitt Peak National Observatory (Bentz & Manne-Nicholas, 2018), as well as data taken from the VISTA Hemisphere Survey (VHS) (McMahon et al., 2013). WHIRC is a near-infrared imager that covers a wavelength range of 9000 Å to 2.5 μm. It has a FOV of $202'' \times 202''$ and a pixel scale of $0.0986''$. WHIRC has three broad band and 10 narrow band filters. We use the $H-$band filter, which has an effective wavelength of 1.65μm. The VHS data was taken with the Visible and Infrared Survey Telescope for Astronomy (VISTA), a 4-m telescope located at Paranal Observatory in Chile, with the VISTA Infrared Camera (VIRCAM). VISTA has a 1.65° ($5940''$) diameter FOV. VIRCAM has a mean pixel scale of $0.339''$ and five broad band and three narrow band filters that cover a wavelength range from approximately 8000 Å to 2.37 μm. We used $J-$band data, which has an effective wavelength of 1.25 μm. Table 2.2 lists the source of NIR data for each of our targets.

Ideally, the NIR data would be simultaneous with the optical/UV/X−ray data. However, as shown in Figure 2.2, AGN variability in the near-IR is at relatively low amplitude and occurs on timescales of several months to years (e.g., Sánchez et al. 2017; Elmer et al. 2020). We therefore include an additional uncertainty on the near-IR fluxes included here, to account for the (low−level) variability expected in the NIR between the dates of the NIR observations and the *XMM* observations.

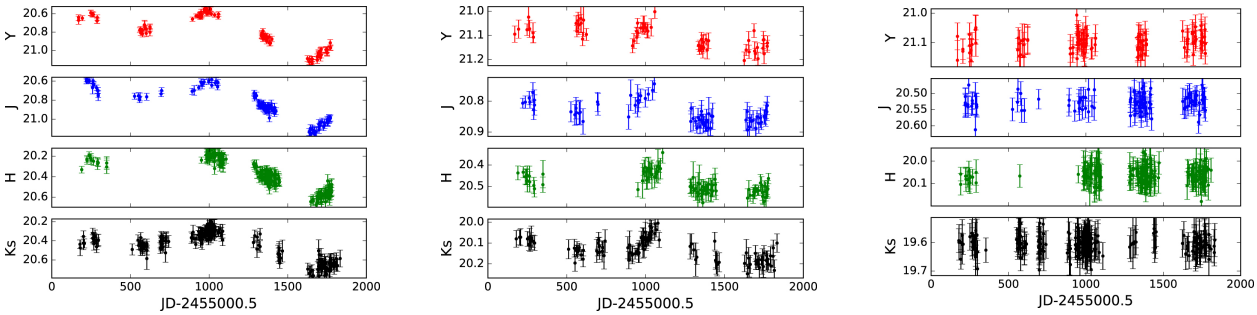

Figure 2.2: Examples of NIR light curves from Sánchez et al. (2017). The NIR data were taken by the UltraVISTA survey (McCracken et al., 2012) from December 2009 to June 2014. The objects, cid_543 (left - broad line, radio quiet AGN, z =1.298), cid_254 (middle - narrow line, radio quiet AGN, z =0711), and lid_2414 (right - radio loud AGN, z =0.916) are named by their identification number from the C-COSMOS Legacy sources multiwavelength catalog (Marchesi et al., 2019). From left to right, these examples show strong variability, weak variability, and no variability.

Host galaxy images & Galfit models All *HST* images and Galfit models used for host corrections were published by Bentz et al. (2006), Bentz et al. (2009), and Bentz et al. (2013). The AGN host galaxies were imaged with one of the optical cameras and a medium-V filter, either the Wide Field Camera 3 (WFC3) UVIS channel through the $F547M$ filter, the Advanced Camera for Surveys (ACS) with the High Resolution Channel (HRC) through the $F550M$ filter, or the Wide Field and Planetary Camera 2 (WFPC2) using the $F547M$ filter. The WFC3 UVIS channel has a 0.0395″ pixel scale and a 162″×162″ FOV. The ACS HRC had a 26″×29″ FOV and a 0.025″ pixel scale. The WFPC2 had a 0.0996″ pixel scale and 80″×80″ FOV. A summary of the HST image and corresponding reference for each target can be found in Table 2.2.

STIS spectra STIS spectra covering the UV-optical regime for NGC 4151, Mrk 110, Mrk 509, NGC3227, and NGC 6814 were used for emission line flux estimates and were downloaded as calibrated fits files from the Mikulski Archive for Space Telescopes (MAST)[2]. The observing program IDs and spectorgraph gratings used are listed in Table 2.2. The AGNs were observed through narrow apertures - 52″×0.1″ for NGC 4151, 52″×0.2″ for Mrk 110, Mrk 509, NGC 3227, and NGC 6814 - so they have minimal host galaxy contribution, making them 'clean' AGN spectra.

[2]`https://mast.stsci.edu/search/hst/ui/#/`

SMBH masses All SMBH masses were taken from the AGN Black Hole Mass Database (Bentz & Katz, 2015). Due to the generally unknown kinematics and geometry of the broad line region, a multiplicative scaling factor, f, is used to bring AGN and quiescent galaxy scaling relations into agreement. Mass values were calculated using $f = 4.82$ (Batiste et al., 2017).

Distances Given the nearby nature of our sample, we adopt redshift-independent distance measurements whenever possible. These include distances measured with the Tully-Fisher (TF) relation (Tully & Fisher, 1977), which is a correlation between the rotational velocity and luminosity of a galaxy. We utilized TF distances for 8 objects published by Robinson et al. (2021). We also utilized distances determined by the period-luminosity relationship of Cepheid variables (Leavitt, 1908) for NGC 6814 (Bentz et al., 2019), NGC 4151 (Yuan et al., 2020), and NGC 4051 (Yuan et al., 2021). The distance of NGC 7469 was constrained using the 'standard candle' nature of type Ia supernova (SNIa) (Ganeshalingam et al. 2013; Koshida et al. 2017). Finally, the distance for NGC 3227 was measured using surface brightness fluctuations of its companion, NGC 3226, with which it is interacting (Tonry et al., 2001). The surface brightness fluctuation method measures the clumpiness/smoothness of a galaxy based on resolved stars in the galaxy, with closer galaxies showing larger surface brightness fluctuations than distant galaxies. For the remaining objects, we adopted the luminosity distance with assumed cosmology $H_0 = 72$ km s^{-1} Mpc^{-1}, $\Omega_M = 0.30$, and $\Omega_\Lambda = 0.70$.

2.2 *Data Reduction and Measurements*

2.2.1 *XMM-Newton Data Reduction*

After downloading the original data files (ODFs) from the XSA, we reduced the *XMM–Newton* data using *XMM* Science Analysis Software (SAS) (v 16.1.0). For the X–ray data, the ODFs were processed using the `epproc` task. The `epproc` pipeline begins by processing the attitude file to create the housekeeping file, which contains information about the position and condition of the telescope and instruments. The main pipeline then processes the data in terms of the CCDs,

Table 2.2. Supplemental Information

Object	log(M_{BH}) ($M_\odot$)	Distance (Mpc)	Distance[a] Reference	HST data[b] & Galfit	HST Camera[b] & Filter	NIR data[b] & Galfit	HST STIS ObsProg ID	STIS Gratings
Mrk335	$7.280\pm^{0.042}_{0.044}$	109.5±7.1	1	7	ACS,HRC,F550M	9		
Mrk590	$7.619\pm^{0.062}_{0.074}$	112.1±7.1	1	7	ACS,HRC,F550M	9		
3C120	$7.794\pm^{0.038}_{0.040}$	140.9±7.1	1	7	ACS,HRC,F550M	9		
Ark120	$8.119\pm^{0.048}_{0.063}$	161.2±32.2	2	7	ACS,HRC,F550M	9		
Mrk6	$8.152\pm^{0.037}_{0.041}$	126.2±25.2	2	9	WFC3,UVIS2,F547M	9		
Mrk79	$7.661\pm^{0.107}_{0.136}$	50.2±10.0	2	7	ACS,HRC,F550M	9		
Mrk110	$7.34\pm^{0.101}_{0.097}$	150.9±7.1	1	7	ACS,HRC,F550M	9	15413	G230L, G430L, G730L
NGC3227	$6.684\pm^{0.081}_{0.102}$	23.7±2.6	8	7	ACS,HRC,F550M	9	8479	G140L, G230L, G430L, G730L
NGC3783	$7.420\pm^{0.077}_{0.76}$	49.8±10.0	2	7	ACS,HRC,F550M	10,11		
NGC4051	$5.940\pm^{0.084}_{0.145}$	16.6±0.3	3	7	ACS,HRC,F550M	9		
NGC4151	$7.605\pm^{0.051}_{0.047}$	15.8±0.4	4	7	ACS,HRC,F550M	9	7569	G140L, G230L, G430L, G730L
PG1226+023	$8.888\pm^{0.077}_{0.113}$	735.7±7.7	1	7	ACS,HRC,F550M	9		
NGC4593	$6.932\pm^{0.084}_{0.104}$	28.5±7.5	2	7	ACS,HRC,F550M	9		
NGC4748	$6.457\pm^{0.110}_{0.161}$	82.2±16.4	2	8	WFC3,UVIS2,F547M	9		
Mrk279	$7.484\pm^{0.099}_{0.133}$	129.7±7.1	1	7	ACS,HRC,F550M	9		
NGC5548	$7.692\pm^{0.016}_{0.016}$	83.6±16.7	2	7	ACS,HRC,F550M	...		
Mrk817	$7.636\pm^{0.064}_{0.072}$	130.8±6.9	2	7	ACS,HRC,F550M	9		
3C390.3	$8.897\pm^{0.084}_{0.058}$	243.5±7.2	1	7	ACS,HRC,F550M	9		
Zw229-015	$6.963\pm^{0.075}_{0.119}$	120.2±7.2	1	9	WFC3,UVIS2,F547M	9		
NGC6814	$7.088\pm^{0.056}_{0.058}$	21.6±0.4	5	8	WFC3,UVIS2,F547M	9	12992	G140L, G230L, G430L
Mrk509	$8.099\pm^{0.035}_{0.035}$	140±7.1	1	7	WFPC2,F547M	9	15124	G230L, G430L, G730L
PG2130+099	$7.482\pm^{0.055}_{0.063}$	274.7±7.3	1	7	ACS,HRC,F550M	9		
NGC7469	$7.006\pm^{0.048}_{0.050}$	61.9±3.3	6	7	ACS,HRC,F550M	9		

Note. — (a) Distances used as from the following sources - [1] Luminosity distance taken from AGN Black Hole Mass Database. [2] Tully-Fisher distance from Robinson et al. (2021). [3] Cepheid distance from Yuan et al. (2021). [4] Cepheid distance from Yuan et al. (2020). [5] Cepheid distance from Bentz et al. (2019). [6] SNIa distance averaged from Ganeshalingam et al. (2013) and Koshida et al. (2017). [8] Surface brightness fluctuation (SBF) distance from Tonry et al. (2001) (b) References for the *HST* $V-$band data, NIR data, and corresponding Galfit results are: [7] Bentz et al. (2009) [8] Bentz et al. (2013) [9] Bentz & Manne-Nicholas (2018) [10] McMahon et al. (2013) [11] This work. The NIR data for Bentz & Manne-Nicholas (2018) and NGC 5548 are WHIRC $H-$band imaging and NGC 3783 has VHS $J-$band imaging.

considering and correcting for bad pixels, energy scale, pattern recognition, gain, and charge transfer inefficiency. An event file is created at the end of the pipeline which can be used to extract the X−ray spectrum. The event file contains position and timing data of the observation, as well as instrument and calibration file information[3].

The X−ray spectra were extracted using the `evselect` task with 36″ radius circular source and background regions. For reference, a pn pixel has a size of 150×150 μm or 4.1″. We filtered patterns 0–4 to to select detector patterns that correspond to photon hits on the pixels rather than cosmic ray or other noise sources and flag==0 to avoid bad pixels and the edges of the CCD. The redistribution matrix file (RMF), which is a matrix used to go from energy space into detector position space, and ancillary response file (ARF), which contains the effective area and the quantum efficiency as a function of energy averaged over time, were made using the `rmfgen` and `arfgen` tasks. Additionally, using `specgroup`, we grouped the data to have a minimum of 25 counts per energy bin. Due to most astrophysical objects emitting few X−ray photons and the ability of X−rays to penetrate most materials, which makes them difficult to direct towards detectors, X−ray observations suffer from low count rates. This, combined with the relatively low spectral resolution of X−ray CCDs, leads to 'difficulties and uncertainties in any analysis' (Arnaud et al., 2011). So, in order to gain physical insight from these observations, X−ray data are fit using theoretical models folded through the instrument response (RMFs and ARFs). The X−ray spectra in this work were modeled in XSPEC (Arnaud, 1996) (v. 12.9.0) using `zwabs`, a redshift dependent photoelectric absorption model:

$$M(E) = exp[-\eta_H \sigma(E(1+z))] \tag{2.1}$$

where E is energy, η_H is column density, σ is the photoelectric cross section and z is redshift, and `powerlaw`:

$$A(E) = KE^{-\alpha} \tag{2.2}$$

[3]A full description of the event list structure can be seen here: `https://xmm-tools.cosmos.esa.int/external/xmm_user_support/documentation/dfhb/evpnima.html`

a simple photon power law, where E is energy, α is the photon index of the power law, and K is the normalization factor. These models were chosen as a simplest possible representation of the AGN continuum in the X−rays. After fitting the model to the data, flux values were calculated by multiplying the observed data by the ratio of the unfolded and folded models, where the unfolded model is the theoretical model integrated over the plot bin, while the folded model is the theoretical model multiplied by the RMF and ARF. The final calibrated flux values were output to ASCII files using the WData command.

The OM data were processed using the `omichain` pipeline. The pipeline identifies which filters were used in the observation, collects needed auxillary files, flat fields the image, detects sources and their positions, sets quality flags for each source, and calculates raw and corrected count rates. The count rates are corrected by flat fielding, for photon counting statistics, and differences in sensitivity across the detector. The pipeline then computes instrumental magnitudes, converts image coordinates to celestial coordinates, and produces a 'sky-image' for each observation. It then finalizes a combined source list and a and creates a mosaic of all the sky images from the individual cleaned exposures. Using the `omsource` task, we selected a region with a $6''$ radius centered on the nucleus of the AGN . The counts and errors were converted into fluxes using the flux conversion based on white dwarf flux standards[4], because white dwarfs show a strong blue+UV continuum, similar to what we expect for AGNs. We also tested the other conversion methods (e.g., AB flux, Vega flux) and they provided similar values. The flux conversion using this method is described as having an uncertainty less than 10%, but we adopted a conservative estimate of 10% uncertainties.

2.2.2 *Optical and UV Host Galaxy Removal*

To quantify the host-galaxy contamination in the optical and UV XMM data, we began with high-resolution images of each AGN host galaxy from the *Hubble Space Telescope* (*HST*). The data were originally collected with the goal of determining the starlight contribution of the host galaxy to measurements of the AGN luminosity. The images were modeled using Galfit (Peng et al. 2002;

[4] `https://www.cosmos.esa.int/web/xmm-newton/sas-watchout-uvflux`

Peng et al. 2010), a two-dimensional image decomposition program. Galfit is able to model galaxy components - bulge, bar, disk, rings - as well as the nucleus of the AGN. The model components were fit using a general Sérsic profile (Sersic, 1968):

$$\Sigma(r) = \Sigma_e \exp\left[-\kappa\left(\left(\frac{r}{r_e}\right)^{1/n} - 1\right)\right] \tag{2.3}$$

where Σ_e is the surface brightness of a pixel at the effective radius, r_e, and n is the Sérsic index, with κ being set by the value of n. The n value corresponds to the curvature of the component, with Gaussians having $n = 0.5$ and exponential disks having $n = 1$ (Peng et al., 2010). Bulges tend to have $n > 1$, while bars have $n < 1$. Additionally, Galfit allows rings to be modeled by including inner and outer truncation functions on any of its analytical functions, such as a Sérsic profile. The AGN is modeled with a point-spread-function (PSF). For the *HST* images, TinyTim (Krist, 1993) provides models of the PSF for each camera and filter combination while for ground-based images the PSF model is generally created by fitting a series of Gaussians to an isolated field star. The parameters of the Gaussians, which include position, magnitude, width, axis ratio, and position angle, are left free to arrive at a suitable fit. When an acceptable PSF model is found, it can be saved as an image for use in modeling the AGN. The sky component of the model was fit as a gradient across the image, allowed to vary in both the x and y directions. Once a successful model for a galaxy image has been created, the modeled AGN and sky components may be subtracted, creating an 'AGN-free' image of the galaxy. The *HST* data and Galfit models of these images were originally published by Bentz et al. (2006), Bentz et al. (2009), and Bentz et al. (2013).

From the AGN-free *HST* images, we determined the host galaxy starlight within the $6''$ radius aperture adopted for the OM measurements using the IRAF (National Optical Astronomy Observatories, 1999) task `phot`. The total counts measured with `phot` were then converted to a calibrated flux using the exposure time and the inverse sensitivity conversion factor (PHOTFLAM) to the galaxy flux through the *HST* filter. The filters used for the observations were medium-*V* filters, and small color corrections were calculated to account for the differences in bandpass between the

HST filters and a typical *V* filter. To estimate the host galaxy flux in each OM filter, we utilized the galaxy spectral templates of Kinney et al. (1996) and Calzetti et al. (1994). In Figure 2.3, we display the spectral templates for a pure bulge, an Sa galaxy, and a starburst. Note that the spectra are similar in the optical, and differ most strongly in the UV. We examined the *UVW2* 'postage stamp'

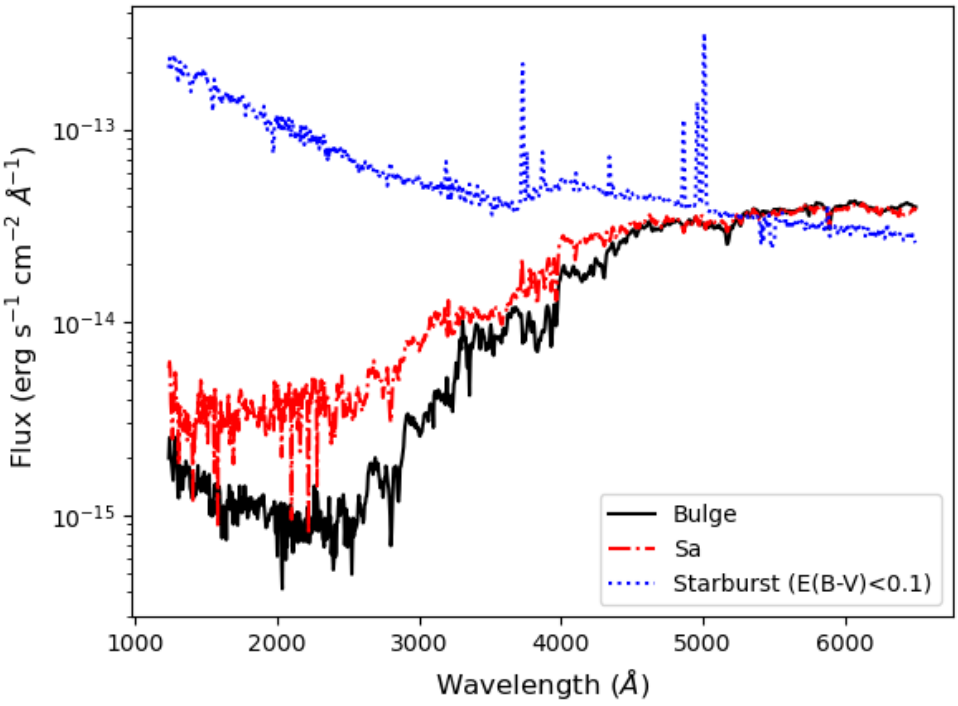

Figure 2.3: Comparison of galaxy templates. Bulge (shown in solid black) and Sa (shown in red dot-dash) templates are from Kinney et al. (1996) and starburst template for E(B-V) 0.1 (shown in dotted blue) is from Calzetti et al. (1994).

images on the *XMM–Newton* Science Archive to determine the contribution of spatially extended UV starlight near each galaxy center. An example of two postage stamp images can be seen in Figure 2.4. The majority of the sample showed very little extended emission in the UV images and we adopted a bulge template (Kinney et al., 1996) for the nuclear host galaxy flux. However, three objects - NGC 3227, NGC 4151, and NGC 7469 - exhibited bright and spatially extended UV flux in the nucleus. We initially attempted to treat them with a Starburst 1 template based on their E(B-V) values (Calzetti et al., 1994), however when scaled to match the host contribution in the

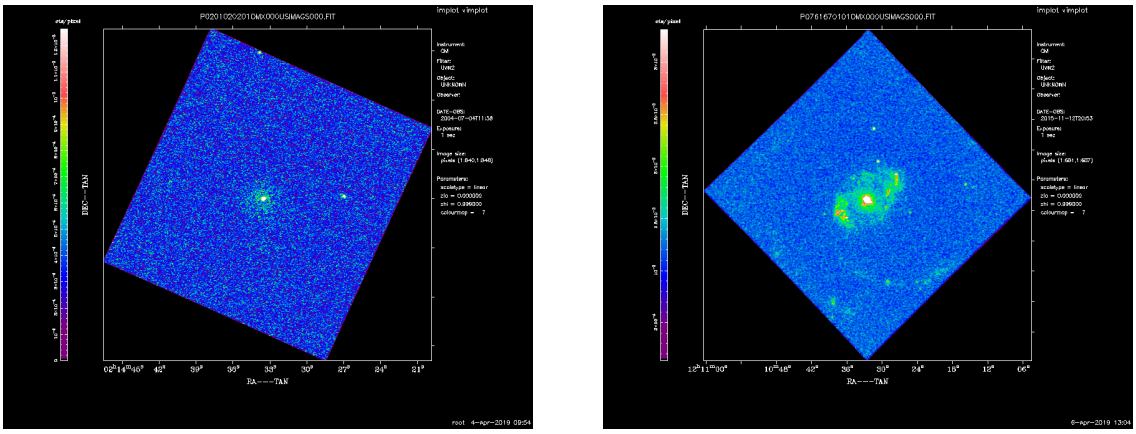

Figure 2.4: Comparison of the $UVW2$ ($\lambda_{\rm central}$ = 2013Å, effective width=435Å) images of Mrk 509 (left) and NGC 4151 (right) from the *XMM-Newton* Science Archive. The outer border of the Mrk 509 image is $\sim 27'' \times 27''$ while the outer border of the NGC 4151 image is $\sim 57'' \times 57''$.

V band, the starburst templates had too much host contribution in the $UVW2$ filter and provided a value that was greater than the total flux (AGN+stars) measured through the aperture. Instead, NGC 3227, NGC 4151, and NGC 7469 were treated with an Sa template (Kinney et al., 1996), which at $\sim$2100 Å ($UVW2$ central wavelength) has approximately a factor of 2 greater host flux than the bulge template.

After selecting the appropriate template, we used the `calcphot` task in IRAF to determine the template flux through the *HST* filter for each galaxy, adjusted for the galaxy redshift and Galactic extinction along our line of sight to each target. We then compared the template flux to the galaxy flux measured from the *HST* image and scaled the intensity of the template accordingly so that it would match the measured brightness for that specific galaxy. Finally, we use `calcphot` again, this time with the scaled galaxy template and the OM filter throughput[5] to estimate the galaxy flux in each of the OM bands. The estimated starlight contributions were then subtracted from the total flux in each band to derive an AGN-only flux. This correction varies in its impact. Some sources have host galaxies that are faint compared to the central AGN, so their starlight corrections are small, while other hosts can dominate the flux contribution in the visible bands. The host contribution in the $V-$band ranges from $\sim$20-70% of the total flux, so even sources on the low end of this

[5] `http://svo2.cab.inta-csic.es/theory/fps3/index.php?mode=browse&gname=XMM&asttype=`

range still have a significant portion of their optical flux coming from the host galaxy. Examples of how the removal of host contribution influences the optical/UV data can be seen in Figure 2.5, where we display Ark 120, which required a significant host galaxy correction ($\sim$69% in V) and Mrk 110 which has a minimal host correction of $\sim$21% in V. We also include NGC 4151, which was corrected with an Sa template rather than the bulge template and thus shows a larger correction in the UV than Ark 120 and Mrk 110.

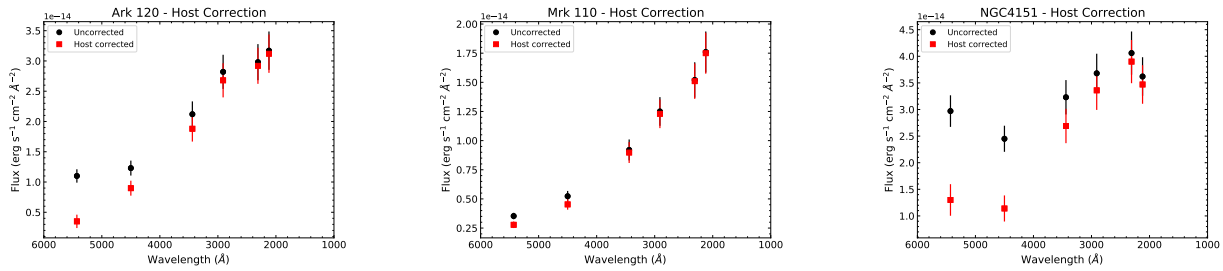

Figure 2.5: Comparison of the host corrections of Ark 120 (left), Mrk 110 (center), and NGC 4151 (right). The host contribution in Ark 120 makes up $\sim$69% of the total $V-$band flux, $\sim$21% in Mrk 110, and $\sim$56% in NGC 4151. Due to NGC 4151 having significant extended emission in the UV, its host correction was estimated using a Sa galaxy template, while the host corrections for Ark 120 and Mrk 110, which display little extended UV emission, were estimated using a bulge template.

Due to the well-known Malmquist bias, which is the preferential detection of intrinsically bright objects at larger distances, we expect that the most distant AGNs in our sample will be the most luminous and will also have the smallest host-galaxy corrections. We observe this trend in our sample, as seen in Figure 2.6. We also calculated the fractional contribution of the host to the total observed flux for the sources that had V band observations. We also see a decreasing trend of fractional host contribution as distance increases (also in Figure 2.6).

2.2.3 *NIR Tail*

Rather than adopting published values of the near-IR flux for each AGN in our sample, we again relied on Galfit to model and separate the AGN and host galaxy, but this time the goal was to isolate

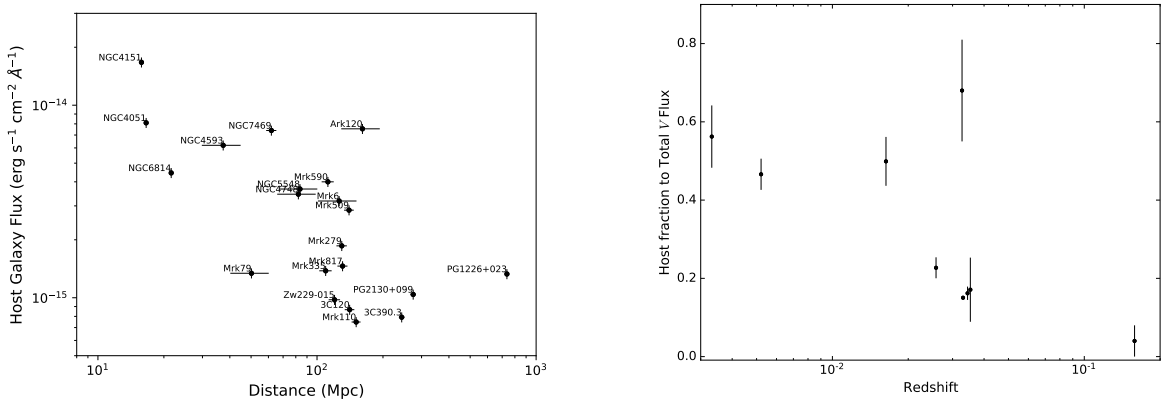

Figure 2.6: *Left*: Host-galaxy contribution to the $V-$band flux measured through our photometric aperture as a function of galaxy distance, for all galaxies in our sample. *Right*: Fractional contribution of the host galaxy flux to the total flux observed through our photometric aperture as a function of redshift. Only the sources with *XMM V* band data are shown.

and measure the AGN brightness rather than remove it. The majority of the NIR observations and Galfit models are described by Bentz & Manne-Nicholas (2018). The reduced near-infrared image of NGC 3783 was downloaded from the VISTA Hemisphere Survey (VHS) (McMahon et al., 2013). As part of this work, we present the Galfit model of NGC 3783.

With the NIR AGN magnitudes separated from their host galaxies, we were able to simply convert the magnitudes to fluxes using the Vega scale (Colina et al., 1996). When propagating the errors on the NIR flux, which determines the strength of its 'pull' on the red end of the SED fit, we considered two things. The first is that redward of ~ 1 μm the thermal emission from the torus starts to take over as the dominant flux source. So while we have minimized the host contribution, a portion of the unresolved nuclear flux is coming from the torus rather than AGN central engine. The second is variability. Although the NIR variability is smaller and occurs on longer timescales than at shorter wavelengths, the NIR observations are not simultaneous with the optical/UV/X−ray observations, and therefore require an additional uncertainty be added to the measurements. Based on the long term light curves of NIR monitoring campaigns (e.g., Sánchez et al. 2017; Elmer et al. 2020) and conservatively considering the central engine versus torus flux in this region, we apply a 0.3 magnitude error to all of the NIR nuclear magnitudes. Examples of the near-IR flux relative to the optical and UV fluxes are shown for three AGNs in Figure 2.7.

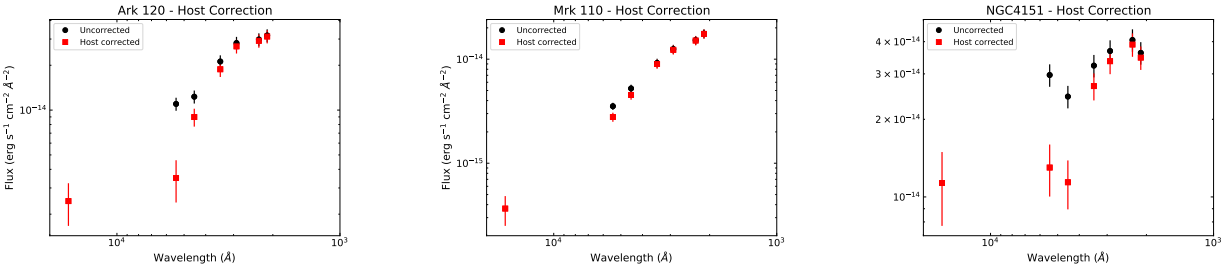

Figure 2.7: Same as Figure 2.5, but with the near-IR fluxes added for comparison with the optical and UV fluxes.

NGC 3783 Due to its location in the Southern Hemisphere, we were unable to obtain WHIRC images of NGC 3783. Instead, we utilized a high-resolution J band image from the VHS. The components used in the Galfit modeling were: a PSF for the AGN, a Sérsic bulge and bar, an exponential disk, and a ring. Model parameters are listed in Table 2.3 and the $J-$band image, model image, and residual are shown in Figure 2.8.

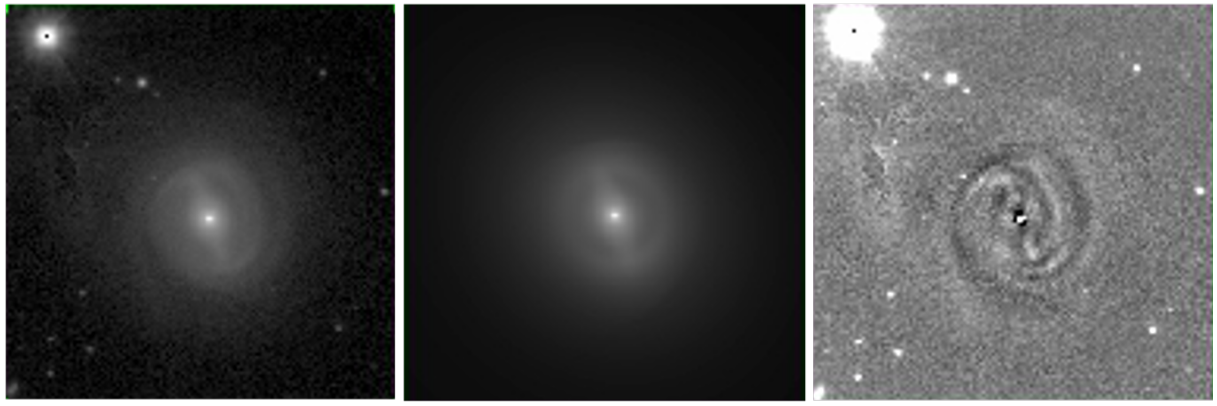

Figure 2.8: Two dimensional surface brightness decomposition of NGC 3783. The left hand figure is the VHS $J-$band images. The center figure is the Galfit model and the right-hand figure is the residuals after subtracting the model from the image. The image and model are displayed with a logarithmic stretch, and the residual is displayed with a linear stretch centered around zero counts. The bright star in the upper left hand corner was masked during the fitting process. The field of view of the image is $1.5' \times 1.5'$ and is oriented with north down and east to the right.

Table 2.3. Galfit parameters for NGC 3783

Object	m (mag)	r (arcsec)	n	q	PA (°E of N)	Component
NGC3783 (*J*)	12.53	···	···	···	···	PSF
	11.44	13.92	2.2	0.90	22.8	bulge
	13.07	26.47	0.2	0.32	19.2	bar
	10.10	46.82	1.0	0.89	47.2	disk
	15.19	23.50	1.0	0.72	15.9	ring
	···	54.00, 29.94	···	0.92	81.8	ring-inner
	···	92.50, 15.04	···	0.78	−55.2	ring-outer

Note. — The sky had counts of 3958.6 counts at the image center, with a gradient (ADUs/pix) of $-4.720E-03$ in x and $-5.284E-03$ in y.

2.2.4 *Line Emission Contribution*

Emission−line features are visible throughout the UV-optical spectra of AGNs. In the UV, the main species are C IV, C III], Al III, Mg II, and the 'little blue bump', which is a combination of Balmer recombination and Fe II (Wills et al., 1985), while Balmer and [O III] lines are dominant in the optical. Additionally, the redshift of the source influences which filters cover which line emission. As an example, the spectrum of NGC 4151 is compared to the OM filters in Figure 2.9 at (a) its true redshift of $z = 0.00332$, (b) $z = 0.05$, and (c) $z = 0.158$. At low redshift, the Mg II emission dominates in the $UVW1$ filter. However, at the high end of our redshift range, Mg II has mostly shifted out of the $UVW1$ filter and instead contributes to the U filter. Additionally, at low redshift, the line emission from [O III] and Hβ falls in between the B and V filters, but at higher redshift they contribute to the flux measured through the V filter.

The optical and UV line emission contributions were estimated from the HST STIS spectra. Out of our sample, only four objects had adequate STIS data to cover the same wavelength range as the OM filters - NGC 4151, NGC 3227, Mrk 110, and Mrk 509. A fifth AGN, NGC 6814, had a STIS spectrum covering the B band and blueward. The spectra are shown in Figure 2.10.

For each of the 5 AGNs with STIS spectra, we determined the flux contribution due to line emission by fitting a continuum to the spectrum. We estimated a local linear continuum based on the emission-free regions in each spectrum close to the filter bandpass of interest. After defining

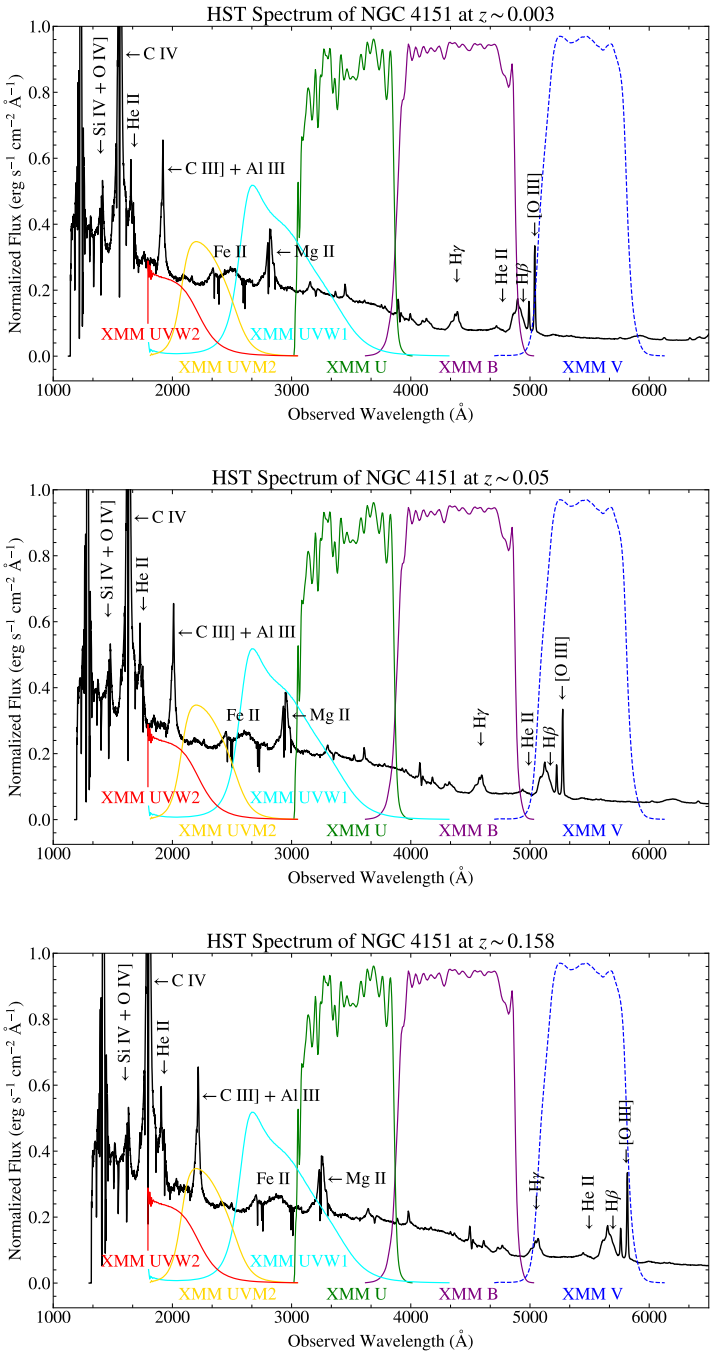

Figure 2.9: STIS spectrum of NGC 4151 at redshifts of $z = 0.00332$ (top), $z = 0.05$ (middle), and $z = 0.158$ (bottom). The transmission of the OM filters are plotted over the spectrum. Jupyter notebook from M. Revalski.

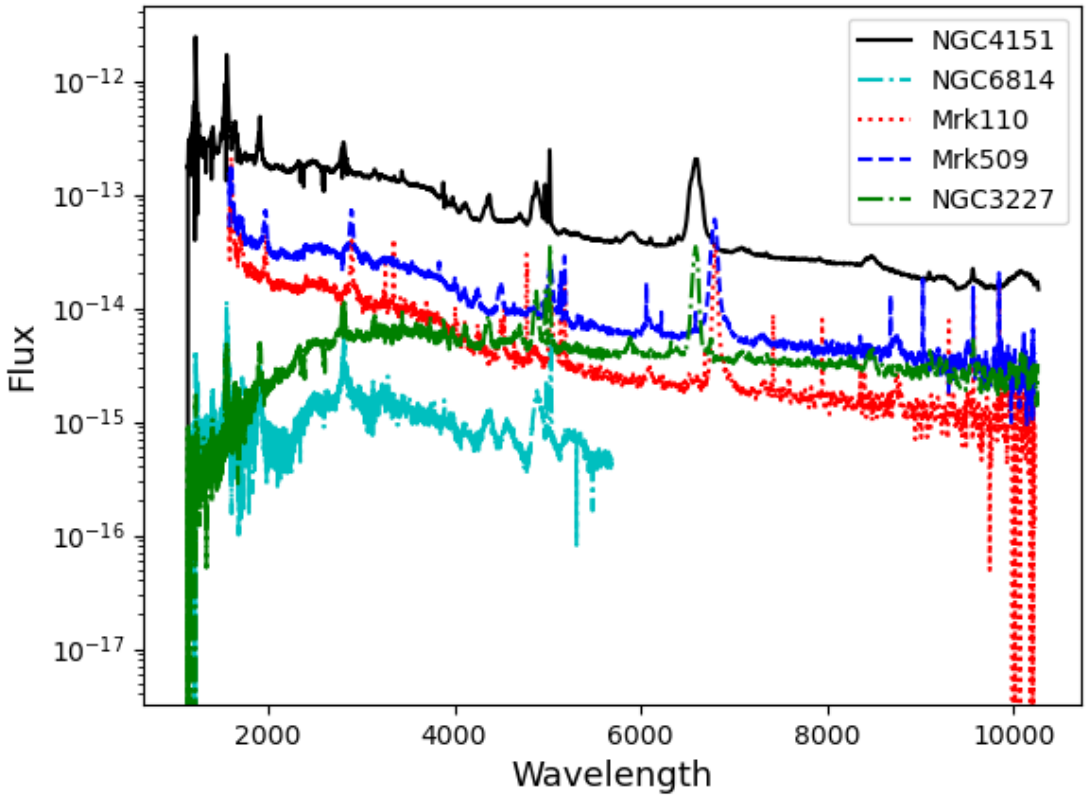

Figure 2.10: STIS spectra of NGC 4151 (solid black), NGC 6814 (dot-dash cyan), Mrk 110 (dot-dot red), Mrk 509 (dashed blue), and NGC 3227 (dot-dash green).

the continuum, we integrated both the flux under the continuum and the total flux through each OM filter. For the other AGNs in our sample, where no suitable STIS spectra exist, we shifted the spectra of NGC 4151, Mrk 110[6], and Mrk 509 to the redshift of each AGN. We then determined the fractional flux due to line emission through the OM filters, and adopted the weighted average of the values from the three spectra as an estimate of the possible line contamination. In Figure 2.11, we display the fractional line emission fluxes and weighted average at each redshift.

[6]Thanks, Ed!

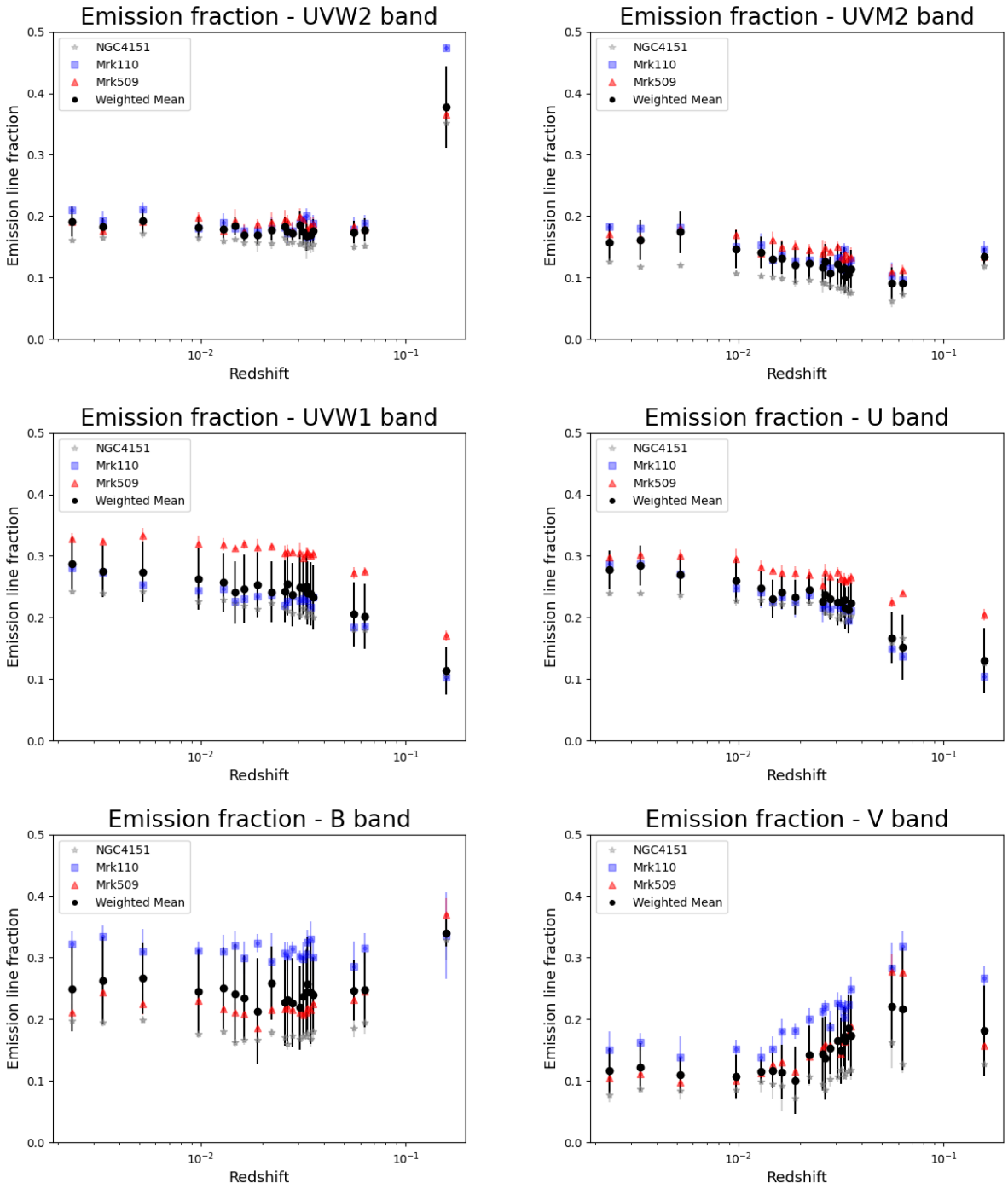

Figure 2.11: Comparison of emission fraction across sample redshift range in XMM Optical Monitor filters for NGC4151 (gray stars), Mrk110 (blue squares), Mrk509 (red triangles), and the weighted average of the three (black circles).

We do not make line emission corrections for most of the NIR data due to the wavelength range of the $H-$band filter being in a relatively line free region, as shown in a quasar template in Figure 2.12 (Glikman et al., 2006). The $J-$band filter used for NGC 3783 covers the region including the Paschen$-\gamma$ and $-\beta$ lines. This emission looks similar to the emission seen in the V band (a few strong lines, but otherwise mostly continuum), so to account for this, we estimated a 10% emission fraction for the J band flux measurement.

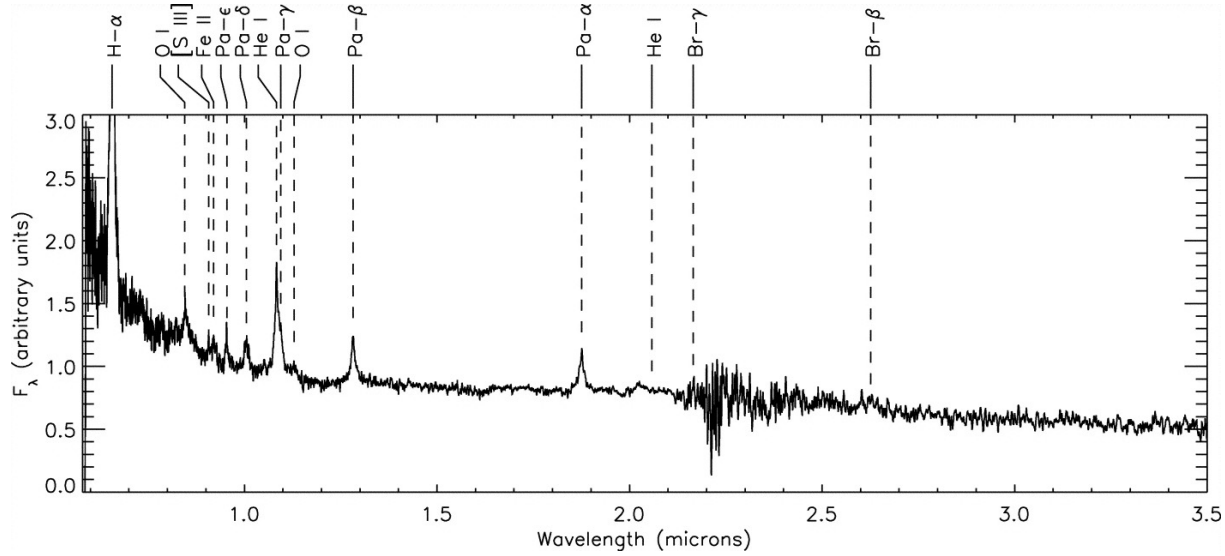

Figure 2.12: Composite NIR quasar template from Glikman et al. (2006). The effective wavelength of the WHIRC $H-$band filter is 1.65 μm with an effective width of 0.28 μm, covering a relatively emission-free region of the spectrum. The VISTA $J-$band filter, with an effective wavelength and width of 1.25 μm and 0.15 μm, includes Paschen$-\gamma$ and $-\beta$ features.

The spectra of NGC 6814 and NGC 3227 were used to correct their own line emission, but were not used in calculating the weighted average. It is difficult to deconvolve the line emission and the reddening from strongly reddened spectra, which NGC 6814 and NGC 3227 both are in the UV. The reddening in both sources is likely caused by an absorber. Crenshaw et al. (2001) propose that the reddened UV spectrum of NGC 3227 is caused by the presence of a 'luke-warm' absorber, which can be placed $>$100 pc from the nucleus. Looking at literature regarding NGC 6814, Turner et al. (1992) and Leighly et al. (1994) reported NGC 6814 having a warm absorber. However, analyzing observations collected with *NuSTAR*, Tortosa et al. (2018) report that the presence of

intrinsic absorbers in the *NuSTAR* bands is negligible. So it is possible that NGC 6814 also has an extended lukewarm absorber that is not visible in the X−rays, rather than a warm absorber.

2.2.5 *Reddening*

Unless you study it, dust is the bane of an astronomer's existence. We consider both Galactic extinction as well as reddening intrinsic to the AGN, correcting first for the known reddening along the line of sight due to dust in the Milky Way before tackling the unknown reddening intrinsic to each AGN.

2.2.5.1 Galactic Reddening

To correct for Galactic extinction we adopt A_λ values from the NASA/IPAC Extragalactic Database (NED) taken from Schlafly & Finkbeiner (2011). Schlafly & Finkbeiner (2011) used observations of stars from the Sloan Digital Sky Survey to recalibrate the Schlegel et al. (1998) dust map, providing updated reddening values for the whole sky. Unfortunately, there were not precomputed extinction values along each sightline for the Optical Monitor filters or the WHIRC H band filter, so we adopted available filters based on similar central wavelengths. In place of the OM $UVW2$, $UVM2$, $UVW1$, U, B, and V filters we used WFC3 $F218W$, WFC3 $F225W$, WFC3 $F300X$, and the Landolt U, B, and V filters. The UKIRT H band filter was used to correct extinction in the WHIRC H band. Using the A_λ values for each filter, we calculate the dereddened flux values, F_0, using:

$$F_0 = F_\lambda 10^{0.4A_\lambda} \tag{2.4}$$

In general, the corrections were modest as most of our AGN are outside the plane of the Galaxy, but with the magnitude of the correction increasing for shorter wavelengths.

2.2.5.2 Intrinsic AGN Reddening

To estimate the intrinsic reddening for each AGN, we follow a method similar to Baron et al. (2016). Baron et al. (2016) define $\alpha_{\rm opt}$ as the slope between 3000 and 5100Å, mathematically defined by their Equation 1. In their formulation, Baron et al. (2016) include an offset of −0.25 to correct for bound-free and line emission at 3000Å. As we have already corrected for these sources of emission, we slightly modify their definition of $\alpha_{\rm opt}$ by ignoring the offset of −0.25 and adopting the form:

$$\alpha_{\rm opt} = \frac{\log[L(3000\ {\rm A})/L(5100\ {\rm A})]}{\log(3000/5100)} \tag{2.5}$$

Due to $\alpha_{\rm opt}$ being determined by such a small wavelength range, we ran initial SED fits focusing solely on the optical and UV data (not including the NIR or X−ray data). The OM optical/UV data was fit by a power law of the form:

$$f(x) = bx^a \tag{2.6}$$

where x is wavelength, a corresponds to the slope of the fit, and b is a constant. A full description of the SED fitting process is discussed in Section 2.3, but in short, the power law was fit to each set of optical and UV points and included the uncertainties in the fluxes and the widths of the filter bandpasses. The $\alpha_{\rm opt}$ values were then calculated from the specific luminosity values determined from the initial SED fit for each AGN. The $\alpha_{\rm opt}$ values were then combined with α_0, or the intrinsic unreddened accretion disk slope, to estimate E(B-V):

$$E_{B-V} = 0.188(\alpha_0 - \alpha_{\rm opt}) \tag{2.7}$$

where the coefficient of 0.188 is derived from the Milky Way extinction law of Pei (1992). Baron et al. (2016) point out that the flux contribution from the host galaxy can alter the optical slope. In the previous section, we showed the majority of the host contribution is in the visible wavelengths - particularly the V band ($\sim$5000Å). As shown in Figure 2.5, removal of the host contribution will to some degree, depending on the AGN, steepen the optical slope, which will result in uncorrected and

host corrected sources having different $\alpha_{\rm opt}$ value. While Baron et al. (2016) note the importance of correcting for the host galaxy contribution, they do not themselves attempt to make any such corrections and so we cannot rely on their derivation of α_0, the expected intrinsic accretion disk slope. However, several of the AGNs in our sample are described in the literature as being 'bare' AGNs - Ark 120, Mrk 110, Mrk 335, Mrk 509, and NGC 7469 (Walton et al., 2013). These are AGNs that show little to no intrinsic absorption in the X−rays. These objects might reasonably be assumed to require little correction for intrinsic reddening in the optical and UV. In Figure 2.13, we display the $\alpha_{\rm opt}$ values derived for each of these AGNs from our initial SED fits.

In the literature we find that Ark 120 is consistently referred to as bright and bare, showing no signs of absorption along the line of sight (Crenshaw et al., 1999), no intrinsic absorbers around the central engine (Reeves et al., 2016), and no ionized absorption in the X−rays (Laha et al. 2014; Laha et al. 2016). Mrk 110 is also referred to as bright and bare, having its bareness compared to Ark 120 (e.g. Porquet et al. 2021; Reeves et al. 2021). However, the literature for the remaining bare sources all seem to report one thing in common. Mrk 509 has evidence for a warm absorber (Kaastra et al. 2012; García et al. 2019). Mrk 335 has evidence for a warm absorber (Liu et al., 2021)[7]. And NGC 7469 has a warm absorber (Kriss et al. 2000; Grafton-Waters et al. 2020). We note that the three sources with reported warm absorbers have systematically more negative $\alpha_{\rm opt}$ (flatter slopes) than the two sources without warm absorbers (see Figure 2.13). This may indicate that a warm absorber is related to reddening in the optical and UV, even if reddening in the X−rays is not detected. We thus only consider the two bare sources without warm absorbers, Ark120 and Mrk110, here when determining α_0. Taking the average of $\alpha_{\rm opt}$ of the two sources, we determined a new α_0 value of −0.5, which was used in place of the value of −0.1 that was adopted by Baron et al. (2016). With $\alpha_{\rm opt}$ values for all our sources and an adopted value of α_0, we calculated E(B-V) for each AGN. The E(B-V) values were combined with a Milky Way reddening curve to determine A_λ values. We also calculated E(B-V) values using the reddening curves of the Large Magellanic Cloud (LMC) and Small Magellanic Cloud (SMC) to determine the scatter on the E(B-V) values. The flux

[7]Tangentially, Mrk 335 which is well known for its variability (e.g. Tripathi et al. 2020), displayed a factor of four change in bolometric luminosity between the 2007 and 2018 observations in this work (see Table 2.5)

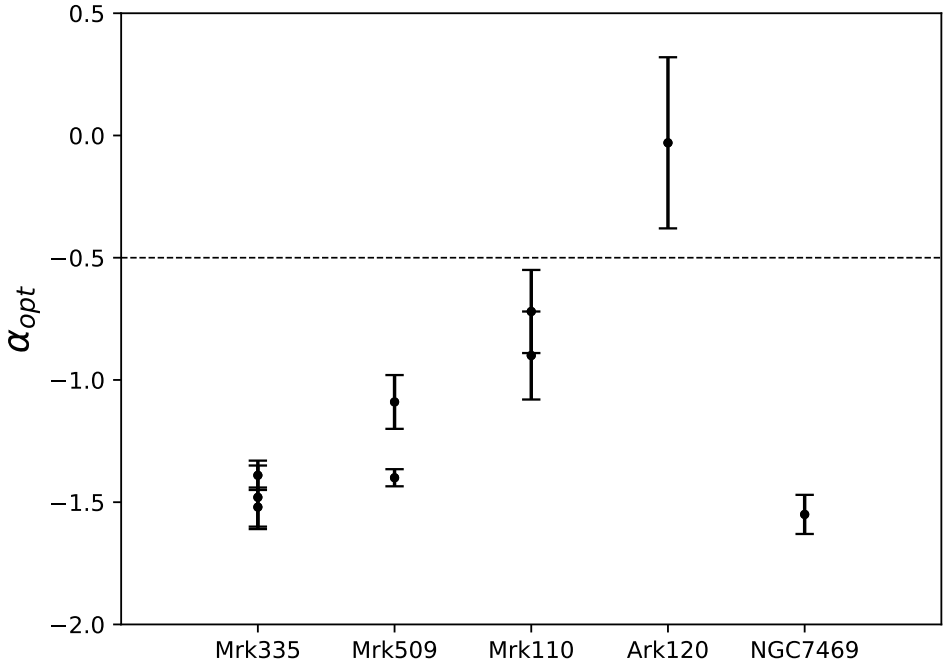

Figure 2.13: Comparison of $\alpha_{\rm opt}$ of Mrk 335, Mrk 509, Mrk 110, Ark 120, and NGC 7469. A less negative $\alpha_{\rm opt}$ indicates a steeper slope. The dashed black line shows our adopted α_0 value of -0.5 in relation to the $\alpha_{\rm opt}$ values of the 'bare' AGNs in our sample.

corrections were then calculated using Equation 2.4. The Galactic and AGN intrinsic E(B-V) values are listed in Table 2.4

In addition to the E(B-V) values, we also had axis ratios of the host galaxy disks, q_d, from the Galfit models from Bentz & Manne-Nicholas (2018). This allowed us to investigate whether there was any correlation between the calculated E(B-V) value and the inclination of the host galaxy. Using the q_d values, we determined the inclination angle, i, of the host (Holmberg, 1958):

$$\cos(i) = [(q_d^2 - q_{0,d}^2)/(1 - q_{0,d}^2)]^{1/2} \tag{2.8}$$

where $q_{0,d}^2 = 0.2$ and is the intrinsic axial ratio of a galaxy disk viewed edge-on (Tully & Pierce, 2000). As seen in Figure 2.14, there does not seem to be any correlation. Galaxies that are viewed

Table 2.4. Galactic and AGN Intrinsic E(B-V) Values

Object	XMM Obs Year	Galactic E(B-V)	AGN Intrinsic E(B-V)		
			Galactic	LMC	SMC
Mrk335	2007	0.031	0.185	0.191	0.206
	2009		0.169	0.175	0.188
	2018		0.192	0.198	0.213
Mrk590	2002	0.032	0.217	0.224	0.241
	2004		0.098	0.101	0.109
3C120	2002	0.226	0.151	0.156	0.168
	2003		0.107	0.110	0.119
Ark120	2014	0.109	0.000	0.000	0.000
Mrk6	2005	0.117	0.136	0.141	0.152
Mrk79	2008	0.061	0.176	0.182	0.196
Mrk110	2004	0.011	0.075	0.077	0.083
	2019		0.041	0.042	0.046
NGC3227[a]	2019	0.019	0.843	0.870	0.938
NGC3783	2016	0.104	0.031	0.032	0.034
NGC4051	2002	0.011	0.341	0.351	0.379
NGC4151	2003	0.023	0.234	0.242	0.260
	2015		0.223	0.230	0.248
PG1226+023	2015	0.018	0.133	0.138	0.148
NGC4593	2000	0.021	0.265	0.273	0.294
NGC4748	2014	0.044	0.131	0.135	0.146
Mrk279	2005	0.014	0.183	0.189	0.203
NGC5548	2000	0.017	0.222	0.229	0.246
Mrk817	2009	0.006	0.163	0.168	0.181
3C390.3	2004	0.061	0.301	0.311	0.335
Zw229-015	2011	0.062	0.185	0.191	0.206
NGC6814	2016	0.160	0.136	0.140	0.151
Mrk509	2006	0.049	0.171	0.176	0.190
	2009		0.111	0.115	0.124
PG2130+099	2003	0.038	0.189	0.195	0.210
NGC7469	2015	0.059	0.199	0.205	0.221

Note. — *XMM-Newton* Galactic E(B-V) values taken from the NASA/IPAC Extragalactic Database (Schlafly & Finkbeiner, 2011). AGN intrinsic E(B-V) values were calculated using Galactic, Large Magellanic Cloud (LMC), and Small Magellanic Cloud (SMC) extinction laws listed in Equation 9 of Baron et al. (2016).

nearly face on have a similar degree of nuclear reddening as galaxies that are much more highly inclined. Therefore, we expect that AGN reddening is mainly intrinsic to the AGN system itself, rather than arising on larger spatial scales within the host galaxy, for this sample.

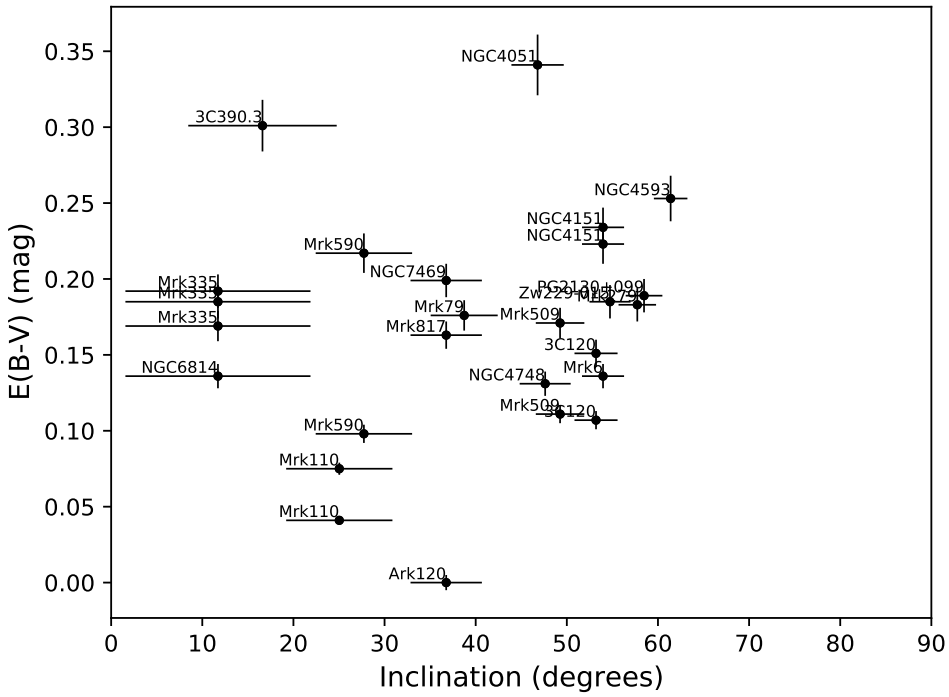

Figure 2.14: Host galaxy inclination versus intrinsic E(B-V). There is no apparent correlation between the host galaxy inclination and the intrinsic E(B-V) value indicating that the reddening is most likely intrinsic to the AGN system and not the larger scale host galaxy.

2.3 *SED Construction and Results*

Vasudevan & Fabian (2009) and others have traditionally fit the UV-optical portion of the SED as a blackbody curve. This is because the Shakura & Sunyaev (1973) treatment of the accretion disk as geometrically thin, but optically thick, allows for it to be treated locally as a blackbody. However, there are a few issues with using a blackbody to model the accretion disk (AD) emission. The first is that an AD is not, in fact, a blackbody. At first order, it is an amalgamation of blackbodies, with the peak temperature of the individual blackbodies depending on their position in the disk, as shown

in Figure 2.15. Depending on the density of the atmosphere above the accretion disk, electron

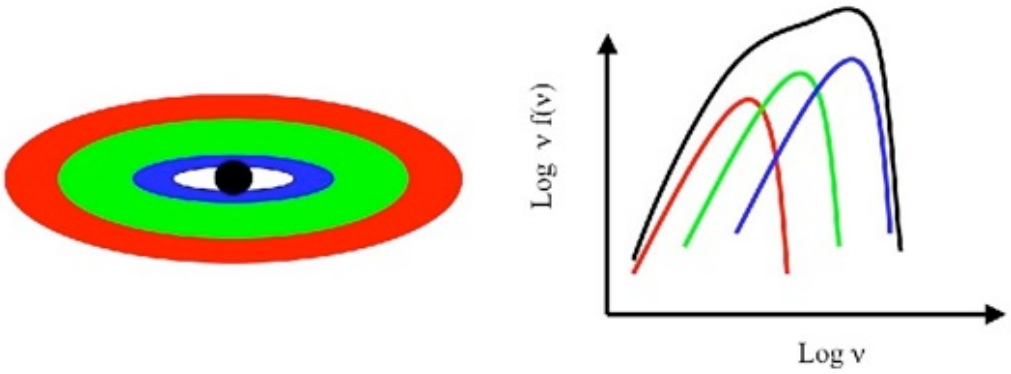

Figure 2.15: Schematic of an accretion disk temperature gradient and how nested blackbodies may create the optical-UV portion of an SED. Image credit: Jeanette Gladstone

scattering can cause non-blackbody emission. Understanding the opacities and scattering in AD atmospheres can help shed light on the size and environments of accretion disks (Czerny & Elvis 1987; Hall et al. 2018). Another issue is that we do not know at what wavelength the peak of the accretion disk emission is located. Quasar studies have shown a spectral break around 1100Å(e.g., Telfer et al. 2002; Shang et al. 2005), but due to uncertainties, it is not clear specifically where or how this peak varies from AGN to AGN. As discussed earlier, due to the absorption of EUV photons by neutral IGM, we cannot directly observe this region of the electromagnetic spectrum. Therefore, we do not model the optical-UV SED with a blackbody here. Instead, we fit the NIR - UV emission with a power law, choosing a conservative spectral break at 1200Å. Using a power law to fit this region has been done in several other studies for these same reasons (e.g. Vanden Berk et al. 2001). We also fit the X−rays with a power law, as is commonly done (e.g. Elvis et al. 1994, Vasudevan & Fabian 2009), but only from $2-10$ keV to avoid any excess in the soft X−rays and any influence from warm absorbers, both of which originate from reprocessed emission. The final component of the SED connects the UV at 1200Å to the X−rays at 2 keV, covering the unobservable EUV through the soft X−rays. It should be noted that the UV/X−ray connecting power law is defined by the fits to the NIR/optical/UV and to the X−rays and is not a separate fit itself.

The power law fits to the two observed wavelength regions - 16500Å to 1200Å and 2–10 keV - were carried out in log space using the orthogonal distance regression (`scipy.odr`) package in python. We chose to use ODR because it minimizes the sum of squared perpendicular distances, meaning it takes errors in both the x and y directions into consideration when calculating the fit. The `uncertainties` package was used to create a correlation matrix for propagating the errors on the fit. Prior to fitting the SEDs, the central wavelengths of the NIR/optical/UV filters were adjusted to account for the redshift of each AGN. An example of a final SED fit can be seen in Figure 2.16, where we show the measurements for NGC 4151 from 2015 as black data points with the power law fit to the UV through NIR as a solid red line and the power law fit to the X–rays as the dashed blue line. The dotted black line connects the two across the unobservable EUV. The complete set of SED plots for all AGNs in our sample can be found in Appendix A.

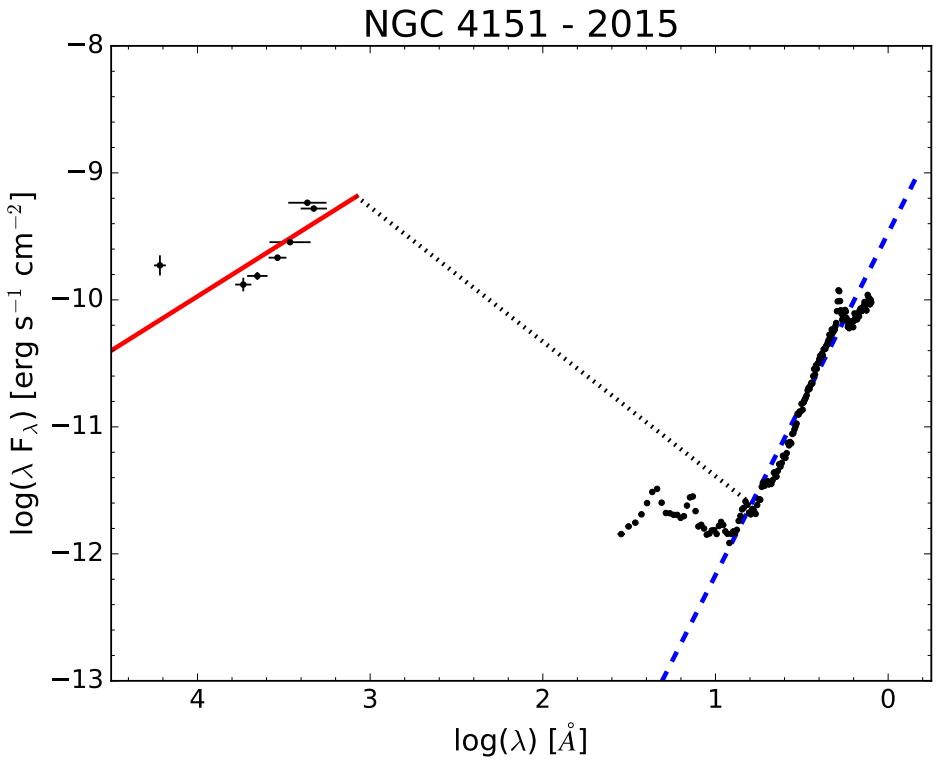

Figure 2.16: SED of the 2015 *XMM-Newton* observation of NGC 4151. The solid red line is the fit from 16500-1200Å, the blue dashed line is the 2–10 keV fit, and the black dotted line connects the two.

Once the fits were determined, we integrated over each fit region, from 1.65μm to 10 keV. The power law used to fit a and b in log-space corresponds to:

$$\lambda f(\lambda) = 10^b \lambda^a \qquad \Leftrightarrow$$
$$f(\lambda) = 10^b \lambda^{a-1}$$

To integrate f(λ) over λ:

$$\begin{aligned}\int_{\lambda_{\rm min}}^{\lambda_{\rm max}} f(\lambda)\mathrm{d}\lambda &= \int_{\lambda_{\rm min}}^{\lambda_{\rm max}} 10^b \lambda^{a-1}\mathrm{d}\lambda \\ &= 10^b \int_{\lambda_{\rm min}}^{\lambda_{\rm max}} \lambda^{a-1}\mathrm{d}\lambda \\ &= \frac{10^b}{a}\left[\lambda^a\right]\Big|_{\lambda_{\rm min}}^{\lambda_{\rm max}} \\ &= \frac{10^b}{a}\left(\lambda_{\rm max}^a - \lambda_{\rm min}^a\right)\end{aligned}$$

From the integrated flux, we calculate the bolometric luminosities and Eddington ratios. We also calculate the X−ray bolometric corrections ($\kappa_{2\text{-}10\,\rm keV}$):

$$\kappa_{2-10keV} = \frac{L_{bol}}{L_{2-10keV}} \tag{2.9}$$

where $L_{2-10keV}$ is the X−ray luminosity between 2−10 keV. And we calculate the commonly used $\alpha_{\rm ox}$, which is defined as:

$$\alpha_{\rm ox} = \frac{\log[L_\nu(2500)/\mathrm{L}_\nu(2\mathrm{keV})]}{log[\nu(2500)/\nu(2\mathrm{keV})]} \tag{2.10}$$

or the slope between 2500Å and 2 keV, where L_ν(2500Å) and L_ν(2 keV) are the specific luminosities at 2500Å and 2 keV in frequency space. We tabulate all of these values in Table 2.5.

Table 2.5. SED Values

Object	XMM ObsDate	log(L_{bol}) [erg s^{-1}]	log(L_{bol}) VF09 [erg s^{-1}]	log(9×L_{5100}) [erg s^{-1}]	L/L_{Edd}	L/L_{Edd} VF09	$\kappa_{2-10keV}$	α_{ox}
Mrk335	2007-07-10	44.99±0.04	45.0	45.06±0.04	0.408±0.033	0.515	170±14	-1.64±0.02
	2009-06-13	44.66±0.02	···	44.90±0.03	0.193±0.0011	···	567.6±3.3	-1.43±0.01
	2018-07-11	44.35±0.02	···	44.62±0.03	0.094±0.004	···	118±6	-1.59±0.01
Mrk590	2002-01-01	44.60±0.07	···	44.20±0.04	0.077±0.012	···	51±8	-1.34±0.03
	2004-07-04	44.36±0.05	43.8	44.03±0.05	0.044±0.006	0.0104	21.8±2.7	-1.19±0.02
3C120	2002-09-06	45.54±0.04	···	45.36±0.03	0.440±0.040	···	35.5±2.9	-1.31±0.02
	2003-08-26	45.25±0.05	45.3	45.15±0.04	0.227±0.028	0.305	16.1±2.0	-1.16±0.03
Ark120	2014-03-24	45.29±0.03	···	45.23±0.03	0.119±0.007	···	17.2±1.0	-1.17±0.01
Mrk6	2005-10-27	44.59±0.05	···	44.94±0.04	0.022±0.002	···	11.3±1.2	-1.05±0.02
Mrk79	2008-04-26	44.19±0.02	···	44.11±0.05	0.027±0.003	···	59±6	-1.43±0.02
Mrk110	2004-11-15	45.02±0.04	45.1	44.75±0.04	0.430±0.040	0.433	12.9±1.2	-1.09±0.02
	2019-11-05	44.85±0.03	···	44.59±0.04	0.288±0.022	···	9.7±0.8	-1.03±0.02
NGC3227	2019-12-05	43.15±0.03	···	43.47±0.04	0.023±0.002	···	23.9±1.6	-1.28±0.02
NGC3783	2016-12-11	44.42±0.01	···	44.74±0.01	0.157±0.003	···	32.2±0.6	-1.35±0.01
NGC4051	2002-11-22	43.71±0.05	42.6	43.63±0.04	0.48±0.05	0.0151	238±26	-1.67±0.02
NGC4151	2003-05-25	44.50±0.07	44	44.37±0.06	0.063±0.010	0.058	45±7	-1.38±0.03
	2015-11-22	43.61±0.03	···	43.71±0.03	0.008±0.001	···	19.8±1.1	-1.27±0.01
PG1226+023	2015-07-13	47.42±0.04	47.1	47.26±0.03	2.69±0.26	1.14	30.9±3.0	-1.29±0.02
NGC4593	2000-07-02	43.95±0.05	43.7	43.78±0.08	0.082±0.009	0.0369	23.1±2.6	-1.22±0.03
NGC4748	2014-01-14	44.43±0.04	···	44.35±0.04	0.750±0.080	···	38±4	-1.32±0.02
Mrk279	2005-11-15	45.26±0.04	45	45.12±0.05	0.540±0.050	0.216	32.7±3.0	-1.29±0.02
NGC5548	2000-12-24	45.18±0.23	44.3	44.49±0.26	0.220±0.120	0.0236	55±29	-1.30±0.04
Mrk817	2009-12-13	45.37±0.07	···	45.29±0.07	0.440±0.070	···	88±15	-1.48±0.04
3C390.3	2004-10-08	45.85±0.05	45.2	45.61±0.05	0.117±0.012	0.0466	26.2±2.7	-1.24±0.02
Zw229-015	2011-06-05	44.28±0.06	···	44.10±0.07	0.165±0.021	···	25.8±3.3	-1.25±0.03
NGC6814	2016-04-08	43.50±0.05	···	43.37±0.04	0.021±0.002	···	22.3±2.6	-1.23±0.05
Mrk509	2006-04-26	45.71±0.04	45.2	45.69±0.05	0.325±0.029	0.0951	46±4	-1.37±0.02
	2009-11-20	45.63±0.03	···	45.55±0.03	0.272±0.020	···	31.5±2.4	-1.30±0.02
PG2130+099	2003-05-16	45.72±0.04	45.0	45.70±0.04	1.37±0.12	0.0179	149±13	-1.59±0.02
NGC7469	2015-11-24	44.75±0.04	···	44.60±0.04	0.44±0.04	···	40±4	-1.33±0.02

2.3.1 *Comments on Individual AGN*

Vasudevan & Fabian (2009) took their mass values from Peterson et al. (2004), with the exception of NGC 4593 which was taken from Denney et al. (2006). They used luminosity distances with an assumed cosmology of H_0 = 71 km s^{-1} Mpc^{-1} and Ω_M = 0.27.

NGC 3227 Due to the extremely reddened nature of NGC 3227, the $\alpha_{\rm opt}$ value calculated was -4.99, which corresponds to an E(B-V)=0.843. This resulted in a factor of $\sim$1500 reddening correction in the $UVW2$ filter and provided an Eddington ratio of 2.1. Using Equation 4 in Baron et al. (2016), we calculated the extinction law for NGC 3227 using the reddening curve determined by Crenshaw et al. (2001). This resulted in an E(B-V) value of 0.78, which again resulted in a super-Eddington accretion rate. A large E(B-V) value has also been reported in other works. For example, Jaffarian & Gaskell (2020) cite an E(B-V) value of 0.98 using the ratio of Hα to Hβ. However, all of these large E(B-V) values result in super-Eddington accretion rates when adopting the Galaxy, LMC, SMC, or NGC 3227 reddening curves. NGC 3227 is not known to be a super-Eddington source. This will require further investigation, but for this work, we adopt the E(B-V) value of 0.18 from Crenshaw et al. (2001) and calculate the A_λ values using the NGC 3227 reddening curve from the same work.

NGC 4051 The Cepheid distance to NGC 4051 was determined by Yuan et al. (2021). Due to its previously underestimated distance, NGC 4051 was thought to have a very low Eddington ratio compared to other narrow-line Seyfert 1 (NLS1) galaxies (e.g., Collin et al. 2006). NLS1s typically have an Eddington ratios greater than 0.1. The updated distance measurement brings the Eddington ratio of NGC 4051 into the range expected for NLS1s.

NGC 5548 $H-$band imaging has been collected, and after reduction and modeling with Galfit, it will be folded into our analysis to constrain the red tail of the SED. Currently, NGC 5548 is fit with 3 OM points.

PG1226+023 PG1226+023 is a well-known blazar and sees increased luminosity values due to relativistic beaming. In this analysis, we do not attempt to correct for relativistic beaming, though we note that such a correction may be important for this AGN.

PG2130+099 The mass value of PG2130+099 that was used by Vasudevan & Fabian (2009) - $\log(M) = 8.66$ $M_\odot$ - was from Peterson et al. (2004). This mass value was updated by Grier et al. (2012) to $\log(M) = 7.433$ $M_\odot$. Grier et al. (2012) attribute the discrepancy in mass measurements to undersampled light curves in the initial measurement and long-term secular changes in the Hβ equivalent width. We also note that we our analysis suggests PG2130+099 may be mildly super-Eddington. This will require additional consideration.

2.3.2 α_{ox}

Several studies have found that α_{ox} decreases with increasing AGN luminosity (e.g. Strateva et al. 2005; Steffen et al. 2006). We tested if the anti-correlated relation between L_{2500} and α_{ox} still holds when the host, line emission, and intrinsic reddening have been corrected for in the flux measurements. In Figure 2.17, we plot our α_{ox} values and specific luminosities at 2500Å against the best fit for the α_{ox}–L_{2500} relationship based on 333 AGNs from the Sloan Digital Sky Survey (SDSS), COMBO-17 survey, and the Bright Quasar Survey published by Steffen et al. (2006):

$$\alpha_{ox} = (-0.137 \pm 0.008)\log(L_{2500}) + (2.638 \pm 0.240) \tag{2.11}$$

As seen in Figure 2.17, our α_{ox} values fit within the uncertainty of the relationship.

2.3.3 *Bolometric Corrections*

We calculated both optical and X–ray bolometric corrections for our sample. We first tested the commonly used optical bolometric correction of 9 times the specific luminosity at 5100 Å, established by Kaspi et al. (2000). In Figure 2.18, we show the 1-to-1 relationship as well as the ODR fit to the values and their errors. Based on the ODR fit, instead of 9 times the optical

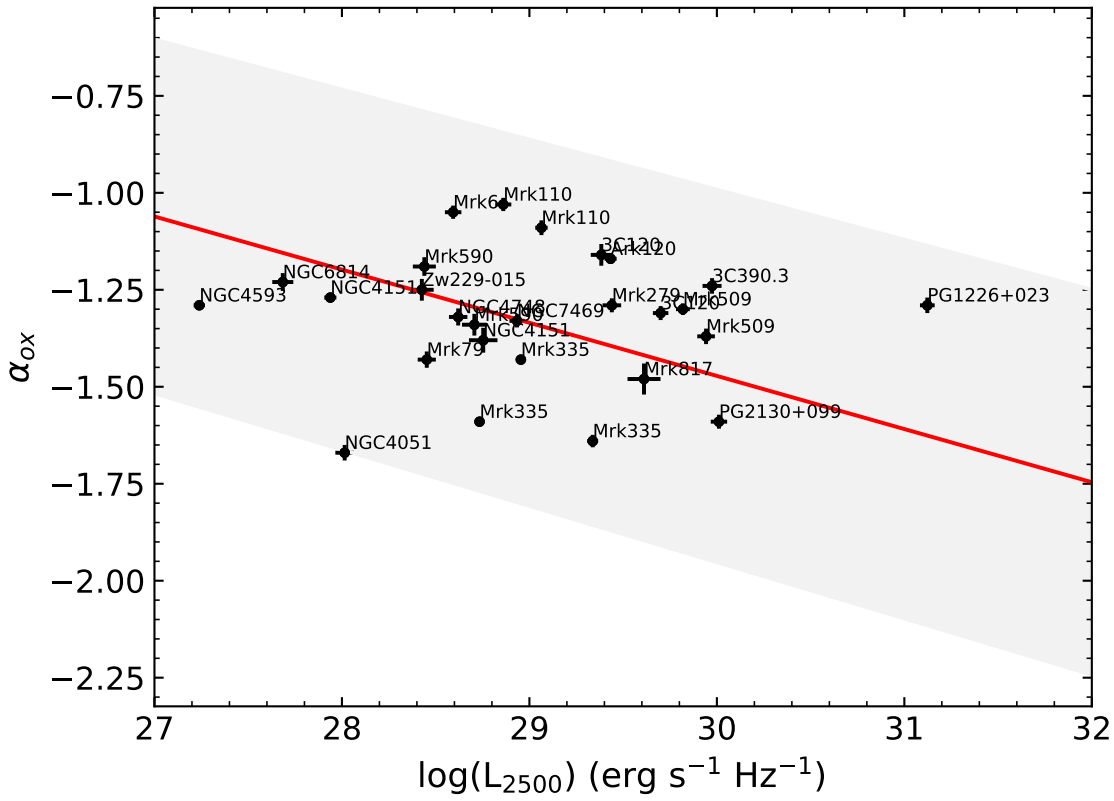

Figure 2.17: Specific luminosity at 2500Å versus α_{ox}. For comparison, the best fit for the α_{ox}–L$_{2500}$ relationship determined from 333 AGNs by Steffen et al. (2006) is show by the solid red line and the error is shaded in gray.

specific flux, this fit indicates a factor of 8.23±0.52 as the optical correction. We also calculated the bolometric correction for the X–rays from 2 – 10 keV. We plotted the X–ray correction against the X–ray luminosity, the Eddington ratio, and the bolometric luminosity. As can be seen in Figure 2.19, there are no apparent correlations between these values for the objects in our sample.

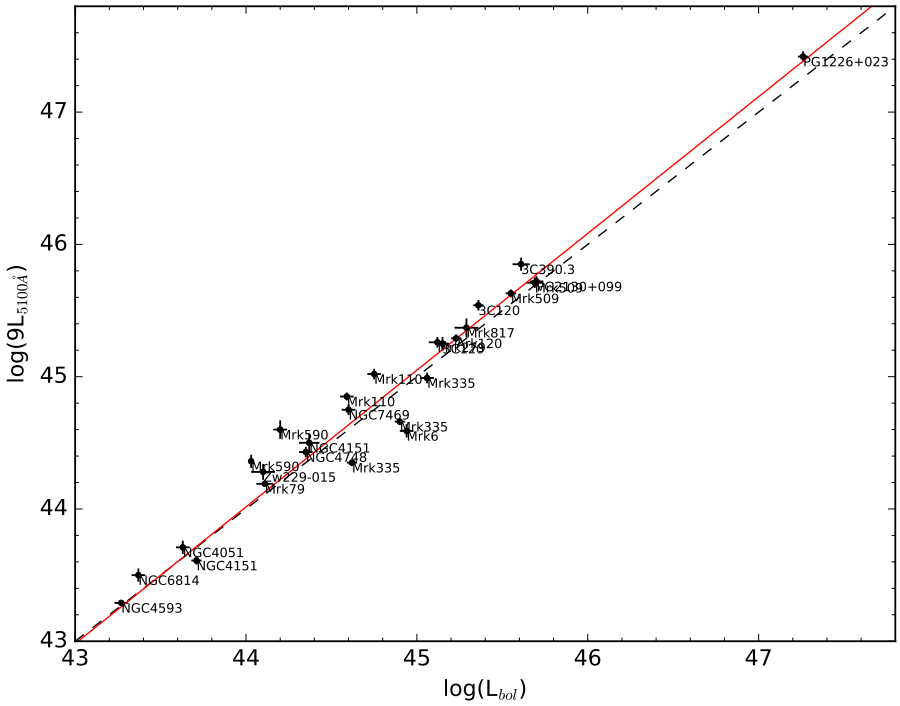

Figure 2.18: Comparison of 9 times the 5100Å specific luminosity to the bolometric luminosity. The ODR fit is shown as a solid red line and the one to one line is shown in dashed black line.

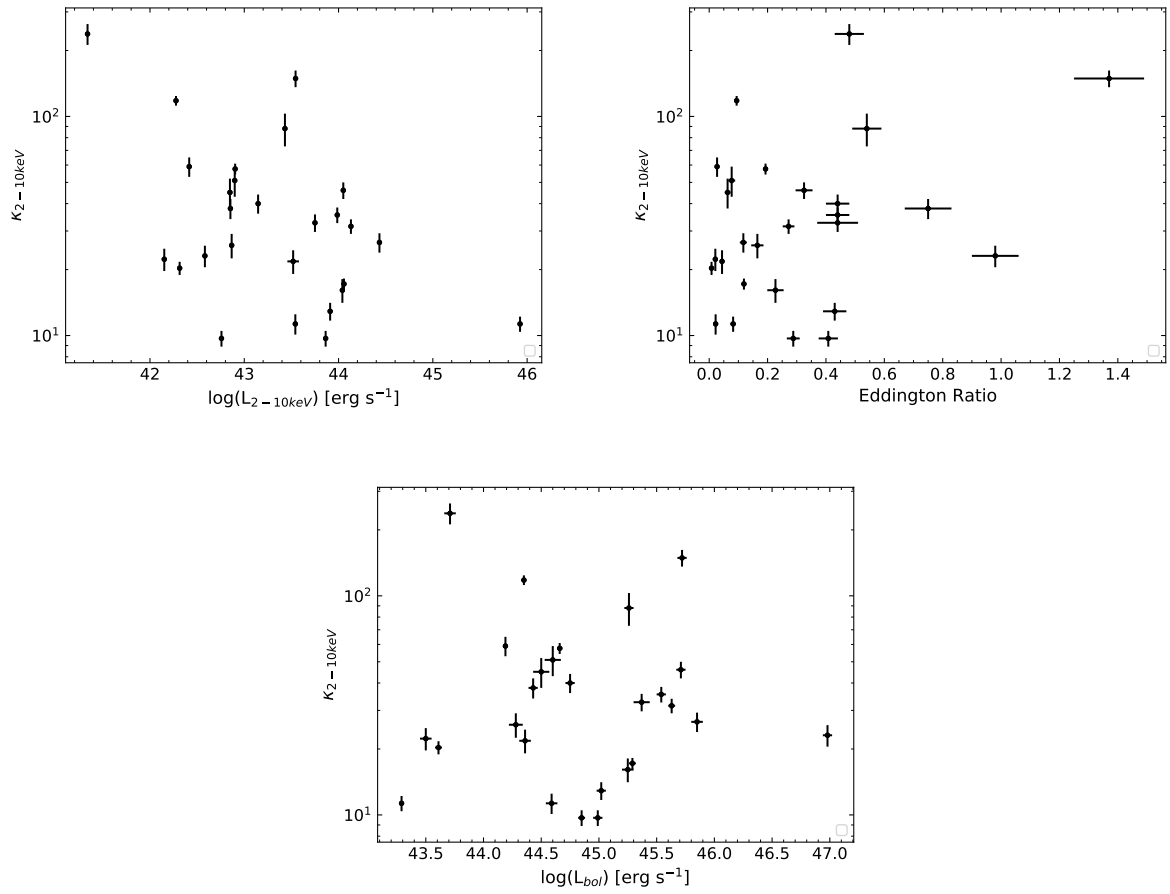

Figure 2.19: X−ray bolometric corrections versus the X−ray luminosities (top left), Eddington ratios (top right), and bolometric luminosities (bottom center).

Chapter 3

VARIABILITY STUDY WITH SWIFT

As discussed in Chapter 2, AGNs are variable objects, with the shortest variability timescales happening at the shortest wavelengths. Studying the variability of AGNs and the associated time lags between wavelengths can help constrain the size and structure of the accretion disk, in addition to other regions of the AGN structure. Intensive disk reverberation mapping campaigns have been recently undertaken to explore the size and structure of the accretion disk, requiring high temporal cadence over long durations and covering multiple wavelengths. Edelson et al. (2019) carried out such a study for four sources in our SED sample - Mrk 509, NGC 4151, NGC 4593, and NGC 5548. Between February 17, 2014 and December 15, 2017, each object was observed 200-300 times over periods of $\sim$3 weeks to 9 months, resulting in a total of 1,064 visits for the four campaigns. Edelson et al. (2019) focused on the temporal relationships of variability across wavelengths (optical to X−rays). However, these data also provide a unique opportunity for SED studies. Using the methods developed in the previous chapter, we constructed SEDs with these data and quantify how variability impacts the shape of the SED and the scatter in the quantities that are derived from the SED.

The observations were conducted by the *Neil Gehrels Swift Observatory* (*Swift*) using the X−Ray Telescope (XRT) and the Ultraviolet/Optical Telescope (UVOT). The XRT instrument has a 600×600 pixel EEV CCD-22 detector, which are the same CCDs used for MOS 1/2 on *XMM-Newton*. XRT has a $23.6'\times23.6'$ field of view and is well calibrated in the $0.2-10$ keV energy range. The UVOT design was based on the *XMM-Newton* Optical Monitor (OM) and the optics are OM flight spares. The UVOT is a modified Ritchey Chrétien telescope that, like the OM, has a 30 cm diameter primary mirror. Like the OM, it has a $17'$ square FOV and has six broadband

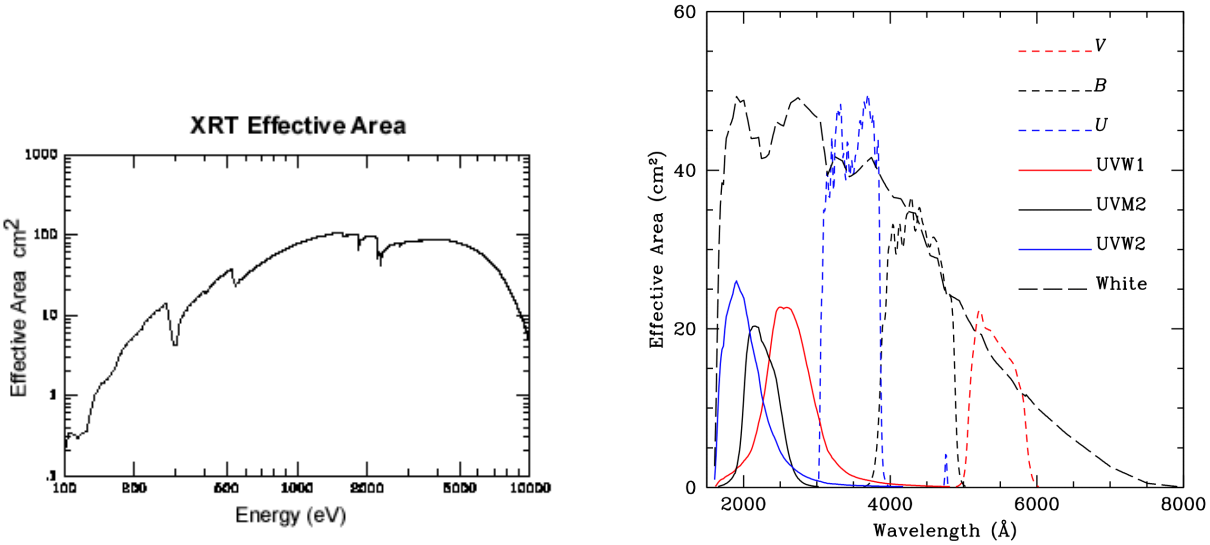

Figure 3.1: Effective area plots of *Swift*'s X–ray Telescope (XRT) on the left and Ultraviolet Optical Telescope (UVOT) on the right. Images from the *Swift* NASA website.

filters that cover a wavelength range of $1700-6500$ Å, as well as a white filter, two grisms, and a field expander. However, UVOT has two main improvements compared to the OM. The first is the increased sensitivity through the UV filters. The second is that UVOT has the ability to reduce high-voltage on the microchannel plates (MCPs) when bright objects enter the FOV on its own, so UVOT can be used without the pre-planning that the OM requires. The effective area plots of the XRT and UVOT instruments used can be seen in Figure 3.1.

3.1 *Data Reduction and Measurements*

The UVOT data were reduced and photometry was carried out by Edelson et al. (2019). For the full UVOT reduction details see Edelson et al. (2019). Here, we briefly describe the process they employed. The data were reprocessed for uniformity using `HEASOFT`[1] (v.6.22.1) and flux values were extracted using the `UVOTSOURCE` task from the `FTOOLS` package (Blackburn, 1995). The extracted flux values were corrected for aperture and coincidence losses, variations in sensitivity across the detector, and declining sensitivity over time. Quality checks were carried out to identify and remove images that had extended PSFs, incorrect astrometric corrections, and insufficient

[1] `https://heasarc.gsfc.nasa.gov/docs/software/heasoft/`

exposure times. The FWHMSIG parameter in the UVOTSOURCE task was used to obtain flux uncertainties that were more consistent with Gaussian statistics. The optical/UV photometry used a circular source region with a 5″ radius and a concentric 40″–90″ annular background region. We retrieved the flux values and errors from the VizieR Online Data Catalog[2] (Edelson et al., 2020). Due to the difference in aperture size compared to the OM observations, we ran the phot task again on the *HST* images of the 4 objects in this sample to recalculate the host galaxy flux contribution through the smaller aperture.

The X−ray data presented by Edelson et al. (2020) were binned into soft (0.3-1.5 keV) and hard (1.5-10 keV) X−rays in units of counts per second. Rather than using these definitions, which are slightly different from what we adopted and presented in Chapter 2 with the *XMM* analysis, we downloaded the X−ray data for all of the objects in the catalog using NASA's High Energy Astrophysics Science Archive Research Center (HEASARC)[3]. These data were comprised of cleaned event files that had been fully reduced and calibrated, using version 6.17 of HEASOFT, by the archive. Using the HEASOFT (v6.29) tool XSELECT, X−ray spectra were extracted from the cleaned event files using 36″ radius source and background regions, as we had adopted for the *XMM* analysis. The ARFs were created using the xrtmkarf task and the RMFs were adopted from the HEASARC Calibration Database (CALDB). The task grppha was used to ignore bad energy channels, to group the spectra to have a minimum of 25 counts per bin, and the chkey command was used to assign the RMFs, ARFs, and background spectra to the source spectra. We then fit the spectra in XSPEC using the zwabs and powerlaw models, as we had done with the *XMM* observations, and the flux values were output to ASCII files using the WData command.

After they were reduced, the X−ray observations, which were numbered by their *Swift* observation ID number, were matched to the optical/UV counterparts, which were numbered by their catalog cadence number. Due to the large number of observations, we restricted our selection to visits that included measurements through all six of the UVOT filters. This left us with 778 visits

[2] https://vizier.cfa.harvard.edu/
[3] https://heasarc.gsfc.nasa.gov/cgi-bin/W3Browse/swift.pl

Table 3.1. Sources and Data Utilized

Object	Date Range (MJD)	Number of Observations	Mean Sampling Interval (days)	Percent of Original Sample used
Mrk509	57829.85584 - 58102.48981	208	1.313	80.9%
NGC4151	57438.04468 - 57505.83057	222	0.305	68.9%
NGC4593	57582.91730 - 57605.38991	131	0.172	67.5%
NGC5548	56705.98256 - 56829.92040	217	0.571	74.6%

for the four sources, or 73% of the total visits. The number of observations utilized, percent of the sample used for each object, and the mean sampling intervals are listed in Table 3.1.

The SED fitting script was edited to loop over all of the visits for each object. As we did with the individual *XMM* observations, we first removed the host contribution, line emission, and applied Galactic reddening corrections and carried out an initial SED fit focusing solely on the optical and UV points to determine $\alpha_{\rm opt}$. Using the calculated $\alpha_{\rm opt}$ and the α_0 adopted in Chapter 2, we determined the E(B-V) values for each visit and applied the intrinsic reddening correction. The reddened and dereddened fits, as well as a mean fit, for each object can be seen in Figure 3.2.

After all of the corrections were applied, we constructed full SEDs for each visit using the method described in Chapter 2. All SEDs and the mean SEDs for each object can be seen in Figure 3.3. As noted previously, the SED fits of NGC 5548 do not include a NIR data point.

After constructing each of the SEDs, we calculated the same quantities as described in Chapter 2 — bolometric luminosity, Eddington ratio, and $\alpha_{\rm ox}$. We also calculated the specific optical (5100Å) and X–ray ($2-10$ keV) luminosities. To visualize these results, we created histograms using the `pyplot.hist` package. To quantify the scatter, we calculated the 68% confidence interval on the median value of each measurement using the `numpy.percentile` function, which computes the q–th percentile of the data along the specified axis.

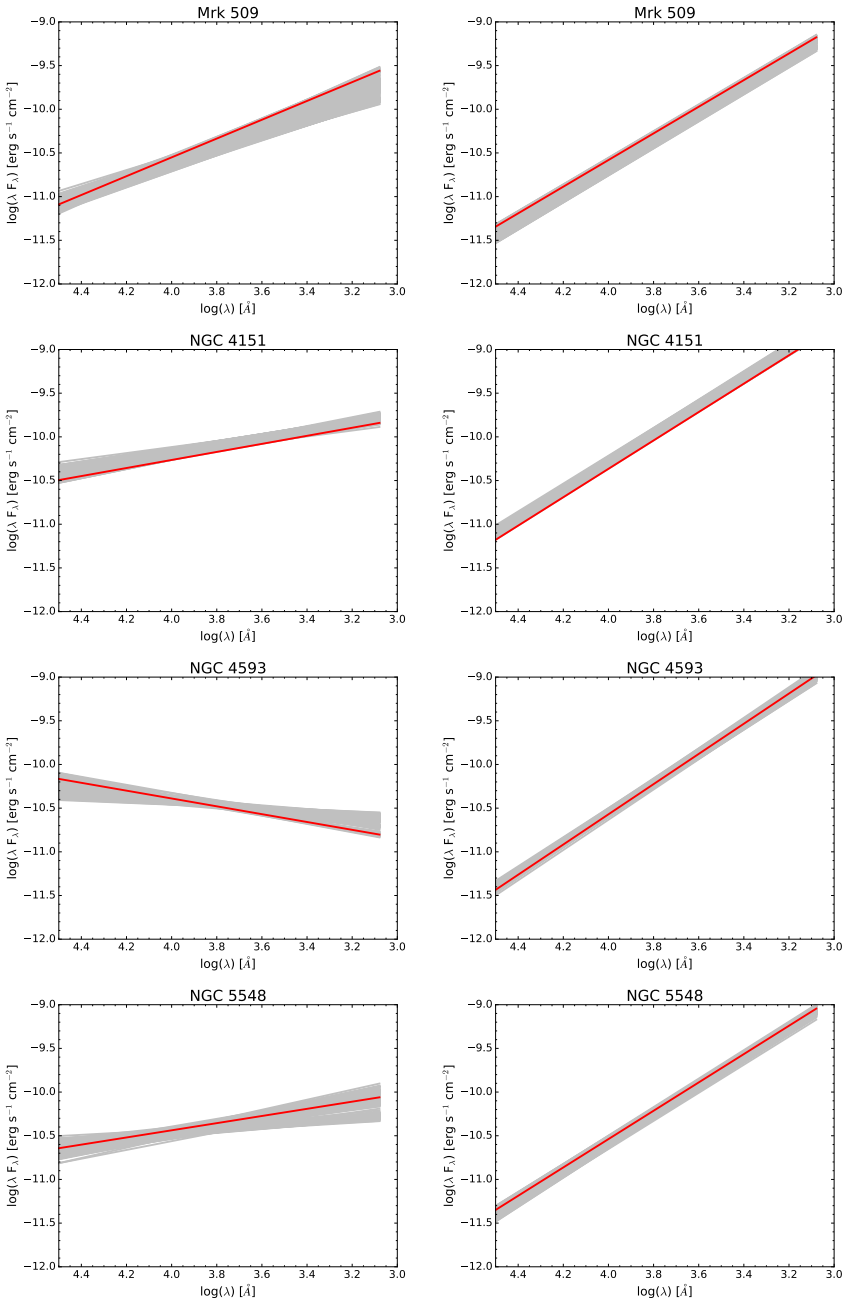

Figure 3.2: Comparison of corrections to the optical/UV regime of the SED. The left-hand figures show the optical/UV fits, in gray, for all visits with only host contribution and line emission corrected. The right-hand figures, show the optical/UV fits, also in gray, with all corrections. The solid red lines are the average fit over all visits.

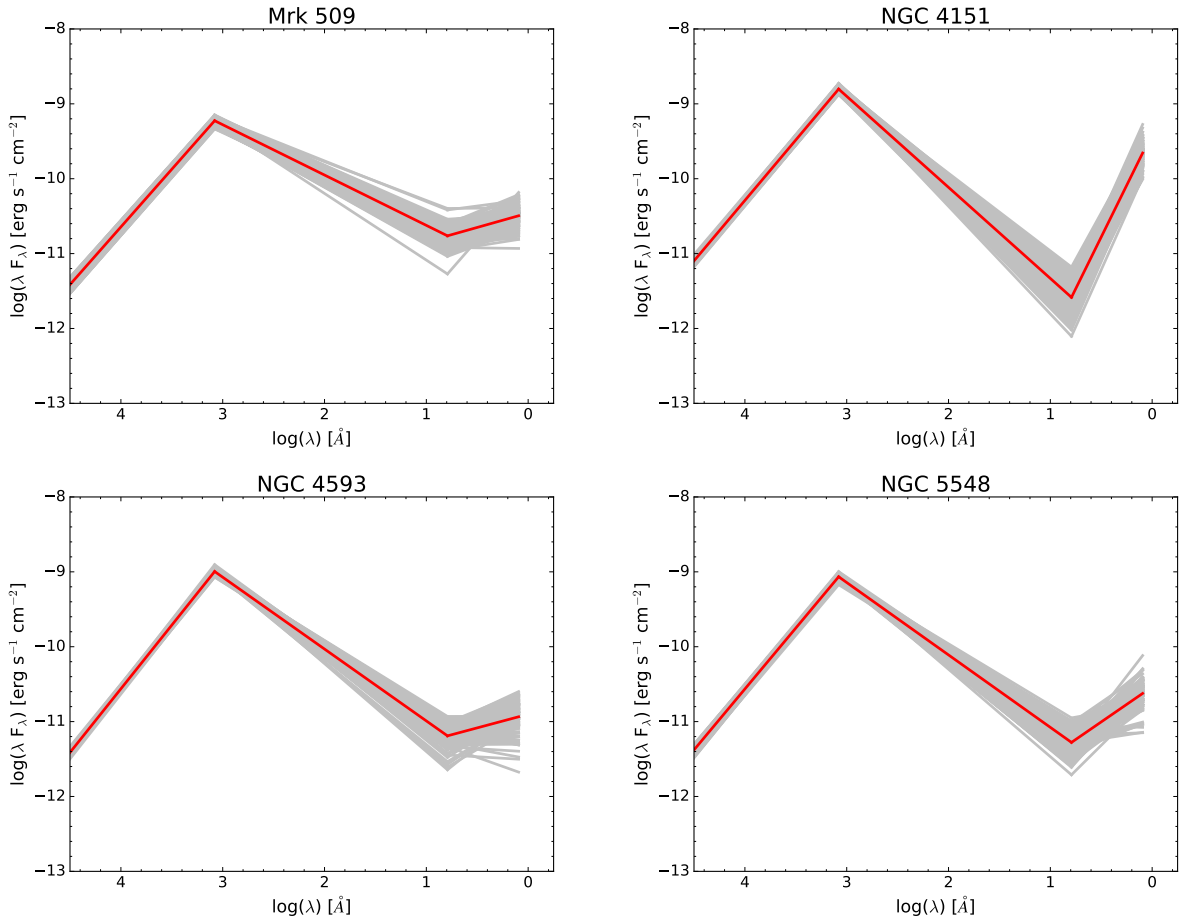

Figure 3.3: SEDs for all visits. The SED of each visit is shown in gray, with the mean SED for all visits shown in red.

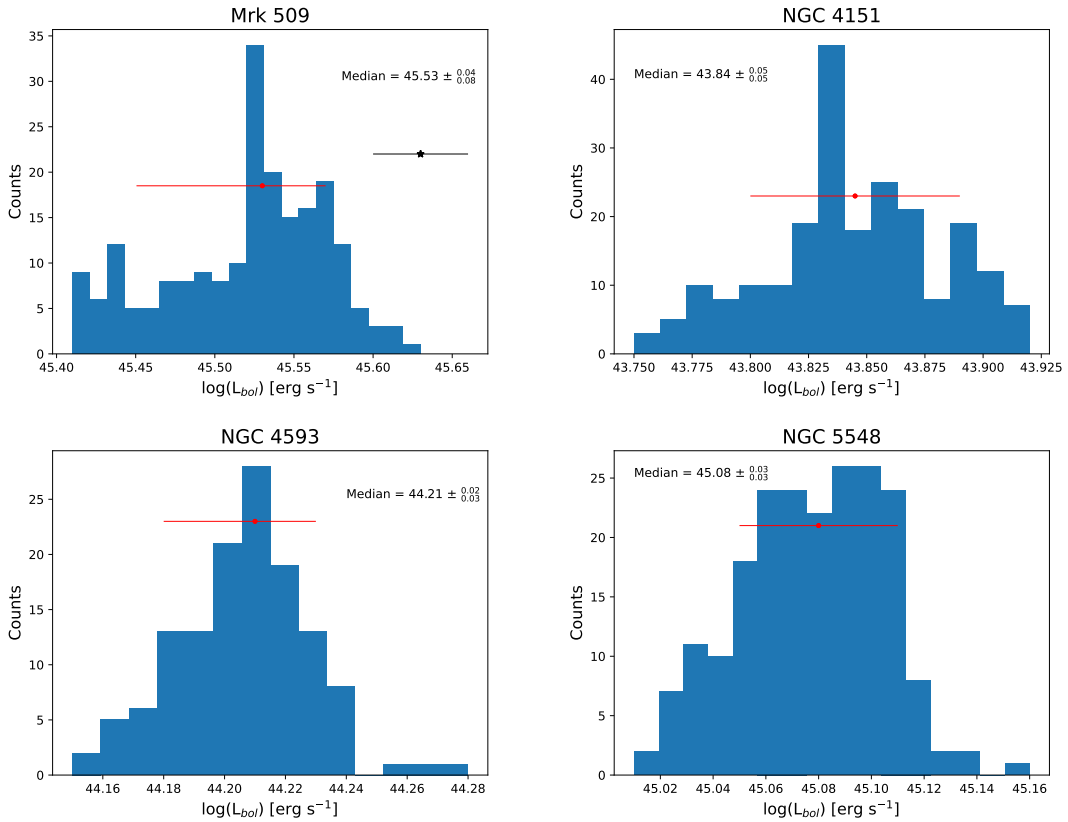

Figure 3.4: Distributions of bolometric luminosities. The median value and the 68% confidence intervals are shown in red. The L_{bol} value from the 2009 *XMM* observation of Mrk 509 is plotted as a black star. *XMM* L_{bol} values for the remaining objects were outside of the Swift distributions and are not included in the plots.

3.1.1 *Bolometric luminosity*

Comparing the distributions of bolometric luminosities shown in Figure 3.4, Mrk 509, which had the longest Swift campaign of the sources, has the largest spread of values, while NGC 4593, which had the shortest campaign, has the smallest spread in L_{bol} values. With the exception of the 2009 observation of Mrk 509, all of the bolometric luminosity values found in Chapter 2 are outside of the *Swift* distributions. The 2006 observation of Mrk 509, the 2003 observation of NGC 4151, and 2000 observation of NGC 5548 values are greater than the *Swift* measurements, while the value from the *XMM* observation of NGC 4593 in 2000 is lower than the *Swift* distribution.

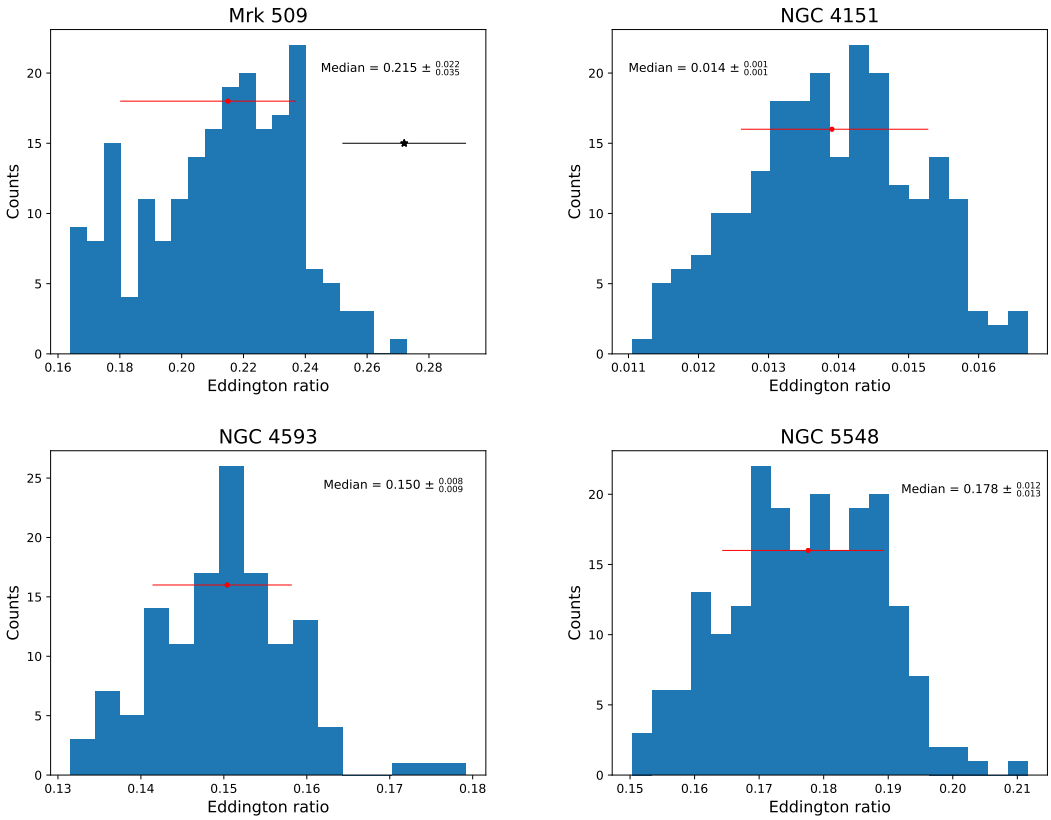

Figure 3.5: Distributions of Eddington ratios. The median value and the 68% confidence intervals are shown in red. The Eddington ratio calculated from the 2009 *XMM* observation of Mrk 509 is plotted as a black star. The *XMM* Eddington ratios for the remaining objects were outside of the Swift distributions and are not included in the plots.

3.1.2 *Eddington ratios*

As expected from what is seen in the distributions of the bolometric luminosity, Mrk 509 has the largest range in its Eddington ratio and also has the most skewed distribution. All *Swift* Eddington ratio distributions are shown in Figure 3.5. The Eddington ratio for the 2009 *XMM* observation of Mrk 509 is included in the figure, however the other *XMM* values are outside of the distribution. The 2006 observation of Mrk 509, the 2003 *XMM* NGC 4151 observation, and the 2000 observation of NGC 5548 values are greater than the *Swift* values. The Eddington ratio from the observation of NGC 4593 in 2000 is lower than the *Swift* distributions.

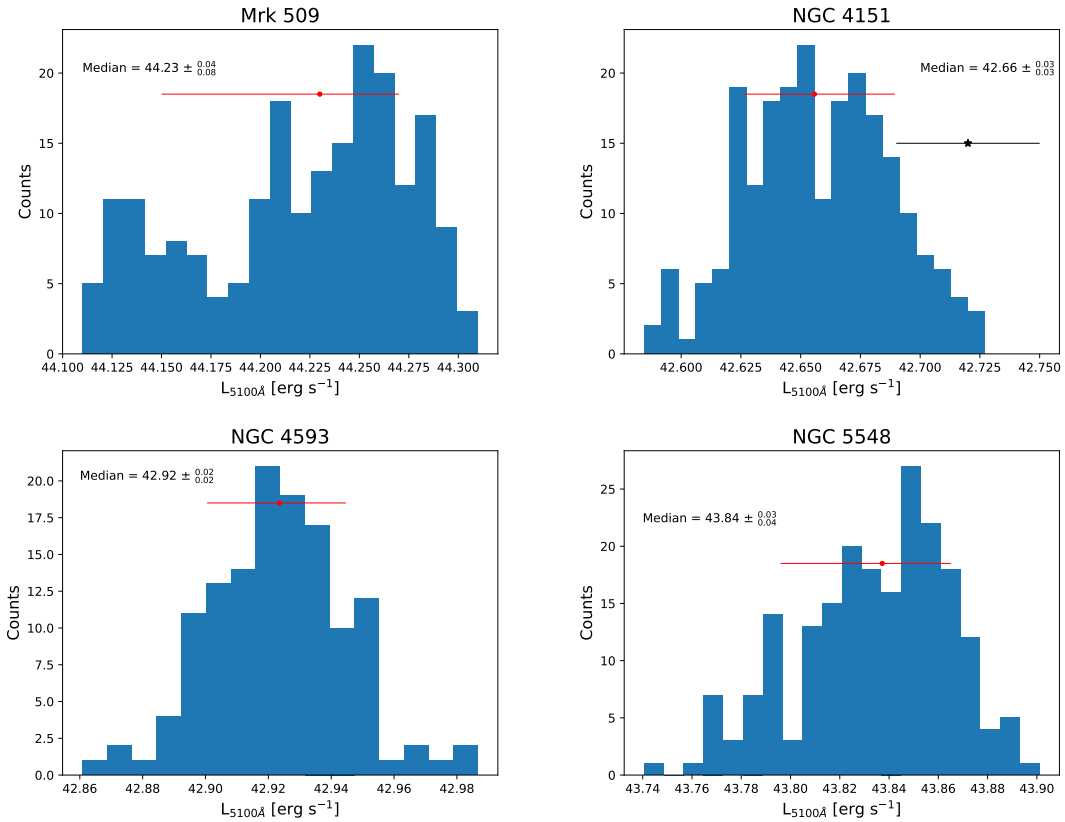

Figure 3.6: Distributions of the specific optical (5100Å) luminosities. The median value and the 68% confidence intervals are shown in red. The specific optical luminosity calculated from the 2015 *XMM* observation of NGC 4151 is plotted as a black star. The *XMM* specific optical luminosities for the remaining objects were outside of the Swift distributions and are not included in the plots.

3.1.3 *5100Å Luminosities*

The distribution of specific luminosities at 5100Å (L_{5100}) are shown in Figure 3.6. The Mrk 509 distribution shows slight evidence of being bimodal. The L_{5100} value from the *XMM* observation of NGC 4151 in 2015 is also shown in the figure, but the other *XMM* values were outside of the *Swift* distributions. The L_{5100} measurement for the 2009 *XMM* observation of Mrk 509, the 2003 observation of NGC 4151, and the 2000 observation of NGC 5548 observations were greater than the *Swift* distribution, while the value from the 2000 observation of NGC 4593 was less than the *Swift* distribution.

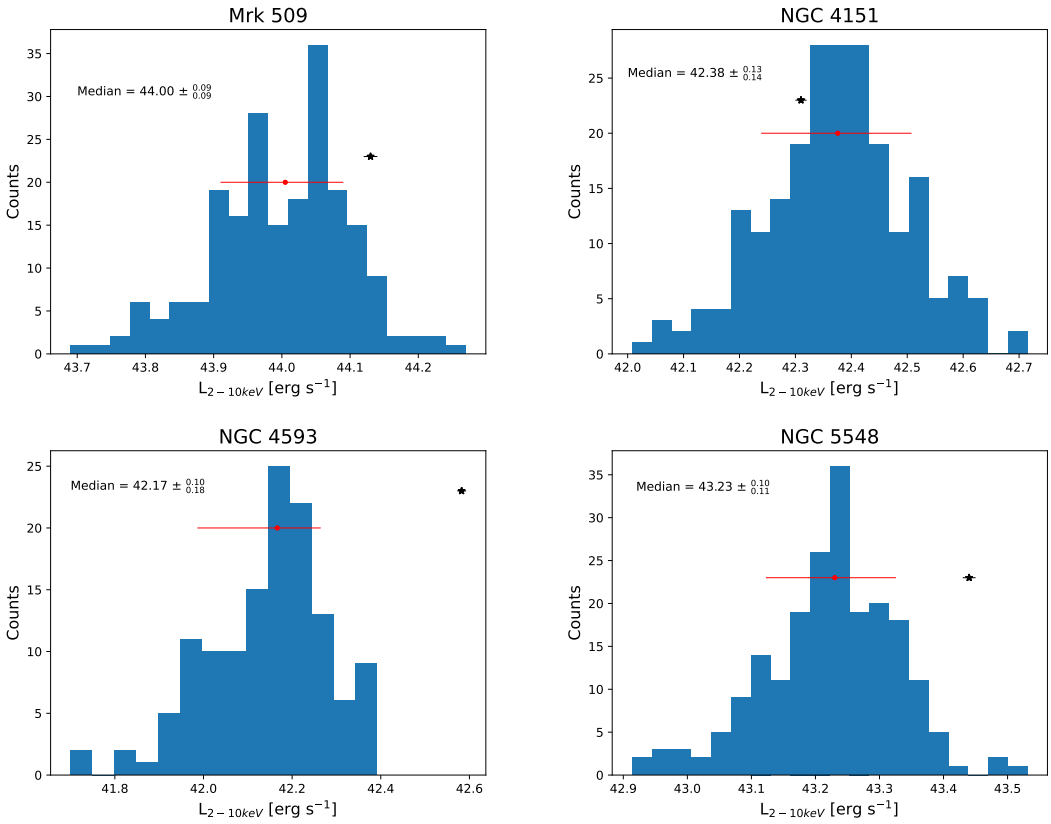

Figure 3.7: Distributions of the specific X–ray (2 – 10 keV) luminosities. The median value and the 68% confidence intervals are shown in red. The specific X–ray luminosities calculated from *XMM* observations are plotted as black stars. The 2009 *XMM* observation of Mrk 509 and the 2003 observation of NGC 4151 are not shown.

3.1.4 2 – 10 *keV Luminosities*

The distributions of the specific X–ray (2 – 10 keV) luminosities and the X–ray luminosities from *XMM* observations are shown in Figure 3.7. Most of the *XMM* X–ray luminosities were included in the figure. The values from the *XMM* observations of Mrk 509 in 2006 and of NGC 4151 in 2003 were greater than the *Swift* distributions. The X–ray luminosities from XMM for the 2009 observation of Mrk 509, and the 2000 observations of NGC 4593 and NGC 5548 were greater than the median of the *Swift* distributions, while the *XMM* value for the 2015 observation of NGC 4151 *XMM* observation falls within the confidence interval of the *Swift* measurements.

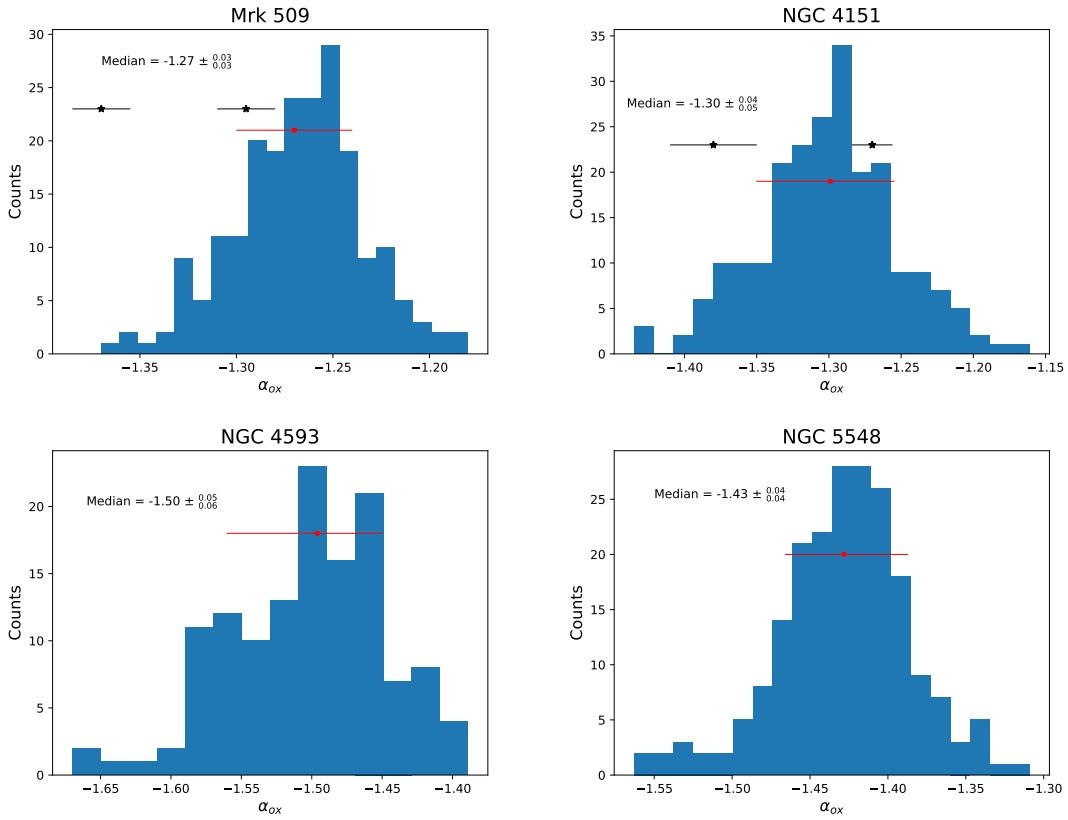

Figure 3.8: Distributions of α_{ox} values. The median value and the 68% confidence intervals are shown in red. The α_{ox} values from all four *XMM* observations of Mrk 509 and NGC 4151 are plotted as black stars. The *XMM* α_{ox} measurements from observations of NGC 4593 and NGC 5548 in 2000 were outside of the *Swift* distributions and are not included in the plot.

3.1.5 α_{ox} *distributions*

Figure 3.8 displays the distributions of the *Swift* α_{ox} values. The *XMM* α_{ox} values from both Mrk 509 observations and both NGC 4151 observations are also shown in the figure. The *XMM* values for observations of NGC 4593 and NGC 5548 in 2000 were less negative than the *Swift* distribution and were not included in the figure. We additionally compared how the median *Swift* α_{ox} values fit in the α_{ox}–L_{2500} relationship determined by Steffen et al. (2006) (see Figure 3.9). The specific 2500Å luminosity used in the figure was determined by taking the median of the values calculated from the SEDs of each visit for each campaign.

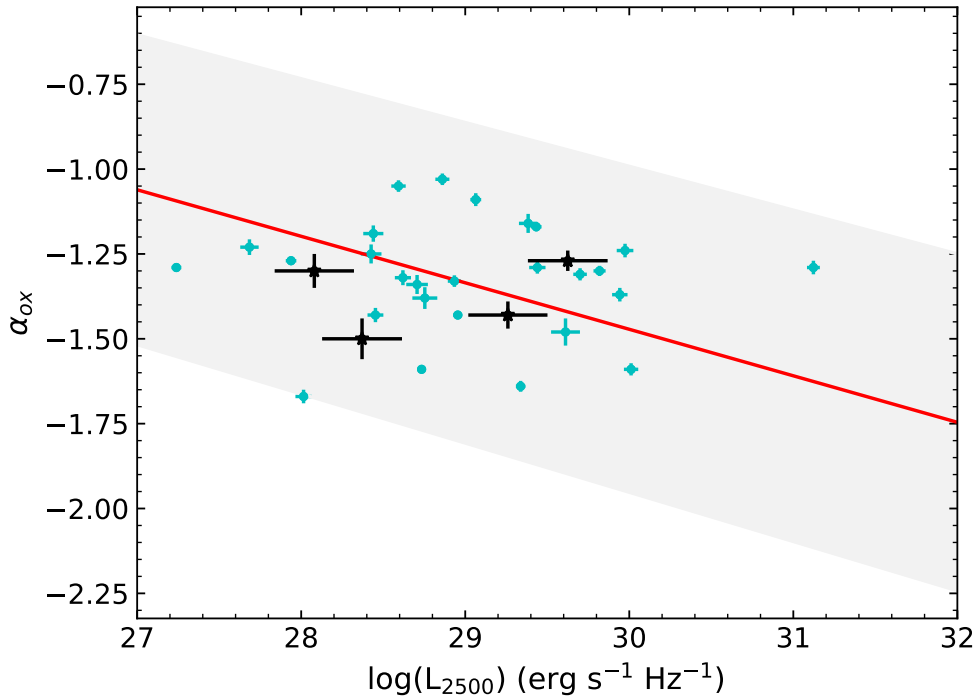

Figure 3.9: Specific luminosity at 2500Å versus α_{ox}. For comparison, the best fit for the α_{ox}–L_{2500} relationship determined from 333 AGNs by Steffen et al. (2006) is show by the solid red line and the error is shaded in gray. The values from *XMM-Newton* observations are plotted in cyan, while the median α_{ox} values and the median specific luminosity values from the *Swift* campaigns are shown in black.

3.1.6 *E(B-V) distributions*

The E(B-V) magnitude distributions are shown in Figure 3.10. The values of the 2009 observation of Mrk 509 and the 2000 observation of NGC 5548 E(B-V) fall within the confidence interval of the *Swift* distributions. The other *XMM* values are outside of the *Swift* distributions. All of the other values were greater than the *Swift* distributions. Despite its classification as a 'bare' AGN (albeit with a warm absorber), Mrk 509 displays quite a bit of scatter in its E(B-V) value, again evidence that warm absorbers may be linked with optical/UV reddening.

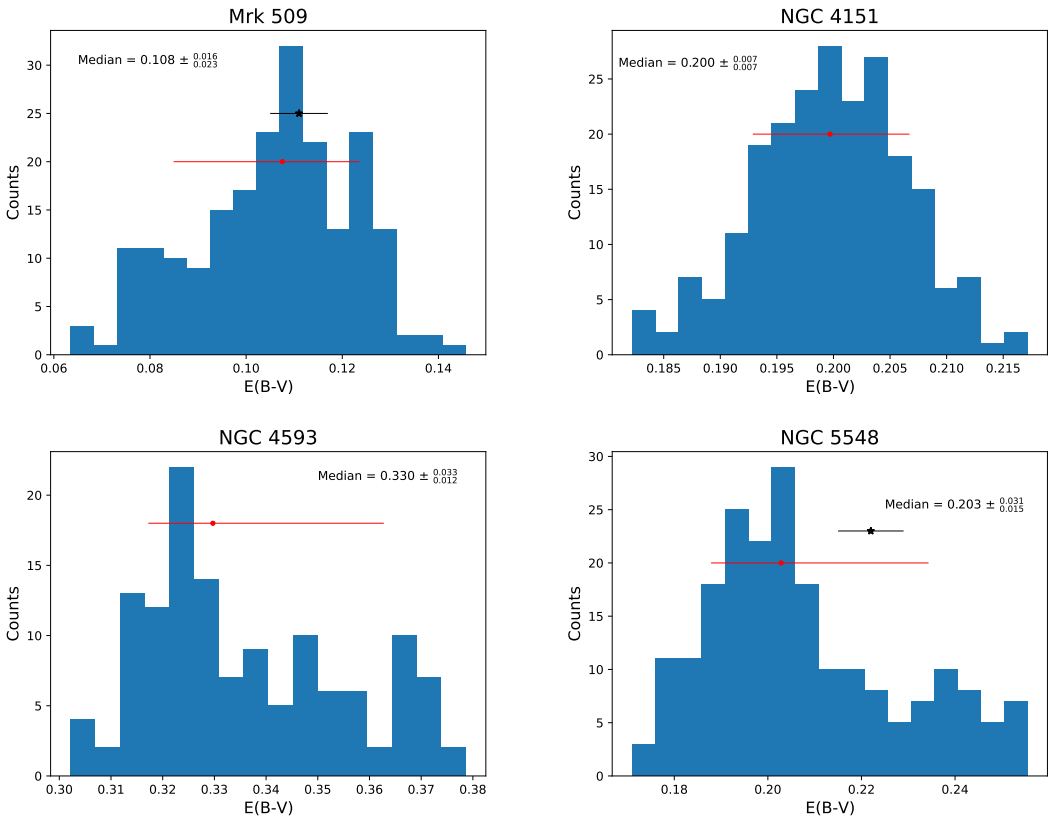

Figure 3.10: Distributions of the E(B-V) magnitude values. The median value and the 68% confidence intervals are shown in red. The E(B-V) value from the 2009 observation of Mrk 509 and 2000 observation of NGC 5548 *XMM* observation values are plotted as black stars. The *XMM* E(B-V) measurements for the other sources were outside of the Swift distributions and are not included in the plots.

3.1.7 *Uncertainties on Distributions*

Each of the values derived have a corresponding uncertainty that may not be adequately reflected by the widths of the histograms. For example, the Eddington luminosity is calculated using a single black hole mass value, however that mass has an associated uncertainty. To explore this issue further, we calculated a second distribution of Eddington ratios for Mrk 509, but instead of using a single black hole mass, we created a normal distribution of black hole mass values characterized by a mean value and width that matches the black hole mass and uncertainties measured for Mrk 509. We then calculated each Eddington ratio using the measured bolometric luminosity and a random draw from the distribution of masses. As seen in Figure 3.11, accounting for the uncertainty in the black hole mass in this way results in a slight increased spread in Eddington ratios. However, despite the widening of the wings, there was not a significant change in the median or the 68% confidence interval, with the single mass method having a median and confidence intervals of $0.215^{+0.022}_{-0.035}$ and the random mass draw having values of $0.214^{+0.028}_{-0.025}$. We note that we have not, however, accounted for the additional factor of $2-3$ uncertainty in reverberation-based masses when a population-average scaling factor is adopted (e.g., Peterson et al. 2004). Incorporating that additional uncertainty would likely have a noticeable effect on the spread of Eddington ratio values.

3.2 *Variaibility on several year timescales*

In the previous section, we discussed the distribution of values for each *Swift* campaign and how those values compared to the *XMM* values. However, many of the *XMM* values were outside of the *Swift* distributions. We compared the median *Swift* values for each source to the *XMM* observations from Chapter 2 to get a larger-scale view of the effects of AGN variability on the values typically derived from SEDs. These comparisons are shown in Figures 3.12 through 3.15.

Mrk 509 Mrk 509 shows an almost factor of 2 decrease in bolometric luminosity, and therefore a significant decrease in the Eddington ratio, over the 11 year period covered by the *XMM* and *Swift* data. It shows a factor of $\sim$3 decrease in its specific optical luminosity. The continual decrease is

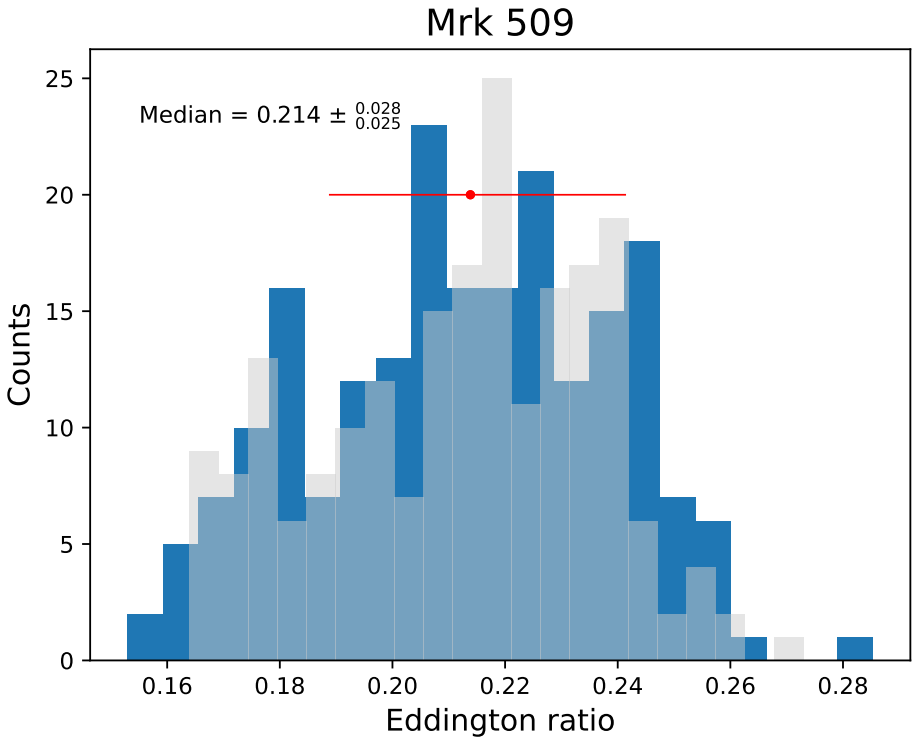

Figure 3.11: Histogram of the Eddington ratio for Mrk 509 with random draws when calculating the Eddington luminosities (blue). The median value and the 68% confidence intervals are shown in red. Rather than using a single mass value, a normal distribution of black hole mass values was created, based on the measured black hole mass and its uncertainties, and random draws from the mass distribution were used when calculating the Eddington luminosity for each bolometric luminosity measurement. The distribution using a single mass value is overplotted in gray.

not seen in the X–rays, where there is a slight increase followed by a decrease. The value of α_{ox} consistently increases (becomes less negative), while the E(B-V) value decreases from 2006 to 2009 and then remains constant.

NGC 4151 The bolometric luminosity dropped by nearly a factor of 8 between the 2003 and 2015 *XMM* observations. It then increased by a factor of $\sim$1.7 in the year between the 2015 *XMM* and the 2016 *Swift* observations. The significant drop between *XMM* observations is also seen in the X–rays and the optical luminosities. The α_{ox} value slightly increases (becomes less negative) and

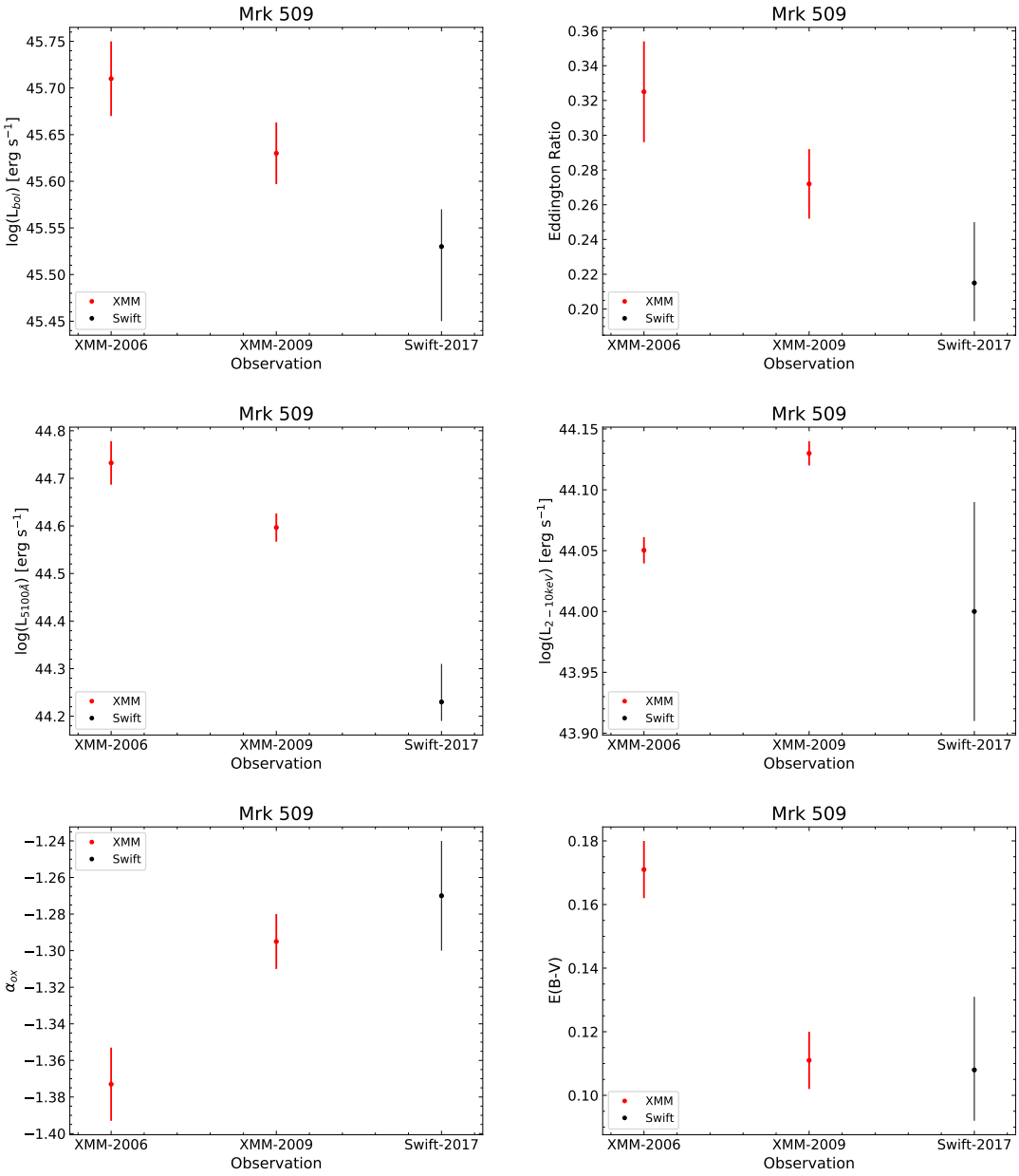

Figure 3.12: Comparison of bolometric luminosity, Eddington ratio, optical luminosity at 5100Å, $2-10$ keV X–ray luminosity, $\alpha_{\rm ox}$, and E(B-V) values from the 2006 and 2009 *XMM* observations and median values from the 2017 *Swift* campaign of Mrk 509.

the E(B-V) slightly decreases across the observations, although the values derived from the 2003 and 2016 observations are formally consistent with the value derived from the 2015 *XMM* data.

NGC 4593 The bolometric luminosity of NGC 4593 increases by a factor $\sim$1.8 in the 16 years between the *XMM* and *Swift* observations. The Eddington ratio reflects this increase, and an increase in the optical luminosity is also seen. However, the X−rays show a factor of $\sim$2.5 decrease in luminosity over the same time period. The $\alpha_{\rm ox}$ value also decreases (becomes more negative), while there is a slight increase in the E(B-V) value.

NGC 5548 NGC 5548 shows a decrease in X-ray luminosity and $\alpha_{\rm ox}$, while the other quantities are consistent within the uncertainties. The SED fits for NGC 5548 do not include a near-IR flux measurement to anchor the red tail of the optical-UV power law, and the importance of those measurements is clearly demonstrated with this exercise through the much larger uncertainties on most quantities derived for NGC 5548.

From the *Swift* distributions we are able to quantify the effects of short-term variability on the derived bolometric luminosity and and Eddington ratio for each source based on the median value and the 68% confidence interval. Furthermore, each individual measurement has an associated uncertainty. We determined the typical fractional uncertainty for each of the four AGNs on their bolometric luminosities and Eddington ratios, and we list them in Table 3.2 along with the fractional spread in values from variability. The typical uncertainty on the measurements of bolometric luminosity range from $6-14\%$, while the typical uncertainty on the Eddington ratios are $\sim 15\%$. These are nearly the same as the spread in values based on the variability of each of the four AGNs, although NGC 4151 is notable for showing a larger spread in values of L_{bol} from variability than the typical measurement uncertainties. By combining the two effects, we can estimate a lower limit on the uncertainties that may be assumed for SED studies comprised of observations collected non-simultaneously but relatively close in time (a few months): $10-20\%$ for L_{bol} and 20% for the Eddington ratio.

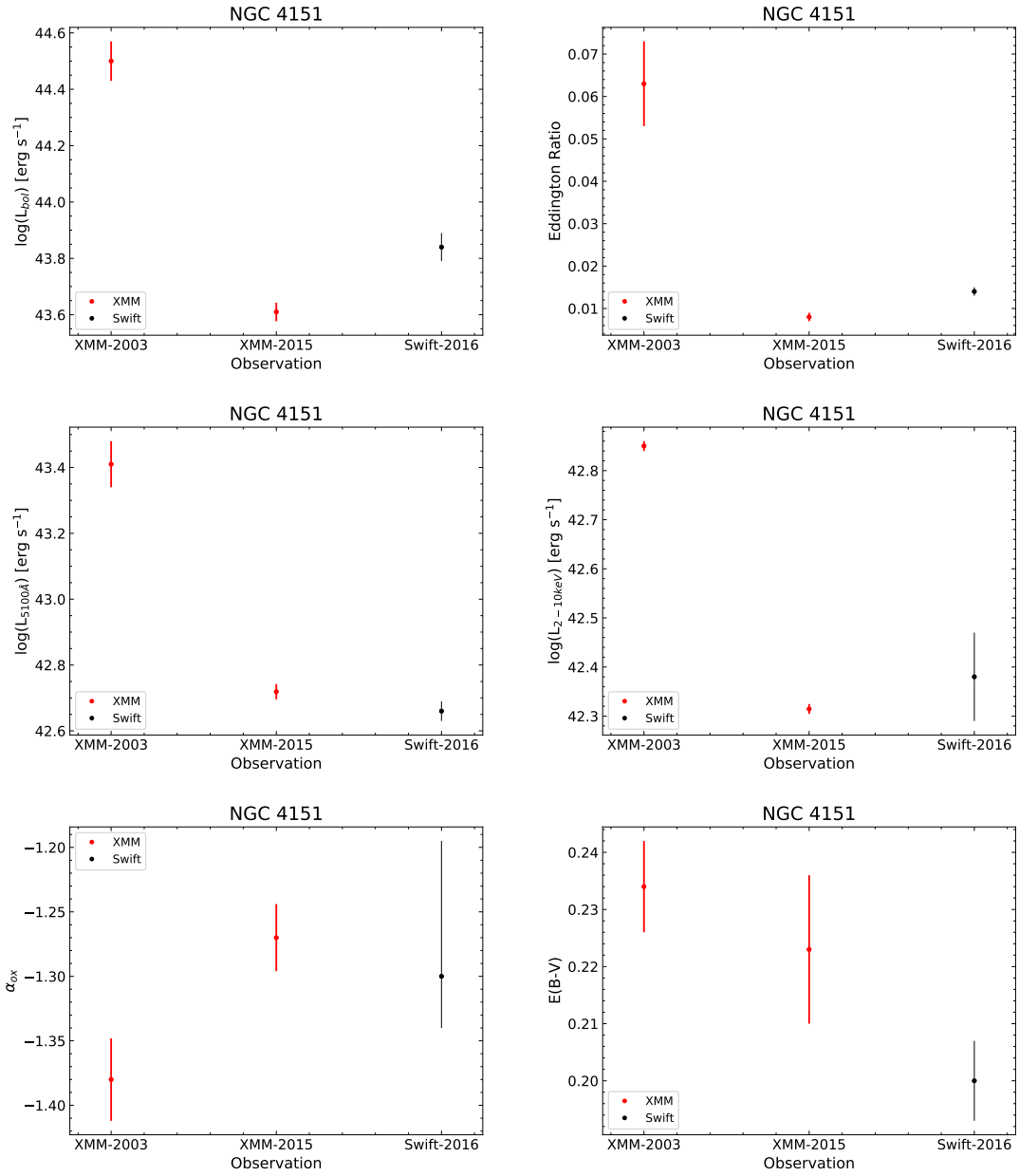

Figure 3.13: Comparison of bolometric luminosity, Eddington ratio, optical luminosity at 5100Å, $2-10$ keV X–ray luminosity, $\alpha_{\rm ox}$, and E(B-V) values from the 2003 and 2015 *XMM* observations and median values from the 2016 *Swift* campaign of NGC 4151.

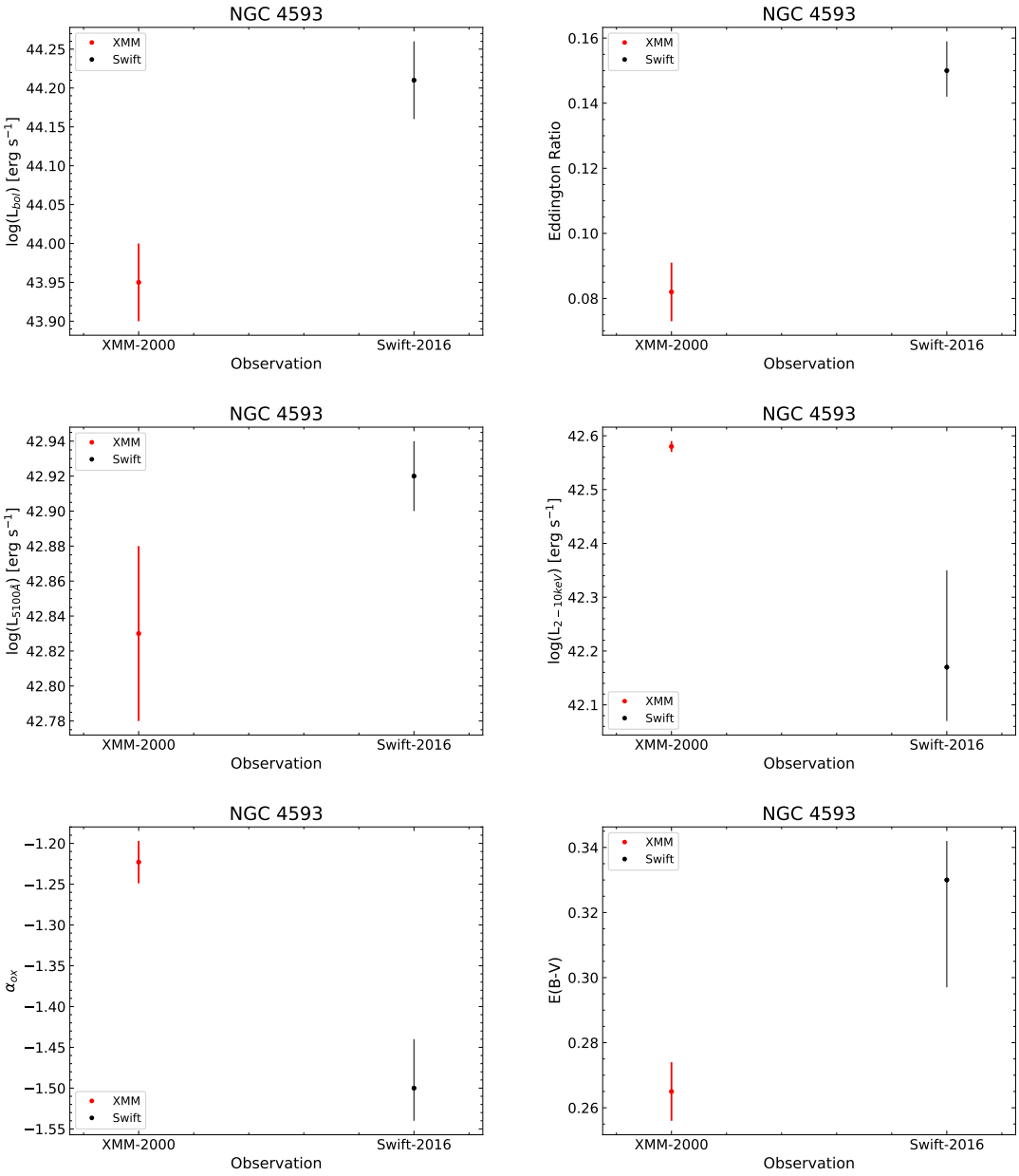

Figure 3.14: Comparison of bolometric luminosity, Eddington ratio, optical luminosity at 5100Å, $2-10$ keV X−ray luminosity, $\alpha_{\rm ox}$, and E(B-V) values from the 2000 *XMM* observation and median values from the 2016 *Swift* campaign of NGC 4593.

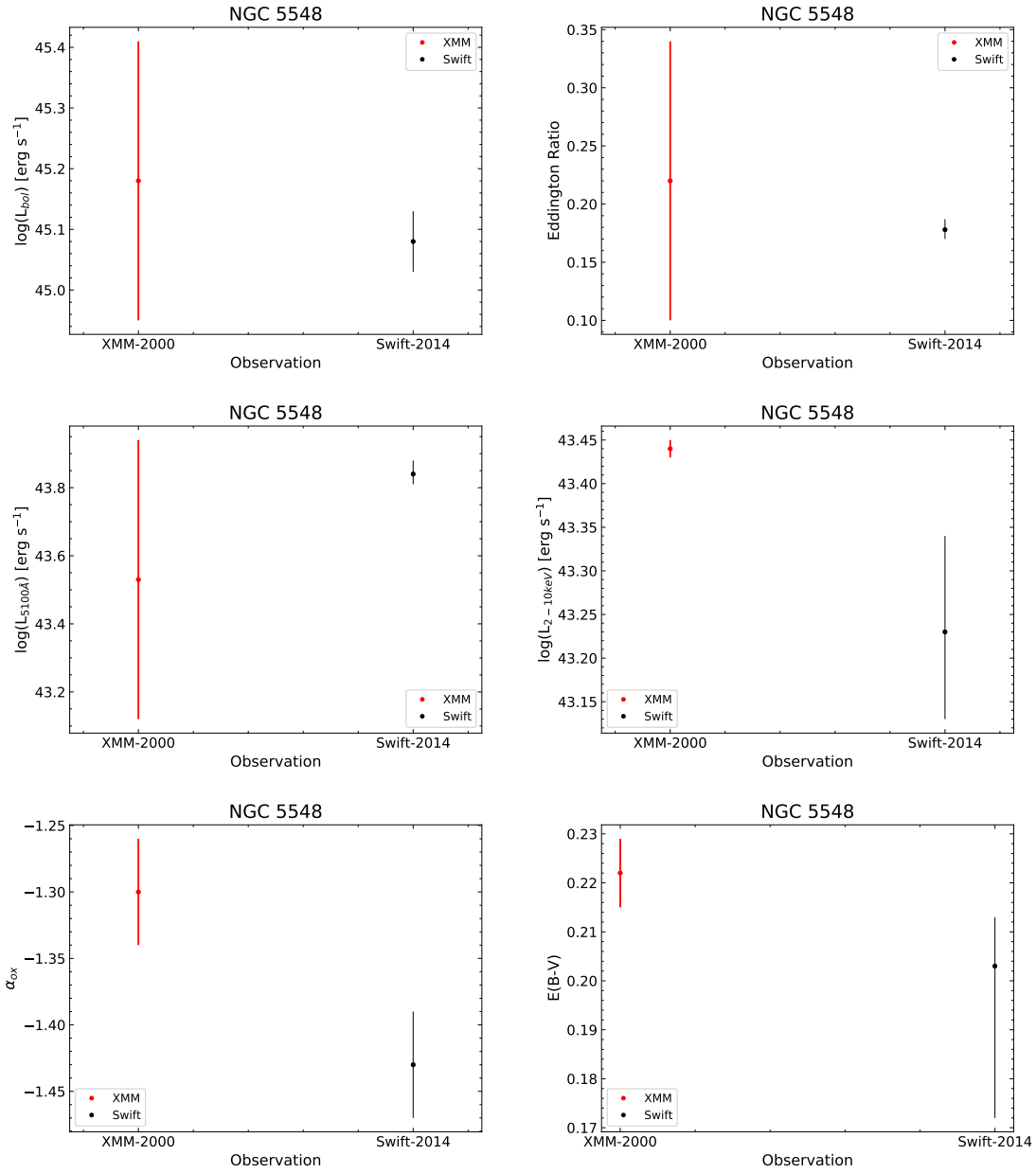

Figure 3.15: Comparison of bolometric luminosity, Eddington ratio, optical luminosity at 5100Å, $2-10$ keV X−ray luminosity, $\alpha_{\rm ox}$, and E(B-V) values of the 2000 *XMM* observation and median values from the 2014 *Swift* campaign of NGC 5548.

Table 3.2. Error budget table

Object	L_{bol} Variability	λ_{Edd} Variability	L_{bol} Measurement	λ_{Edd} Measurement	L_{bol} Combined	λ_{Edd} Combined
Mrk 509	0.148	0.135	0.133	0.135	0.199	0.190
NGC 4151	0.122	0.136	0.071	0.153	0.141	0.205
NGC 4593	0.059	0.149	0.057	0.149	0.082	0.211
NGC 5548	0.072	0.145	0.070	0.144	0.100	0.204

Note. — Columns 2 and 3 display fractional spread in bolometric luminosity and Eddington ratio (λ_{Edd}) values caused by variability, while columns 4 and 5 display the median fractional measurement uncertainty on L_{bol} and λ_{Edd} for all of the *Swift* observations of the four AGNs. Columns 6 and 7 show the combined effect of variability and measurement uncertainties.

However, as we saw when comparing the *Swift* measurements with the *XMM* measurements, when these timescales increase to several years in between, the lower limits are blown out of the water (e.g., the factor of 2 change in the bolometric luminosity of Mrk 509 and NGC 4593, anti-correlated behavior in optical and $X-$ray wavelengths). These trends exemplify the necessity for simultaneous, or at least relatively close together in time measurements (within several months) when constructing SEDs. If observations are stitched together from significantly different times, it would be an inaccurate representation of what was actually occurring in the system, and would result in very inaccurate estimates of bolometric luminosity and Eddington ratio, as well as any other quantities derived from the SED.

Chapter 4

DISCUSSION

4.1 *Comparison to Vasudevan & Fabian (2009)*

In our sample we have 12 sets of *XMM* observations that were also analyzed by Vasudevan & Fabian (2009) (hereafter VF09). In comparing our derived values with theirs (e.g., bolometric luminosity, Eddington ratio, etc) there are two considerations to be examined: (1) how did the change in SED construction method affect the derived values, and (2) how did updates to the supplemental information, such as black hole mass or galaxy distance, affect the derived values?

We first investigated how the change in SED construction method affected the derived values. VF09 used a blackbody curve to fit their optical/UV data and did not apply any corrections to the OM data. Thus their analysis neglects to account for host galaxy flux, internal reddening, and the contribution of emission lines to the UV and optical aperture fluxes. The blackbody model assumes the existence of a big blue bump in the unobservable EUV, and in some cases, they only constrained their blackbody model with a single OM measurement. In this work, we adopted power law fits that are determined by observations and do not guess at the location or strength of a big blue bump. We have corrected for known contributions to the UV and optical fluxes that do not arise from the accretion disk, and we have restricted the analysis to only those objects that have at least 2 OM measurements plus a NIR measurement (or in the case of NGC 5548 which does not yet have a near-IR measurement, 3 OM measurements). Figure 4.1 compares the bolometric luminosities and Eddington ratios from our method with those reported by VF09, with all other relevant quantities — black hole mass, distance — held the same. In 9 out of 12 cases (the exceptions being 3C120,

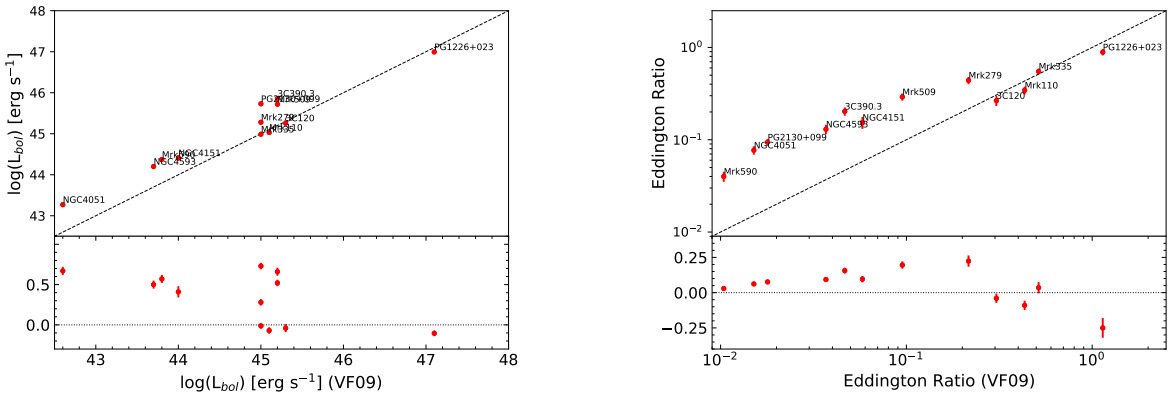

Figure 4.1: Comparison of bolometric luminosity (left) and Eddington ratio (right) from VF09 with the values obtained using our SED fitting method but adopting the mass and distance values used by VF09 (plotted in log space). Residuals are shown in the bottom panels of each plot, plotted in linear space. The one-to-one relation is indicated by the dashed black line.

Mrk 110, and PG 1226+023) our method derives a greater bolometric luminosity than was reported by VF09. This is also see in the Eddington ratios, where 9 out of 12 cases show an increase in the values determined by our method compared to what was reported by VF09. In considering the numerous changes between our method and that of VF09, removal of the host galaxy and emission line fluxes and not assuming the presence of an unseen big blue bump in the EUV would all serve to decrease both bolometric luminosity and Eddington ratio. On the other hand, correcting for internal reddening would instead increase both values.

We also examined the effect on the derived values of updates to the black hole masses and galaxy distances in our sample. In Figure 4.2, we again show the bolometric luminosities and Eddington ratios from our method and those reported by VF09. Red points are the same as in Figure 4.1, with the black points including updates that account for the best current measurements of black hole mass and galaxy distance, and the difference between them displayed by the vertical connecting lines. In most cases, the values are fairly similar to what is shown in Figure 4.1. However, 4 objects had either a significant change in their distance (NGC 4051, NGC 4151, and NGC 4593) or black hole mass (PG 2130+099). NGC 4051 and NGC 4151 both now have Cepheid distance measurements (Yuan et al. 2020; Yuan et al. 2021) and NGC 4593 has a Tully-Fisher distance (Robinson et al.,

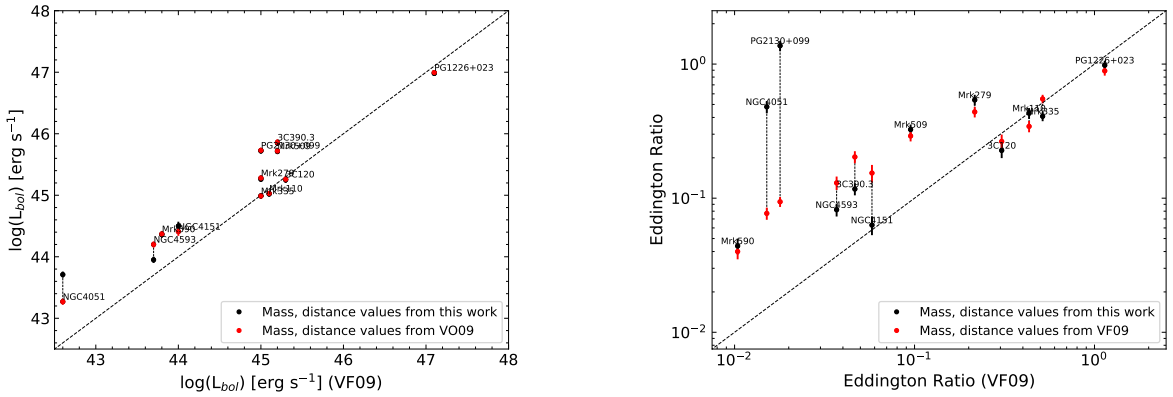

Figure 4.2: Comparison of bolometric luminosity (left) and Eddington ratio (right) from VF09 with the values obtained using our SED fitting method. The data points in red were calculated using the mass and distance measurements used by VF09, while the black points were calculated using updated mass and distance measurements. Measurements for the same object are connected by a vertical black line. The one-to-one relation is indicated by the dashed black line.

2021), while Grier et al. (2012) updated the mass of PG 2130+099. Updated distance measurements will strongly influence the bolometric luminosity, which goes like D^2. The distance measurement of NGC 4051 increased by $\sim$40%, the distance of NGC 4593 decreased by $\sim$34%, and the distance of NGC 4151 increased by $\sim$11%. The impact of these improved distance measurements will also carry over to Eddington ratios. Furthermore, the Eddington luminosity is dependent on mass, so any mass changes will also impact the Eddington ratio, as we see in the case of the Eddington ratio for PG 2130+099. The mass measurement determined by Grier et al. (2012) is approximately an order of magnitude smaller than the Peterson et al. (2004) value used by VF09, causing an order of magnitude increase in the Eddington ratio when the updated mass is incorporated.

In Figure 4.3, we compare our final derived values of bolometric luminosity and Eddington ratio with the values reported by VF09. Based on the small sample compared here, it appears that the quantities derived for low-luminosity AGNs are more sensitive to the exact methods employed when constructing an SED, and therefore require additional care and attention to detail. And the importance of measuring accurate distances for low-z sources, which will be preferentially low-luminosity AGNs, is clearly seen here in the large changes that result from the distance updates.

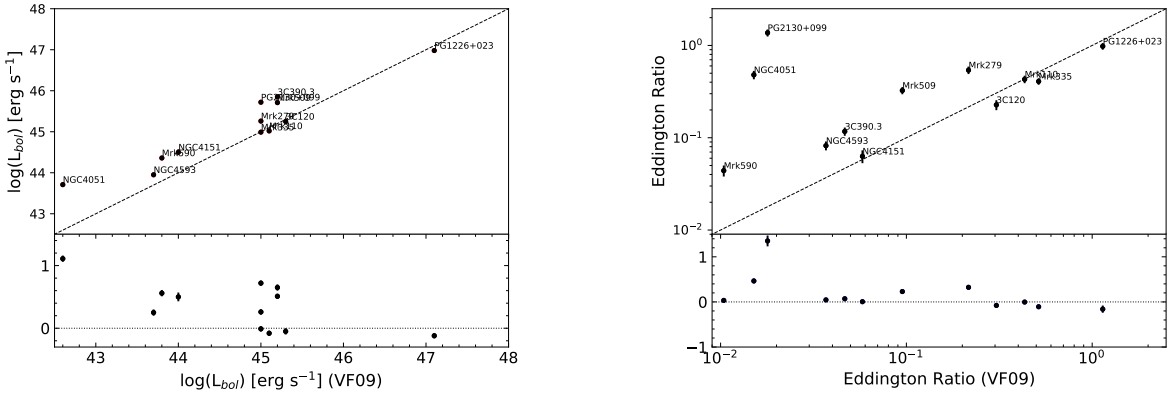

Figure 4.3: Comparison of bolometric luminosity (left) and Eddington ratio (right) from VF09 with the values obtained using our SED fitting method with updated mass and distance values (plotted in log space). Residuals are shown in the bottom panel of each plot, plotted in linear space. The one-to-one relation is indicated by the dashed black line.

4.2 *Comparing to X−Cigale*

In addition to comparing our values to those reported by VF09, we also explored how different model assumptions affect derived SED values by comparing our results for Ark 120 to results determined with X−CIGALE (Yang et al., 2020). X−CIGALE is an updated version of the Code Investigating GALaxy Emission (CIGALE) (Boquien et al., 2019), which is a python based SED fitting program that works by building composite stellar populations from simple stellar populations and star formation histories along with dust and nebular ionization models to create galaxies. It also includes models for the IR to X−ray properties of AGNs, like the optical depth of the torus, inclination of the AGN, extinction laws for polar dust, and the X−ray photon index. X−CIGALE uses all of the framework of CIGALE, but includes the ability to fit X−ray data as broadband or 'boxcar-shaped filter' photometry. The model begins by calculating a star formation history and stellar population based on an initial mass function. It then sets nebular ionization parameters and line widths, and attenuation of stellar and nebular emission. The AGN IR to UV data are fit by a model called SKIRTOR (Stalevski et al., 2016), which is a clumpy two phase torus model. Parameters for SKIRTOR include the optical depth of the torus, density parameters, inclination, viewing angle, AGN luminosity fraction in the IR, extinction law, E(B-V), and the temperature and

emissivity of polar dust. All of the described SKIRTOR parameter values are chosen by the user, within certain ranges. For example, the inclination of the AGN may be set between 0° and 90° in increments of 10°. The model also corrects for redshift and IGM absorption.

To model Ark 120, we used the raw uncorrected fluxes due to the galaxy, emission, and reddening contributions being built into X–CIGALE. There are 39 parameters that must be set by the user, so for convenience, the full set of fit parameters for this model are described in Appendix B. We note that we assumed a Salpeter initial mass function, a nebular ionization parameter of $log(U) = -2.0$. We selected an AGN inclination of 30° and the AGN fractional contribution to the total IR luminosity to be 0.5. The initial fit produced a total luminosity of $\log L_{bol} = 45.19 \pm 0.02$ erg/s, which is comparable to our bolometric luminosity value of $\log L_{bol} = 45.29 \pm 0.03$ erg/s. However, Figure 4.4 shows there is still a fair amount of scatter in the residuals near the optical and UV flux measurements and the reduced χ^2 of 7.0 suggests that fine tuning of the individual SKIRTOR and galaxy creation parameters is still required.

4.3 *Impacts of Corrections*

4.3.1 *Host Correction*

As we discussed in Chapter 2, we expect and do see a decrease in host galaxy contribution for AGNs at larger distances. The process of determining accurate host galaxy contributions requires high resolution imaging, which for very large samples is not observationally or computationally realistic. So we considered whether a trend may be seen in our sample that could be used to estimate the correction, and thus provide a mechanism for large samples to efficiently account for host galaxy contributions. We examined the host galaxy contribution as a function of distance for the XMM OM filters V, B, and U. The V contributions were determined from *HST* images and the B and U values were extrapolated from the V band using `calcphot` and galaxy template spectra. To quantify the trend in the data, we carried out a linear regression arriving at the following relationships:

$$\log(V_{correction}) = (-0.74 \pm 0.02)\log(z) + (-15.79 \pm 0.03) \tag{4.1}$$

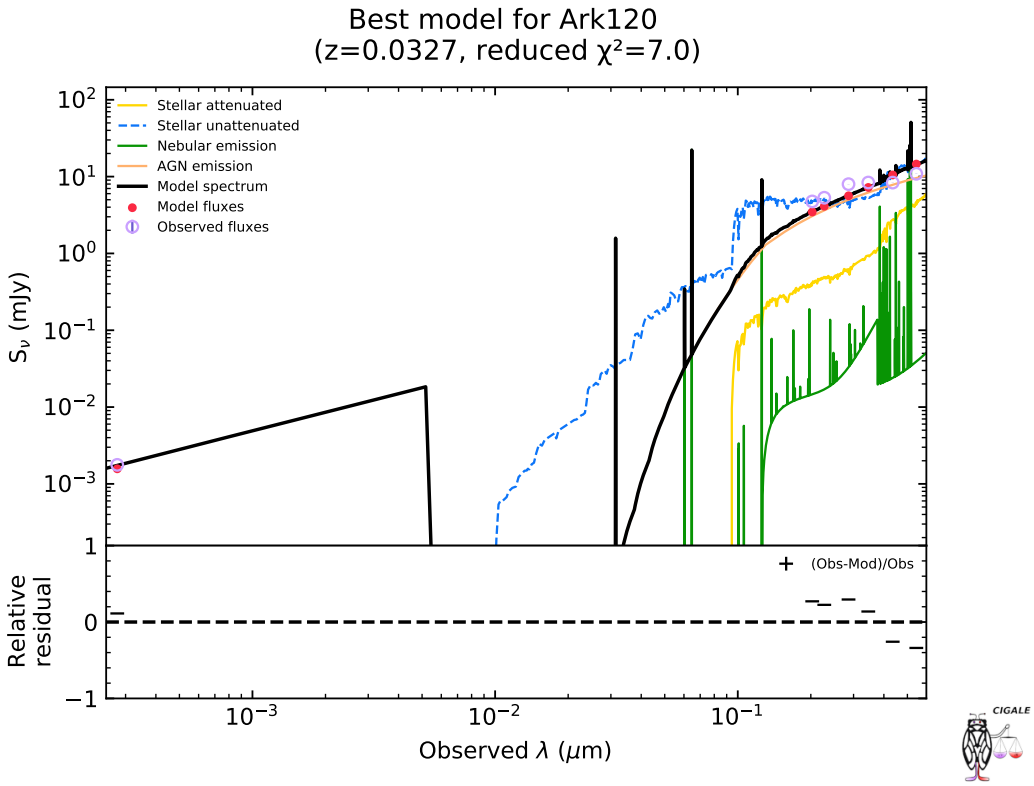

Figure 4.4: SED of Ark 120 produced by X–Cigale. The SED was modeled using a Salpeter initial mass function, the SKIRTOR model, and the 2 – 10 keV boxcar filter for the X–ray flux.

$$\log(B_{correction}) = (-0.86 \pm 0.14)\log(z) + (-16.23 \pm 0.03) \tag{4.2}$$

$$\log(U_{correction}) = (-0.89 \pm 0.0.02)\log(z) + (-16.77 \pm 0.02) \tag{4.3}$$

which are shown as the solid lines in Figure 4.5. An initial fit examining the galaxy flux as a function of $\log z$ showed a power law solution, so we refit the relationships in log-log space. As expected, we find a larger correction in each filter for closer galaxies, and we find that for a galaxy at a specific distance, the host galaxy correction in V is larger than B, which in turn is larger than U. While the measured galaxy fluxes that we used here assumed a circular aperture of radius $6''$, a grid of host galaxy fluxes as a function of distance and aperture size would be needed to provide the most value to the community.

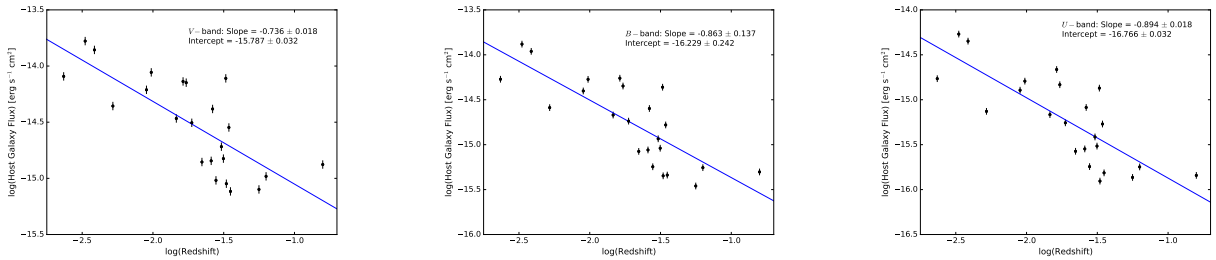

Figure 4.5: Host galaxy flux of the 23 objects in our sample for the V (left), B (center), and U bands (right) versus redshift. The host flux values were determined through a $6''$ radius aperture.

4.3.2 *Line Emission Correction*

For the line emission corrections adopted in our work, we were only able to find high quality UV-optical spectra for a small number of our sample. For the others, we estimated a "typical" emission line contribution through each filter at the redshift of the target.

However, even with the few optical-UV spectra available to us, we see evidence for a potentially large scatter in emission line contributions. Crenshaw et al. (2001) propose that the reddened UV spectrum of NGC 3227 is caused by the presence of a 'luke-warm' absorber, which can be placed $>$100 pc from the nucleus. Turner et al. (1992) and Leighly et al. (1994) reported NGC 6814 as also having a warm absorber. However, analyzing observations collected with *NuSTAR*, Tortosa et al. (2018) report that the effects of the absorber are not visible in the X−rays. Mrk 509 also has evidence for a warm absorber (Kaastra et al. 2012; García et al. 2019) but is considered a bare AGN, where 'bare' is defined as showing little to no intrinsic absorption in the X−rays. In Figure 4.6, we plot the STIS spectra of these three AGNs, and note that they all show differences, particularly in the UV. The spectrum of Mrk 509 does not appear strongly reddened, while the spectra of NGC 3227 and NGC 6814 do. But even between the two reddened spectra, there are differences. NGC 6814 is less reddened in the UV and the Fe II features surrounding the Mg II emission ($\sim$2800Å) are much stronger in NGC 6814 than in NGC 3227. It is difficult to disentangle line emission and reddening

and reaffirms that even though objects are experiencing similar situations (e.g., absorbers) they can manifest very differently in the spectra.

Ideally, we would determine the line emission contribution from high resolution spectra of each source, but even if such spectra were available, the variable nature of AGNs would cause further complications. The first complication is the Baldwin effect (Baldwin, 1977), which is the relationship between emission and continuum where the equivalent width of an emission line decreases as the continuum increases. The equivalent width can be approximated by taking the ratio of the total line flux and the continuum level beneath the emission line (Peterson, 1997). The sources for which we had STIS spectra cover a relatively small luminosity range, so for any object at either extreme of the luminosity range (like blazar PG1226+023), the line emission estimates adopted here may not be very representative of the actual line emission contribution. It would be useful to compile a library of AGN spectra covering a wide range of luminosities to account for this effect when correcting line emission. The second complication is that, even if such a library is compiled, absorption signatures, including narrow and broad absorption of the emission lines as well as warm absorbers, are observed to come and go with time (e.g., Kriss et al. 2019; De Marco et al. 2020; Mehdipour et al. 2022). The best scenario for correcting for line emission would be to obtain simultaneous optical/UV spectra for objects of interest, rather than relying on broad-band flux estimates.

4.3.3 *Reddening Correction*

Only two AGNs in our sample are expected to have minimal amounts of reddening along our sight lines - Ark 120 and Mrk 110. The mean E(B-V) value of the sample is 0.149. Combining this with the Milky Way reddening curve, the average flux correction to the $UVW2$ filter is a factor of 3.6. Of the 12 objects in common between our analysis and that of VF09, only three AGNs did not show an increase in bolometric luminosity in our work compared to VF09, and all three were found to have E(B-V)$<$ 0.1. The biggest uncertainty in determining a reddening correction is the intrinsic accretion disk slope. We adopted a single slope for the intrinsic accretion disk emission in

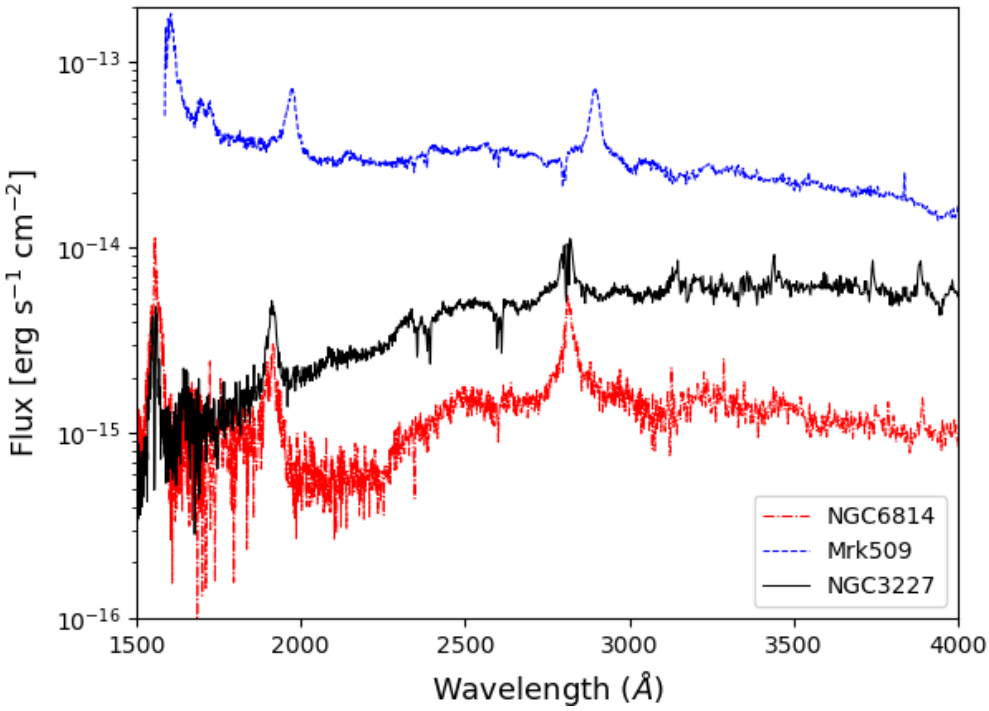

Figure 4.6: Comparison of optical/UV spectra of AGNs with absorbers.

all the objects in our sample based on two bare AGNs without any known absorbers. However, it is not clear that a single intrinsic slope is an appropriate assumption for all AGNs. Considering a schematic of the optical to X–ray SED of a disk dominated AGN shown in Figure 4.7 (Collinson et al., 2015), the slope of the left-hand gray dashed line, which indicate what part of the accretion disk that are visible to observers, is dependent on where the peak temperature of the disk (shown in red) is located. So if that peak is shifted to higher or lower temperatures, the slope is going to change. And the temperature of the accretion disk is expected to be dependent on both mass and accretion rate (Peterson, 1997), so realistically, the intrinsic accretion disk slope is going to be intrinsic to that particular system rather than to all AGN accretion disks.

There is also the conventional expectation that AGNs get 'bluer when brighter', which would further negate the assumption that even a single AGN always has the same intrinsic accretion disk slope. To test whether there is any evidence for the AGNs in our sample becoming 'bluer when

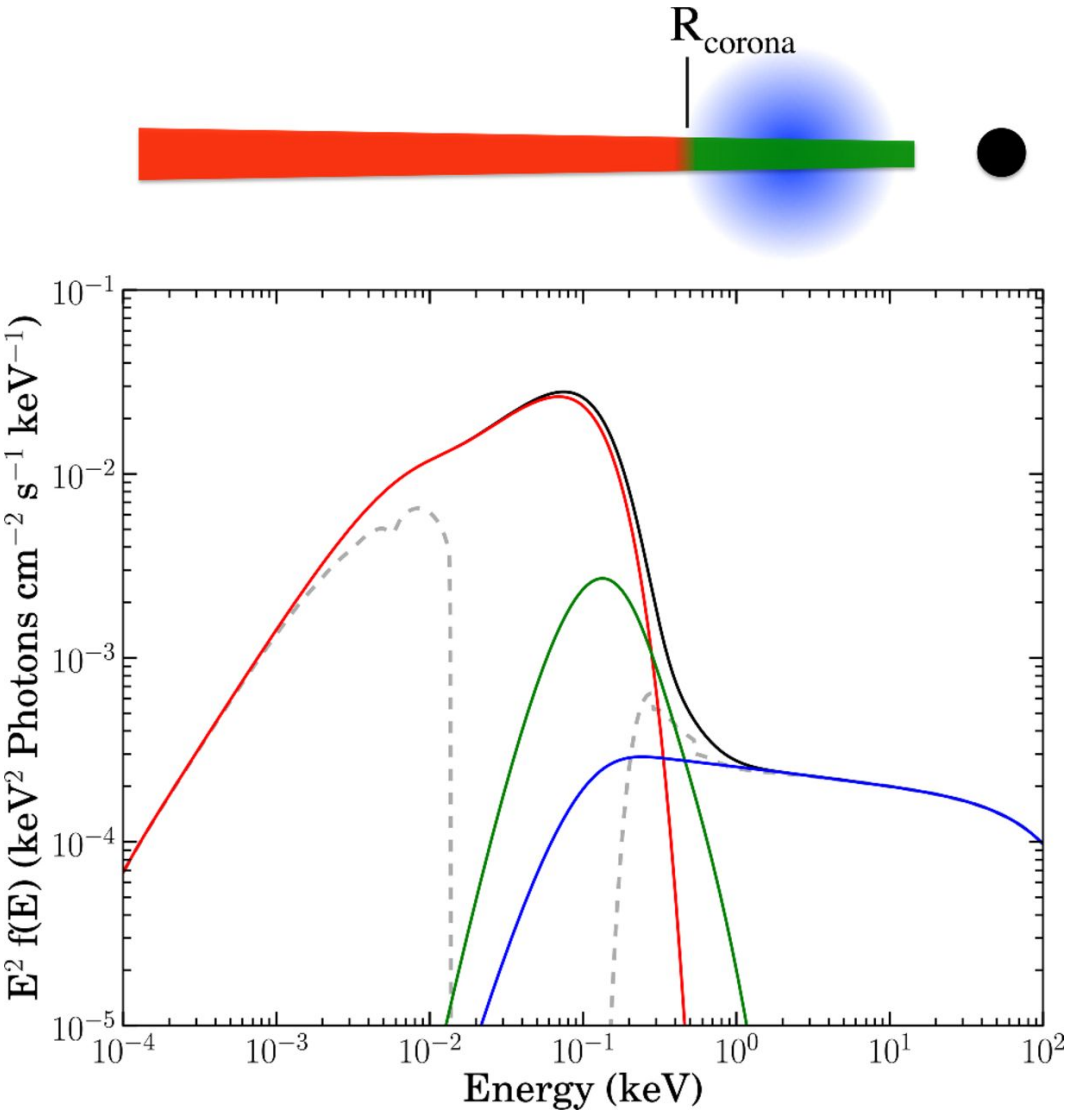

Figure 4.7: Disk dominated SED (Collinson et al., 2015)

brighter', we compared the bolometric luminosities and estimated E(B-V) values for all of the 778 Swift visits. Our E(B-V) value is determined by the $3000-5100$Å slope, so we expect that our estimate of E(B-V) will decrease as L_{bol} increases, if the AGN is in fact becoming "bluer". As shown in Figure 4.8, we see some evidence of this for Mrk 509, but the opposite is seen for NGC 4593, while NGC 4151 and NGC 5548 just show scatter around a central E(B-V) value. The ambiguity we see with the 'bluer when brighter' concept is shared in the literature. Sakata et al. (2010) reports that the spectral shape of the optical wavelengths does not systematically change

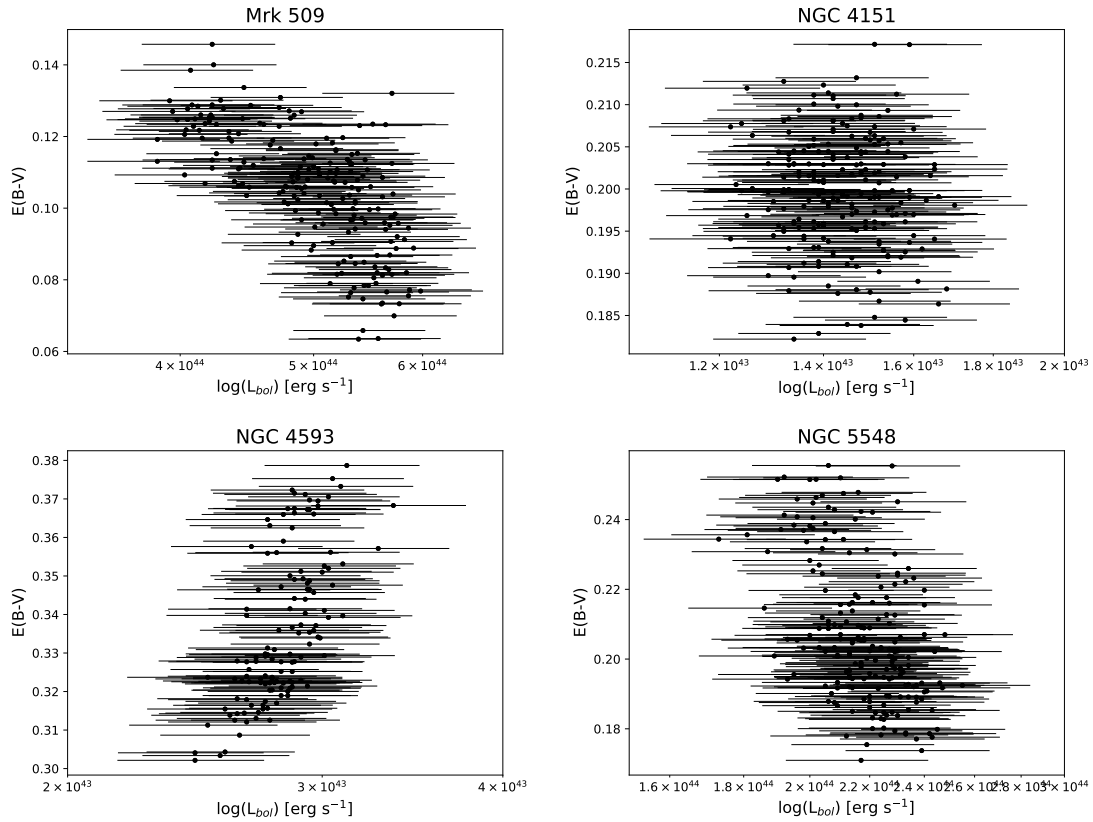

Figure 4.8: Comparison of bolometric luminosity and E(B-V) from the 778 Swift observations of Mrk 509, NGC 4151, NGC 4593, and NGC 5548.

with the change in continuum flux ('no bluer when brighter'). They also report that in quasars the effect of 'bluer when brighter' is only seen to strongly influence the far-UV wavelengths, with a weak influence in the near-UV regime (Sakata et al., 2011). Sukanya et al. (2018) observe the same trends in the far- and near-UV for Seyferts, while Siejkowski & Wierzcholska (2017) reported not seeing any 'bluer when brighter' trend in blazars. Thus, further investigation with simultaneous observations of additional AGNs are needed to determine the conditions under which spectral hardening, or 'bluer when brighter' is most likely to be observed.

4.4 *Variability*

4.4.1 *Uncertainties caused by variability*

In Chapter 3 we explored the variability of four Seyfert 1s on a few weeks to 9 months timescale. By calculating the median values and the 68% confidence intervals of the distributions, we were able to quantify the spread in values derived from the SEDs. As listed in Chapter 3, variability causes a $5-15\%$ spread in L_{bol} values over weeks to months, and a 15% spread in Eddington ratios over the same time period. Combining that with the fractional uncertainties on the measurements, these quantities have a lower limit of 10-20% uncertainty for situations where data are non-simultaneous but collected close in time.

In cases where data are collected over a period of several years, however, as is often the case when archival catalogs are mined, the uncertainty in any value derived from the SED increases significantly. For example, the bolometric luminosity of Mrk 509 decreased by nearly a factor of 2 from the 2006 to 2017 observations, demonstrating that extreme caution is needed when interpreting SEDs that are created by compiling data collected over very long time periods.

4.4.2 *Long−term and Extreme variability*

110 year light curve of NGC 4151 While a few of our targets have observations separated in time by a few years to a decade, we expect that longer-term monitoring of AGNs would show that they exhibit even larger variability than we see here. Oknyanskij et al. (2016) present a historical light curve for NGC 4151 spanning 110 years from 1906 to 2016. The data used to construct the light curve covers the modern history of astronomical technology, including measurements from photographic plates, photoelectric detectors, and CCD observations. From the light curve, Oknyanskij et al. (2016) reported three types of variability — fast variations on the order of days, slow variations on the order of several years, and one very slow component that covered tens of years. It is also clear that variability of up to $1.5-2.0$ magnitudes over ~ 10 years or more is not unusual. The *Swift* observations we examined here were able to probe fast variations, while our comparison

of *XMM* and *Swift* observations were able, in some cases, to probe slow variations. While NGC 4151 is one of the prototypical Seyfert galaxies, very long term light curves for additional AGNs are needed to determine whether the types of variation observed for NGC 4151 are truly typical for all members of its class.

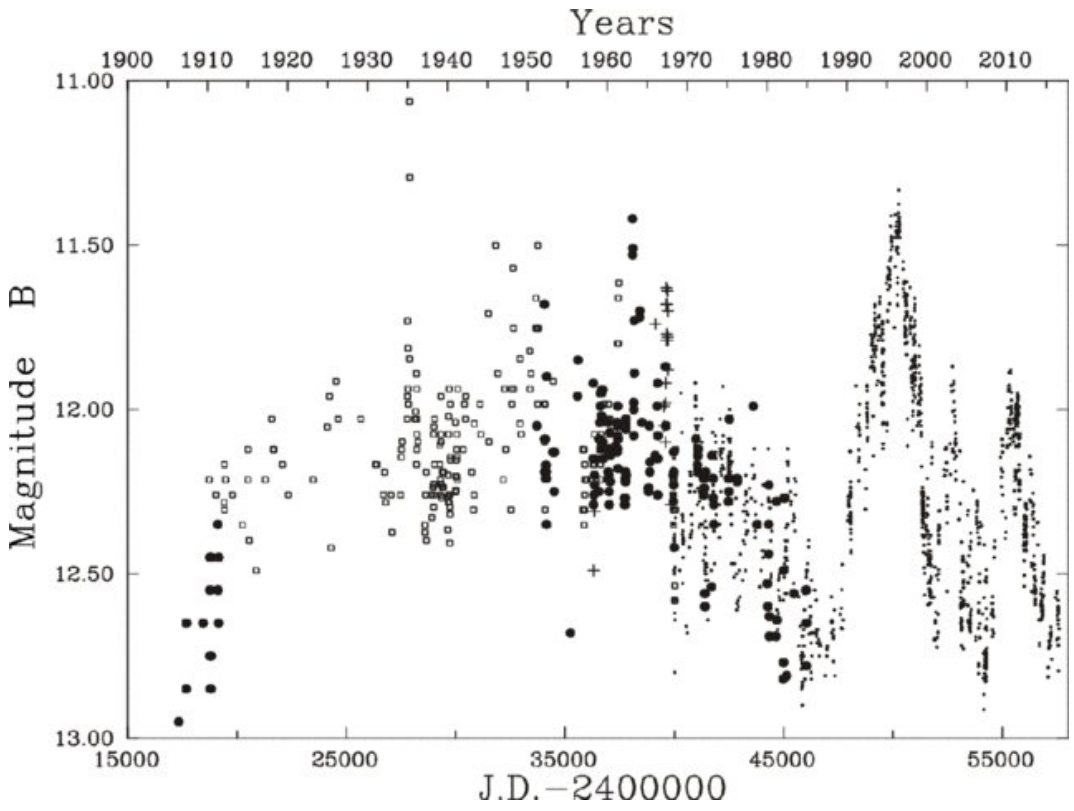

Figure 4.9: 110 year (1906-2016) light curve of NGC 4151. The data come from the following sources: filled circles − Moscow and Odessa plate data; open squares − Harvard/Steward plate data; plus signs − photoelectric data from various sources (see Oknyanskij et al. 2016); dots − photoelectric and CCD data taken at the Crimean Astronomical Station and Weihai Observatory.

Changing look AGNs While 110 years of NGC 4151 observations may display 'typical' Seyfert variability, there are a growing number of AGNs that have been observed to exhibit much more extreme variability, the so-called changing look AGNs (CLAGNS; e.g., Yang et al. 2018; Hon et al. 2020; Lyu et al. 2022). CLAGNs display extreme changes in continuum flux accompanied by the appearance or disappearance of broad line emission over short periods of time. These changes are thought to be caused by either a variable accretion rate or variable obscuration. Mrk 590 is one

of these CLAGNs. Denney et al. (2014) presented observations spanning 40 years which show Mrk 509 has decreased by a factor of 100 from its highest luminosity. The multiwavelength light

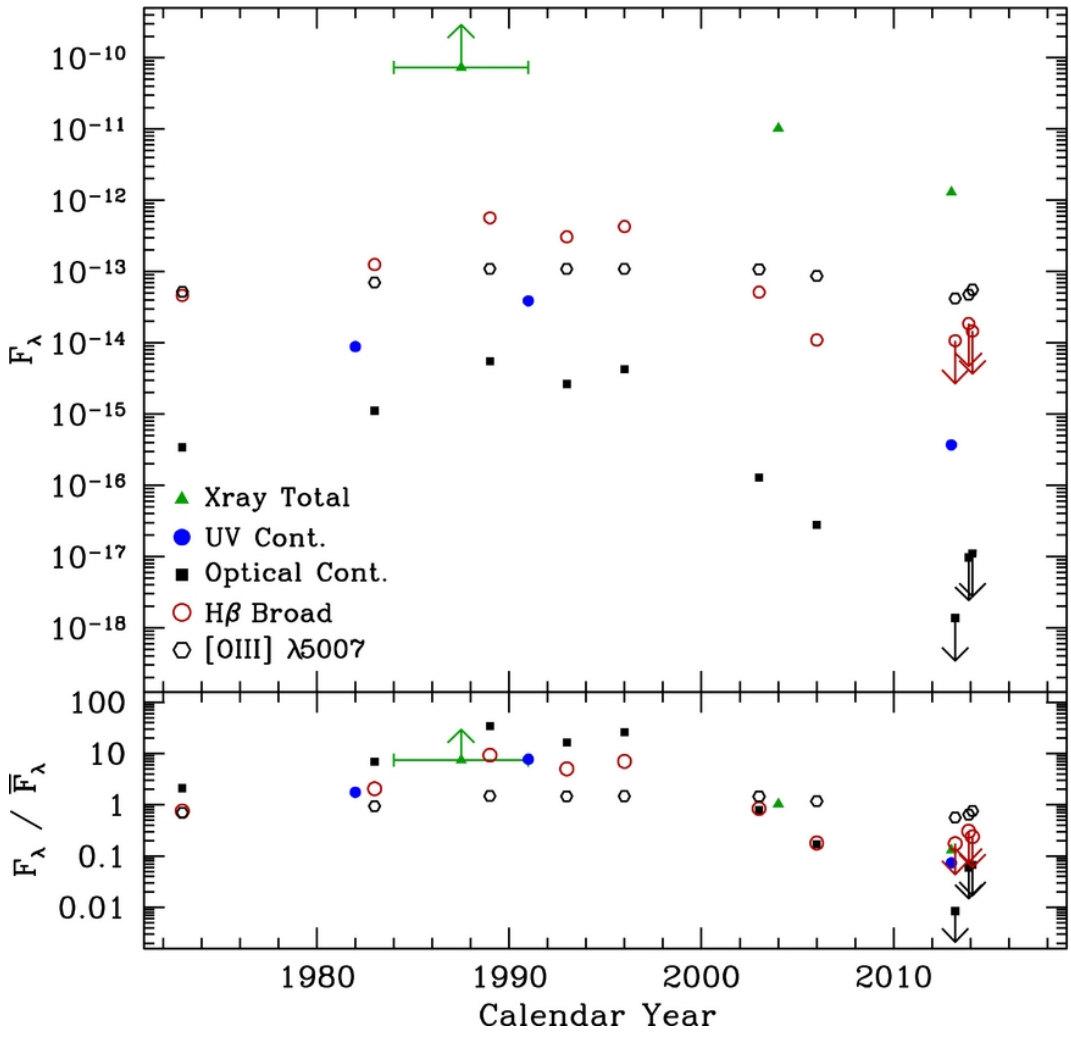

Figure 4.10: The multiwavelength light curves of Mrk 590. The X–rays are shown as green triangles, the UV continuum as blue circle, starlight subtracted optical conintuum as black squares, Hβ line flux as open red circle, and [O III] as open black points.

curve is shown in Figure 4.10 and includes measurements collected between 1973 and 2014. There was a sudden and steep drop off in the mid 1990s that, as of 2014, had not turned back up. The *XMM* observations that we used in this work were taken in 2002 and 2004. We also observe a decrease in all values between the two observations, seeing a 17% decrease in bolometric luminosity between the two dates.

Denney et al. (2014) also report that Mrk 590 exhibited an increase and then disappearance of broad lines in the optical spectrum following the sharp decline of the luminosity. Mathur et al. (2018) report that broad Mg II has recently reappeared, along with the X−ray soft excess that had disappeared. They also report that the current low luminosity state does not seem to be caused by an obscuration event due to the lack of absorption seen in the X−rays. CLAGNs therefore act as cautionary examples of the extreme variability that may occur between observations that occur many years apart, and again make the case for observations of SEDs to prioritize simultaneous or near-simultaneous observations.

4.5 *Jetted and non-jetted AGNs*

We have three radio sources in our sample, 3C 120, 3C 390.3, and PG 1226+023. With their strong radio jets, can we assume that the methods we have applied, and the conclusions that we have drawn, are applicable to these AGNs? It may depend on the system. Gliozzi et al. (2009) report that the short term variability of 3C390.3 was consistent with the variability exhibited by other Seyferts. But 3C390.3 is not a blazar, just a 'regular' radio-loud AGN. Since blazars are known for their rapid, large-amplitude variability (Peterson, 1997), it is less clear that their variability would be similar to the Seyferts that comprise the majority of our sample. Fernandes et al. (2020) presented multiwavelength light curves and polarimetric data of PG1226+023, which is classified as a blazar or flat-spectrum radio source. They observed an anti-correlation in the variability of the V and 15 GHz bands and explain this may be due to part of the accretion disk falling towards the black hole. Such an event may cause the X−ray emission to drop and synchrotron radiation to increase as the infalling material is ejected by the jet. So jets may complicate conclusions we find here regarding variability in AGNs.

Furthermore, depending on the geometry of the system, jets may be a source of relativistic beaming, as is known to be the case for PG 1226+023. It would be worth exploring methods, such as finding measured Doppler factors (e.g., Hovatta et al. 2009; Pei et al. 2020), to estimate non-boosted luminosity values. Alternatively, Kataoka et al. (2011) used spectral templates to explore a 'mixing

parameter' that describes the fractional jet contribution to the observed flux across the SED of several radio-quiet and radio-loud AGNs. Both of these options should be explored going forward.

Chapter 5

SUMMARY AND FUTURE WORK

5.1 *Summary*

The goal of this work was to construct the most accurate multi-wavelength SEDs focusing on the accretion driven flux from the central engine of 23 AGNs with reverberation mapped black hole masses. We utilized simultaneous optical/UV/X–ray observations from *XMM-Newton* and ground-based near-infrared data to explore the emission from the central engine. We removed host galaxy starlight, emission from the BLR and NLR, and accounted for reddening intrinsic to the AGNs. Our SED fitting was carried out with power laws over the NIR/optical/UV and X–rays with the two connected by a power law across the unobservable EUV. We derived bolometric luminosities, Eddington ratios, optical and X–ray bolometric corrections, and $\alpha_{\rm ox}$ values. Additionally, for a sample of 4 galaxies, we analyzed 778 separate visits with Swift covering the optical-UV and X–rays over a period of three weeks to 9 months. With these 778 separate visits, we quantified the effect of variability on SED fits and the quantities derived from them.

We find that correcting for host contribution, line emission, and intrinsic reddening do impact the values derived from SEDs, as do updating mass and distance measurements. In particular, low-luminosity AGNs appear to be more sensitive to the particular methods used in constructing an SED, showing a larger change in derived values of bolometric luminosity and Eddington ratio from one method to another. The importance of accurate distances for nearby AGNs is highlighted by the large changes in derived values for the handful of AGNs in our sample that have distances from Cepheids, Tully-Fisher, and other methods that are more accurate than redshifts. Our derived

quantities are in agreement with the initial results for a single object using the SED fitting code X−CIGALE, although further exploration is needed, especially for the low-luminosity end of our sample. We determined trends of the host-galaxy flux contribution as a function of redshift for the V, B, and U filters through a $6''$ radius aperture, which could be further generalized to provide a useful tool for estimating host-galaxy contributions for large samples. In regards to the emission-line corrections, the addition of a larger range of luminosities among the AGN template spectra considered would allow known complications, like the Baldwin effect, to be taken into account. Due to the enigmatic nature of accretion disks, the treatment of the intrinsic accretion disk slope for reddening corrections may still have room for improvement and requires further exploration.

With the repeated observations provided by *Swift* we determined a lower limit of $10-20\%$ for L_{bol} and 20% for the Eddington ratio uncertainties when the observations for SEDs are collected close in time but not simultaneously. Based on the 110 year historical light curve of NGC 4151 and the existence of changing look AGNs, the uncertainties are expected to increase significantly for observations that are collected more than a few months apart, suggesting that extreme caution is needed when interpreting SEDs that are created by compiling data collected over very long time periods. Furthermore, the variations of $1.5-2.0$ magnitudes over ~ 10 years seen several times in the historical light curve of NGC 4151 and the extreme changes observed in CLAGNs provide clear cautionary evidence against creating AGN SEDs by mining catalogs of observations that were collected over the course of many years. Finally, with 3 radio-loud AGNs in our sample, it may be important to explore options that allow for estimation and correction of relativistic beaming and other contributions from a strong jet, in addition to the corrections explored here for the host galaxy, line emission, and intrinsic reddening.

5.2 *Future Work*

5.2.1 *Corrections*

Host Correction In Chapter 4, we calculated trends for the host contribution to the *XMM* observations through the V, B, and U filters as a function of redshift. Due to the relatively small sample

and the specific aperture size, the usefulness of those relations is limited. However, with the *HST V* images we have in hand, we could relatively easily define a grid of host-galaxy flux contributions in V as a function of redshift for multiple aperture sizes. A first step to improve on the B and U trends would be to explore archival *HST* imaging of objects in our sample through other optical/UV filters and compare the `synphot` and template-derived host galaxy corrections to starlight flux values measured from the images to assess how well they match. After confirming the values or adjusting our methods to ensure agreement, grids could also be made for the B and U bands. This would provide a simple way to estimate host corrections for large samples, allowing for a more accurate assessment of the luminosities and accretion rates.

Line Emission While we considered a 'typical' emission line contribution to each bandpass as a function of redshift, a more accurate approach would be to identify a set of template AGN spectra as a function of luminosity. Then grids of emission-line fluxes as a function of redshift for each passband could be generated, allowing for quick estimates of the emission-line contribution for large samples, or in cases where it is not possible to acquire optical-UV spectra of the AGNs of interest.

Reddening As indicated by the E(B-V) values estimated for our sample, intrinsic reddening is a significant feature in AGNs. And currently, the Milky Way, the LMC, and SMC reddening curves are applied when considering reddening in other galaxies. None of these galaxies are AGNs. With archival data and new targeted observations, it would be interesting to follow the method of Crenshaw et al. (2001) to construct reddening curves for a variety of AGNs, including some 'bare' AGNs. Utilizing a variety of spectra, multiple reddening curves could be created. The reddening curve derived for NGC 3227 was close to the MW curve in the optical, but was more similar to the SMC in the UV. Creating additional reddening curves would provide additional examples that may provide insight into the variety of dust characteristics that may be found across a wide range of environments.

The optical/UV spectra could also be used to further examine the differences between 'bare' AGNs with and without warm absorbers. As shown in Chapter 4, Mrk 509 has a warm absorber and does not show significant reddening in its UV spectrum, but its observed optical/UV slope is somewhat flatter than that of Mrk 110 and Ark 120, as we described in Chapter 2. And when comparing the $\alpha_{\rm opt}$ value of Mrk 509 to NGC 6814 and NGC 3227, which do show significant reddening in their UV spectra, Mrk 509 has a less negative value (Mrk 509: −1.09; NGC 6814: −1.22; NGC 3227:−4.99[1]). It would also be interesting to explore how reddening associated with luke-warm absorbers may differ from any reddening associated with traditional warm absorbers.

5.2.2 *NIR data*

H-band imaging of NGC 5548 has already been collected and, after reduction and modeling with Galfit, may be folded into our analysis, thus providing a better constraint on the red tail of the accretion disk signature in the SED. Additionally, there were objects in the VF09 sample as well as AGNs in the larger RM sample with the appropriate *XMM* observations that we excluded from our sample because they did not have high-resolution NIR images available. The large uncertainties on the quantities derived for NGC5548 in Chapters 2 and 3 demonstrate the importance of constraining the very red end of the accretion disk tail, but there may be additional observations available now. In particular, the Vista Hemisphere Survey may include observations of some of these other AGNs, allowing our sample size to be expanded.

5.2.3 *X−CIGALE*

The preliminary values of the X−CIGALE fit for Ark 120 were in agreement with the values determined in this work. Further investigation with a larger number of objects, and covering a wider range of potential parameter settings, will be needed to explore the effect on derived quantities like the bolometric luminosity and Eddington ratio. Additionally, since Ark 120 is a 'bare' AGN, it would be useful to explore how X−CIGALE handles objects that have varying amounts of reddening

[1]This extreme slope was addressed in Chapter 2

(based on our estimates of their E(B-V) values). This will also provide the opportunity to directly compare the reddening values determined by SKIRTOR to the values we determined using the modified Baron et al. (2016) method.

5.2.4 *Sample expansion*

Our initial sample focused on the *XMM* observations for a sample of objects described by VF09. To begin expanding the sample of AGNs with SEDs from simultaneous optical/UV/X−ray observations, we could go back to where we started, the *XMM* Science Archive. New *XMM* observations are collected every day, and there may be new AGNs with reverberation masses and the requisite observations to be included in our sample. As discussed earlier, the XRT and UVOT are nearly identical to the *XMM* EPIC-MOS and OM instruments, so the *Swift* archive could also be explored. One important reason for expanding the sample would be to include AGNs that cover a larger range of AGN properties. Any new sources would need to be accompanied by accurate black hole masses and have the necessary supporting data to derive well-constrained SEDs and the quantities that are derived from them, in particular bolometric luminosity and Eddington ratio. With expansion of the sample, further methods to account and correct for effects such as jet boosting may become even more important, but could help provide additional insight into the energetics and physics of the central engines of accreting supermassive black holes.

Bibliography

Abramowicz, M. A., Czerny, B., Lasota, J. P., & Szuszkiewicz, E. 1988, The Astrophysical Journal, 332, 646

Alonso-Herrero, A., Quillen, A. C., Rieke, G. H., Ivanov, V. D., & Efstathiou, A. 2003, The Astronomical Journal, 126, 81

Antonucci, R. R. J. & Miller, J. S. 1985, The Astrophysical Journal, 297, 621. doi:10.1086/163559

Antonucci, R. 1993, Annual Reviews of Astronomy and Astrophysics, 31, 473

Arnaud, K., Smith, R., & Siemiginowska, A. 2011, Handbook of X-ray Astronomy

Arnaud, K. A. 1996, in Astronomical Society of the Pacific Conference Series, Vol. 101, Astronomical Data Analysis Software and Systems V, ed. G. H. Jacoby & J. Barnes, 17

Baldwin, J. A. 1977, The Astrophysical Journal, 214, 679

Baron, D., Stern, J., Poznanski, D., & Netzer, H. 2016, The Astrophysical Journal, 832, 8

Batiste, M., Bentz, M. C., Raimundo, S. I., Vestergaard, M., & Onken, C. A. 2017, The Astrophysical Journal, 838, L10

Bentz, M. C., Ferrarese, L., Onken, C. A., Peterson, B. M., & Valluri, M. 2019, The Astrophysical Journal, 885, 161

Bentz, M. C., & Katz, S. 2015, Publications of the Astronomical Society of the Pacific, 127, 67

Bentz, M. C., & Manne-Nicholas, E. 2018, The Astrophysical Journal, 864, 146

Bentz, M. C., Peterson, B. M., Netzer, H., Pogge, R. W., & Vestergaard, M. 2009, The Astrophysical Journal, 697, 160

Bentz, M. C., Peterson, B. M., Pogge, R. W., Vestergaard, M., & Onken, C. A. 2006, The Astrophysical Journal, 644, 133

Bentz, M. C., Denney, K. D., Grier, C. J., et al. 2013, The Astrophysical Journal, 767, 149

Blackburn, J. K. 1995, in Astronomical Society of the Pacific Conference Series, Vol. 77, Astronomical Data Analysis Software and Systems IV, ed. R. A. Shaw, H. E. Payne, & J. J. E. Hayes, 367

Boquien, M., Burgarella, D., Roehlly, Y., et al. 2019, Astronomy and Astrophysics, 622, A103

Brown, M. J. I., Duncan, K. J., Landt, H., et al. 2019, Monthly Notices of the Royal Astronomical Society, 489, 3351

Cackett, E. M., Bentz, M. C., & Kara, E. 2021, iScience, 24, 102557

Cackett, E. M., Gelbord, J., Li, Y.-R., et al. 2020, The Astrophysical Journal, 896, 1

Calzetti, D., Kinney, A. L., & Storchi-Bergmann, T. 1994, The Astrophysical Journal, 429, 582

Chandrasekhar, S. 1931, The Astrophysical Journal, 74, 81

Colina, L., Bohlin, R., & Castelli, F. 1996, Instrument Science Report CAL/SCS-008, Space Telescope Science Institute

Collin, S., Kawaguchi, T., Peterson, B. M., et al. 2006, Astronomy and Astrophysics, 456, 75. doi:10.1051/0004-6361:20064878

Collinson, J. S., Ward, M. J., Done, C., et al. 2015, Monthly Notices of the Royal Astronomical Society, 449, 2174

Collinson, J. S., Ward, M. J., Landt, H., et al. 2017, Monthly Notices of the Royal Astronomical Society, 465, 358

Crenshaw, D. M., Kraemer, S. B., Boggess, A., et al. 1999, The Astrophysical Journal, 516, 750

Crenshaw, D. M., Kraemer, S. B., Bruhweiler, F. C., & Ruiz, J. R. 2001, The Astrophysical Journal, 555, 633

Czerny, B., & Elvis, M. 1987, The Astrophysical Journal, 321, 305

De Marco, B., Adhikari, T. P., Ponti, G., et al. 2020, Astronomy and Astrophysics, 634, A65

Denney, K. D., Bentz, M. C., Peterson, B. M., et al. 2006, The Astrophysical Journal, 653, 152

Denney, K. D., De Rosa, G., Croxall, K., et al. 2014, The Astrophysical Journal, 796, 134

Du, P., Wang, J.-M., & Zhang, Z.-X. 2017, The Astrophysical Journal Letters, 840, L6. doi:10.3847/2041-8213/aa6d7b

Edelson, R., Gelbord, J., Cackett, E., et al. 2019, The Astrophysical Journal, 870, 123

—. 2020, VizieR Online Data Catalog, J/ApJ/870/123

Elitzur, M. 2006, New Astronomy Reviews, 50, 728

Elmer, E., Almaini, O., Merrifield, M., et al. 2020, Monthly Notices of the Royal Astronomical Society, 493, 3026

Elvis, M., Maccacaro, T., Wilson, A. S., et al. 1978, Monthly Notices of the Royal Astronomical Society, 183, 129

Elvis, M., Wilkes, B. J., McDowell, J. C., et al. 1994, The Astrophysical Journal Supplement Series, 95, 1

Elvis, M., Hao, H., Civano, F., et al. 2012, The Astrophysical Journal, 759, 6

Fath, E. A. 1909, Publications of the Astronomical Society of the Pacific, 21, 138

Fausnaugh, M. M., Peterson, B. M., Starkey, D. A., Horne, K., & , t. A. S. C. 2017, Frontiers in Astronomy and Space Sciences, 4

Fernandes, S., Patiño-Álvarez, V. M., Chavushyan, V., Schlegel, E. M., & Valdés, J. R. 2020, Monthly Notices of the Royal Astronomical Society, 497, 2066

Finkelstein, D. 1958, Phys. Rev., 110, 965

Ganeshalingam, M., Li, W., & Filippenko, A. V. 2013, Monthly Notices of the Royal Astronomical Society, 433, 2240

García, J. A., Kara, E., Walton, D., et al. 2019, The Astrophysical Journal, 871, 88

Gaskell, C. M., & Benker, A. J. 2007, arXiv e-prints, arXiv:0711.1013. https://arxiv.org/abs/0711.1013

Gaskell, C. M., & Klimek, E. S. 2003, Astronomical and Astrophysical Transactions, 22, 661

Giacconi, R., Gursky, H., Paolini, F. R., & Rossi, B. B. 1962, Phys. Rev. Lett., 9, 439

Glikman, E., Helfand, D. J., & White, R. L. 2006, The Astrophysical Journal, 640, 579

Gliozzi, M., Papadakis, I. E., Eracleous, M., et al. 2009, The Astrophysical Journal, 703, 1021

Gliozzi, M., & Williams, J. K. 2020, Monthly Notices of the Royal Astronomical Society, 491, 532

Grafton-Waters, S., Branduardi-Raymont, G., Mehdipour, M., et al. 2020, Astronomy and Astrophysics, 633, A62

Grier, C. J., Peterson, B. M., Pogge, R. W., et al. 2012, The Astrophysical Journal, 755, 60

Haardt, F., & Maraschi, L. 1991, The Astrophysical Journal Letters, 380, L51

Hall, P. B., Sarrouh, G. T., & Horne, K. 2018, The Astrophysical Journal, 854, 93

Heckman, T. M., & Best, P. N. 2014, Annual Reviews of Astronomy and Astrophysics, 52, 589

Heisler, C. A., Lumsden, S. L., & Bailey, J. A. 1997, Nature, 385, 700. doi:10.1038/385700a0

Holmberg, E. 1958, Meddelanden fran Lunds Astronomiska Observatorium Serie II, 136, 1

Hon, W. J., Webster, R., & Wolf, C. 2020, Monthly Notices of the Royal Astronomical Society, 497, 192

Hönig, S. F. 2019, The Astrophysical Journal, 884, 171

Hovatta, T., Valtaoja, E., Tornikoski, M., & Lähteenmäki, A. 2009, Astronomy and Astrophysics, 494, 527

Hubble, E. P. 1926, The Astrophysical Journal, 64, 321

—. 1929, The Astrophysical Journal, 69, 103

Jaffarian, G. W. & Gaskell, C. M. 2020, Monthly Notices of the Royal Astronomical Society, 493, 930. doi:10.1093/mnras/staa262

Jansky, K. 1935, Proceedings of the Institute of Radio Engineers, 23, 1158

Jansky, K. G. 1933, Nature, 132, 66

Kaastra, J. S., Detmers, R. G., Mehdipour, M., et al. 2012, Astronomy and Astrophysics, 539, A117

Kant, I. 1755, Allgemeine Naturgeschichte und Theorie des Himmels

Kaspi, S., Smith, P. S., Netzer, H., et al. 2000, The Astrophysical Journal, 533, 631

Kataoka, J., Stawarz, Ł., Takahashi, Y., et al. 2011, The Astrophysical Journal, 740, 29

Kerr, R. P. 1963, Phys. Rev. Lett., 11, 237

Kilerci Eser, E., & Vestergaard, M. 2018, Monthly Notices of the Royal Astronomical Society, 474, 1590

Kinney, A. L., Calzetti, D., Bohlin, R. C., et al. 1996, The Astrophysical Journal, 467, 38

Kishimoto, M., Hönig, S. F., Beckert, T., & Weigelt, G. 2007, Astronomy and Astrophysics, 476, 713

Koshida, S., Yoshii, Y., Kobayashi, Y., et al. 2017, The Astrophysical Journal, 842, L13

Kraemer, S. B., & Crenshaw, D. M. 1999, in American Astronomical Society Meeting Abstracts, Vol. 195, American Astronomical Society Meeting Abstracts, 115.05

Kriss, G. A., Peterson, B. M., Crenshaw, D. M., & Zheng, W. 2000, The Astrophysical Journal, 535, 58

Kriss, G. A., De Rosa, G., Ely, J., et al. 2019, The Astrophysical Journal, 881, 153

Krist, J. 1993, in Astronomical Society of the Pacific Conference Series, Vol. 52, Astronomical Data Analysis Software and Systems II, ed. R. J. Hanisch, R. J. V. Brissenden, & J. Barnes, 536

Laha, S., Guainazzi, M., Chakravorty, S., Dewangan, G. C., & Kembhavi, A. K. 2016, Monthly Notices of the Royal Astronomical Society, 457, 3896

Laha, S., Guainazzi, M., Dewangan, G. C., Chakravorty, S., & Kembhavi, A. K. 2014, Monthly Notices of the Royal Astronomical Society, 441, 2613

Leavitt, H. S. 1908, Annals of Harvard College Observatory, 60, 87

Leavitt, H. S., & Pickering, E. C. 1912, Harvard College Observatory Circular, 173, 1

Leighly, K., Kunieda, H., Tsusaka, Y., Awaki, H., & Tsuruta, S. 1994, The Astrophysical Journal, 421, 69

Liu, H., Parker, M. L., Jiang, J., et al. 2021, Monthly Notices of the Royal Astronomical Society, 506, 5190

Lynden-Bell, D. 1969, Nature, 223, 690

Lyu, B., Wu, Q., Yan, Z., Yu, W., & Liu, H. 2022, The Astrophysical Journal, 927, 227

Lyu, J., & Rieke, G. H. 2021, The Astrophysical Journal, 912, 126

Marchesi, S., Civano, F., Elvis, M., et al. 2019, VizieR Online Data Catalog, J/ApJ/817/34

Mason, K. O., Breeveld, A., Much, R., et al. 2001, Astronomy and Astrophysics, 365, L36

Mathur, S., Denney, K. D., Gupta, A., et al. 2018, The Astrophysical Journal, 866, 123

McCracken, H. J., Milvang-Jensen, B., Dunlop, J., et al. 2012, Astronomy and Astrophysics, 544, A156

McMahon, R. G., Banerji, M., Gonzalez, E., et al. 2013, The Messenger, 154, 35

Meena, B., Crenshaw, D. M., Schmitt, H. R., et al. 2021, The Astrophysical Journal, 916, 31

Mehdipour, M., Kriss, G. A., Brenneman, L. W., et al. 2022, The Astrophysical Journal, 925, 84

Michell, J. 1784, Philosophical Transactions of the Royal Society of London Series I, 74, 35

Minkowski, R. 1960, The Astrophysical Journal, 132, 908

National Optical Astronomy Observatories. 1999, IRAF: Image Reduction and Analysis Facility. http://ascl.net/9911.002

Newman, E. T., Couch, E., Chinnapared, K., et al. 1965, Journal of Mathematical Physics, 6, 918

Nordström, G. 1918, Koninklijke Nederlandse Akademie van Wetenschappen Proceedings Series B Physical Sciences, 20, 1238

Ochsenbein, F., Bauer, P., & Marcout, J. 2000, , 143, 23. doi:10.1051/aas:2000169

Oknyanskij, V. L., Metlova, N. V., Huseynov, N. A., Guo, D.-F., & Lyuty, V. M. 2016, Odessa Astronomical Publications, 29, 95

Oppenheimer, J. R., & Snyder, H. 1939, Phys. Rev., 56, 455

Oppenheimer, J. R., & Volkoff, G. M. 1939, Phys. Rev., 55, 374

Osterbrock, D. E. 1978, Proceedings of the National Academy of Science, 75, 540

Padovani, P., Alexander, D. M., Assef, R. J., et al. 2017, The Astronomy and Astrophysics Review, 25, 2

Pei, Y. C. 1992, The Astrophysical Journal, 395, 130

Pei, Z., Fan, J., Yang, J., & Bastieri, D. 2020, Publications of the Astronomical Society of Australia, 37, e043

Peng, C. Y., Ho, L. C., Impey, C. D., & Rix, H.-W. 2002, The Astronomical Journal, 124, 266

Peng, C. Y., Ho, L. C., Impey, C. D., & Rix, H.-W. 2010, The Astronomical Journal, 139, 2097

Peterson, B. M. 1997, An Introduction to Active Galactic Nuclei

Peterson, B. M., Ferrarese, L., Gilbert, K. M., et al. 2004, The Astrophysical Journal, 613, 682

Porquet, D., Reeves, J. N., Grosso, N., Braito, V., & Lobban, A. 2021, Astronomy and Astrophysics, 654, A89

Proga, D. 2005, The Astrophysical Journal Letters, 630, L9

Rees, M. J. 1984, Annual Review of Astronomy and Astrophysics, 22, 471

Reeves, J. N., Porquet, D., Braito, V., Grosso, N., & Lobban, A. 2021, Astronomy and Astrophysics, 649, L3

Reeves, J. N., Porquet, D., Braito, V., et al. 2016, The Astrophysical Journal, 828, 98

Reissner, H. 1916, Annalen der Physik, 355, 106

Revalski, M., Meena, B., Martinez, F., et al. 2021, The Astrophysical Journal, 910, 139

Richards, G. T., Lacy, M., Storrie-Lombardi, L. J., et al. 2006, The Astrophysical Journal Supplement Series, 166, 470

Robinson, J. H., Bentz, M. C., Courtois, H. M., et al. 2021, The Astrophysical Journal, 912, 160

Sánchez, P., Lira, P., Cartier, R., et al. 2017, The Astrophysical Journal, 849, 110

Sakata, Y., Minezaki, T., Yoshii, Y., et al. 2010, The Astrophysical Journal, 711, 461. doi:10.1088/0004-637X/711/1/461

Sakata, Y., Morokuma, T., Minezaki, T., et al. 2011, The Astrophysical Journal, 731, 50. doi:10.1088/0004-637X/731/1/50

Sanders, D. B., Phinney, E. S., Neugebauer, G., Soifer, B. T., & Matthews, K. 1989, The Astrophysical Journal, 347, 29

Schlafly, E. F., & Finkbeiner, D. P. 2011, The Astrophysical Journal, 737, 103

Schlegel, D. J., Finkbeiner, D. P., & Davis, M. 1998, The Astrophysical Journal, 500, 525

Schmidt, M. 1963, Nature, 197, 1040

Sersic, J. L. 1968, Atlas de Galaxias Australes

Seyfert, C. K. 1943, The Astrophysical Journal, 97, 28

Shakura, N. I., & Sunyaev, R. A. 1973, Astronomy and Astrophysics, 500, 33

Shapley, H., & Curtis, H. D. 1921, Bulletin of the National Research Council, 2, 171

Shields, G. A. 1999, Publications of the Astronomical Society of the Pacific, 111, 661

Siejkowski, H. & Wierzcholska, A. 2017, Monthly Notices of the Royal Astronomical Society, 468, 426. doi:10.1093/mnras/stx495

Shang, Z., Brotherton, M. S., Green, R. F., et al. 2005, The Astrophysical Journal, 619, 41. doi:10.1086/426134

Slipher, V. M. 1917, Lowell Observatory Bulletin, 3, 59

Smith, H. J., & Hoffleit, D. 1963, Nature, 198, 650

Stalevski, M., Ricci, C., Ueda, Y., et al. 2016, Monthly Notices of the Royal Astronomical Society, 458, 2288

Steffen, A. T., Strateva, I., Brandt, W. N., et al. 2006, The Astronomical Journal, 131, 2826

Strateva, I. V., Brandt, W. N., Schneider, D. P., Vanden Berk, D. G., & Vignali, C. 2005, The Astronomical Journal, 130, 387

Sukanya, N., Stalin, C. S., Joseph, P., et al. 2018, Journal of Astrophysics and Astronomy, 39, 65. doi:10.1007/s12036-018-9556-z

Telfer, R. C., Zheng, W., Kriss, G. A., et al. 2002, The Astrophysical Journal, 565, 773. doi:10.1086/324689

Tonry, J. L., Dressler, A., Blakeslee, J. P., et al. 2001, The Astrophysical Journal, 546, 681

Tortosa, A., Bianchi, S., Marinucci, A., et al. 2018, Monthly Notices of the Royal Astronomical Society, 473, 3104

Tripathi, S., McGrath, K. M., Gallo, L. C., et al. 2020, Monthly Notices of the Royal Astronomical Society, 499, 1266

Tully, R. B., & Fisher, J. R. 1977, Astronomy and Astrophysics, 54, 661

Tully, R. B., & Pierce, M. J. 2000, The Astrophysical Journal, 533, 744

Turner, T. J., Done, C., Mushotzky, R., Madejski, G., & Kunieda, H. 1992, The Astrophysical Journal, 391, 102

Ulrich, M.-H., Maraschi, L., & Urry, C. M. 1997, Annual Reviews of Astronomy and Astrophysics, 35, 445

Vanden Berk, D. E., Richards, G. T., Bauer, A., et al. 2001, The Astronomical Journal, 122, 549

Vasudevan, R. V., & Fabian, A. C. 2009, Monthly Notices of the Royal Astronomical Society, 392, 1124

@MISCvizier, author = Ochsenbein F. et. al title = " The VizieR database of astronomical catalogues " doi = 10.26093/cds/vizier,

Walton, D. J., Nardini, E., Fabian, A. C., Gallo, L. C., & Reis, R. C. 2013, Monthly Notices of the Royal Astronomical Society, 428, 2901

Wills, B. J., Netzer, H., & Wills, D. 1985, The Astrophysical Journal, 288, 94

Wilson, A. S., & Colbert, E. J. M. 1995, The Astrophysical Journal, 438, 62

Yang, G., Boquien, M., Buat, V., et al. 2020, Monthly Notices of the Royal Astronomical Society, 491, 740

Yang, Q., Wu, X.-B., Fan, X., et al. 2018, The Astrophysical Journal, 862, 109

Yuan, W., Fausnaugh, M. M., Hoffmann, S. L., et al. 2020, The Astrophysical Journal, 902, 26

Yuan, W., Macri, L. M., Peterson, B. M., et al. 2021, The Astrophysical Journal, 913, 3

Appendix A

SED PLOTS

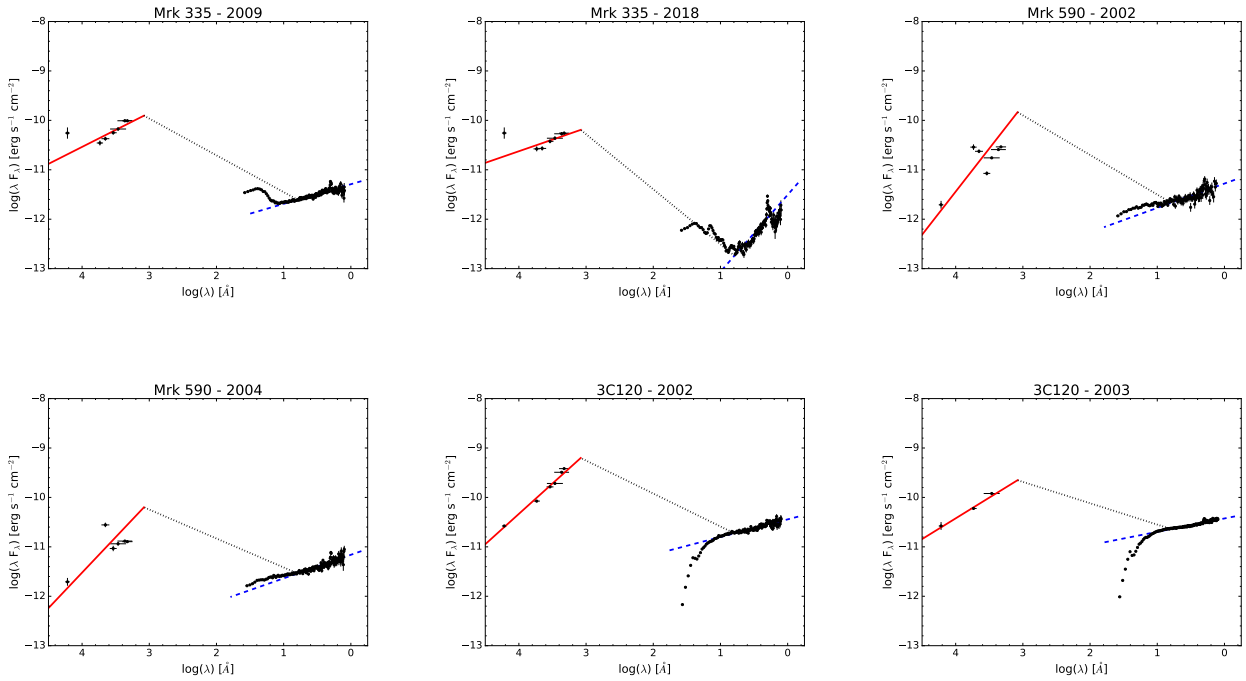

Figure A.1: SEDs with simultaneous optical/UV/X−ray observations from *XMM-Newton*. The solid red line is the power law fit from 16500 − 1200 Å, the blue dashed line is the power law fit from 2 − 10 keV, and the black dotted line connects the two regions.

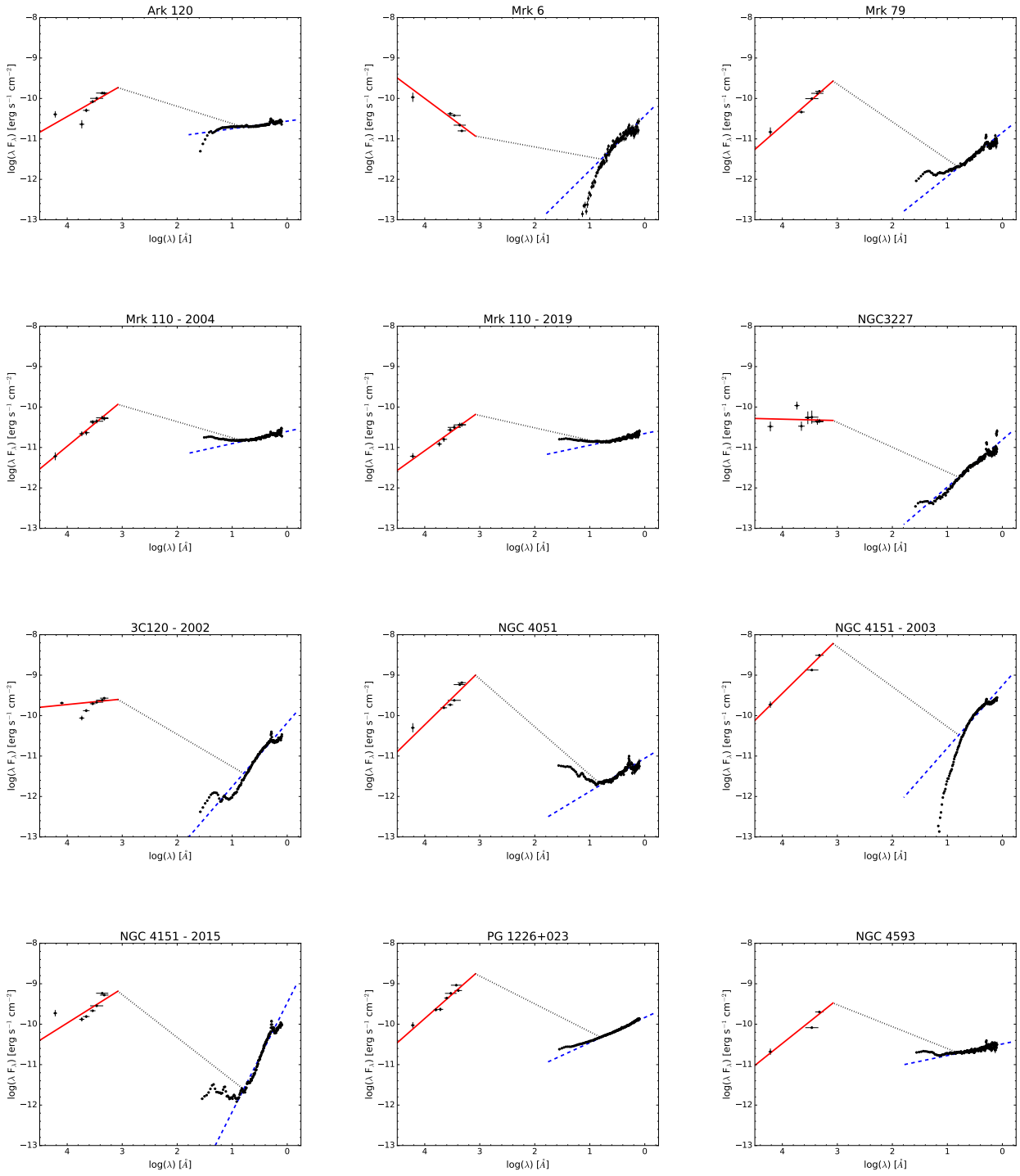

Figure A.2: SEDs with simultaneous optical/UV/X–ray observations from *XMM-Newton*. The solid red line is the power law fit from 16500 − 1200 Å, the blue dashed line is the power law fit from 2 − 10 keV, and the black dotted line connects the two regions.

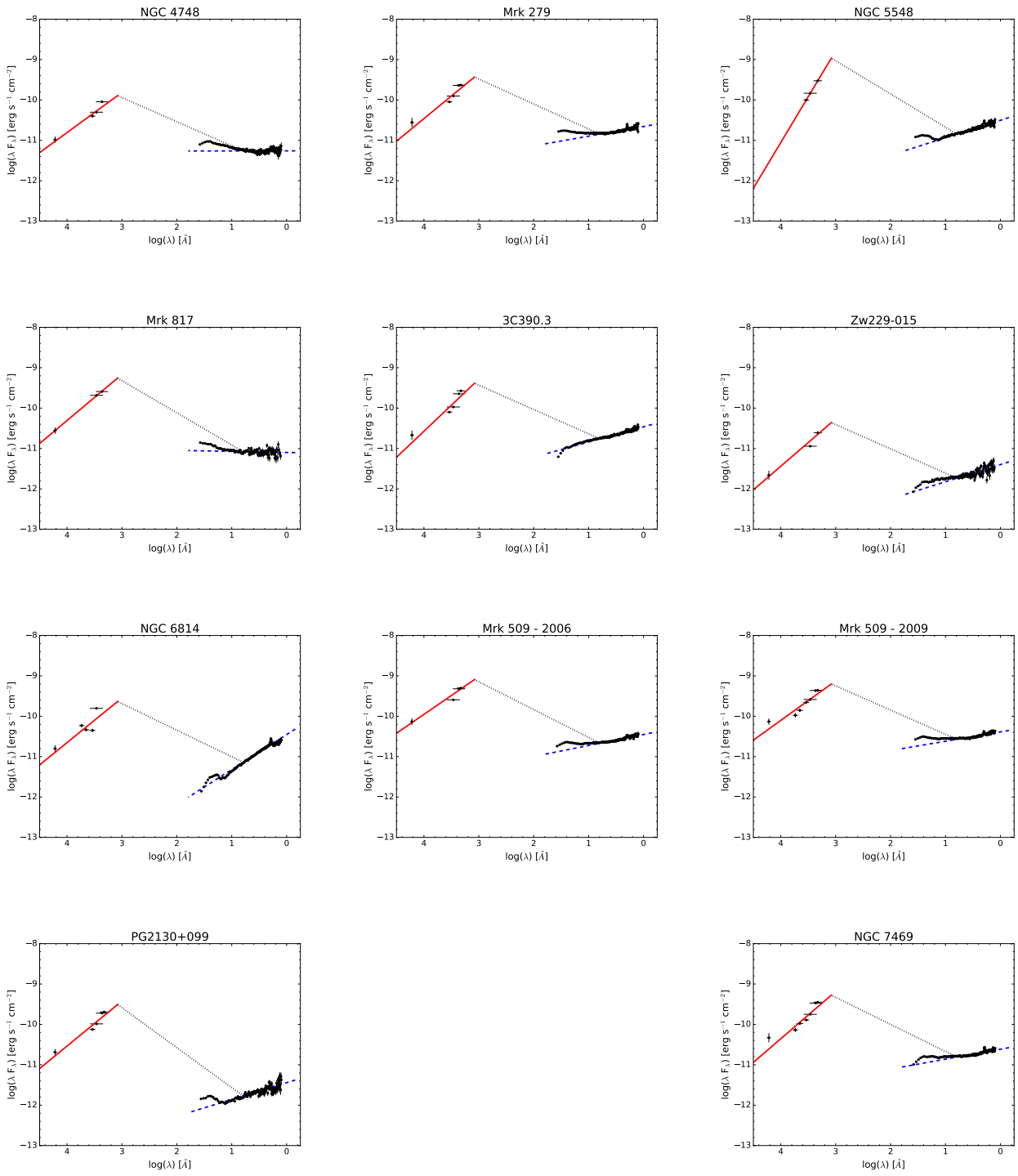

Figure A.3: SEDs with simultaneous optical/UV/X–ray observations from *XMM-Newton*. The solid red line is the power law fit from 16500 − 1200 Å, the blue dashed line is the power law fit from 2 − 10 keV, and the black dotted line connects the two regions.

Appendix B

X-CIGALE FIT PARAMETERS

```
# Configuration of the SED creation modules.
[sed_modules_params]
 [[sfhdelayed]]
# e-folding time of the main stellar population model in Myr.
    tau_main = 2000.0
# Age of the main stellar population in the galaxy in Myr.
# The precision is 1 Myr.
    age_main = 5000
# e-folding time of the late starburst population model in Myr.
    tau_burst = 50.0
# Age of the late burst in Myr. The precision is 1 Myr.
    age_burst = 20
# Mass fraction of the late burst population.
    f_burst = 0.0
# Multiplicative factor controlling the SFR if normalise is False.
# For instance without any burst: SFR(t)=sfr_A×t×exp(-t/)/²
    sfr_A = 1.0
# Normalise the SFH to produce one solar mass.
    normalise = True

[[bc03]]
```

```
# Initial mass function: 0 (Salpeter) or 1 (Chabrier).
    imf = 0
# Metalicity. Possible values are: 0.0001, 0.0004, 0.004, 0.008,
# 0.02, 0.05.
    metallicity = 0.02
# Age [Myr] of the separation between the young and the old star
# populations. The default value in 10^7 years (10 Myr).
# Set to 0 not to differentiate ages (only an old population).
    separation_age = 10

[[nebular]]
# Ionisation parameter
    logU = -2.0
# Fraction of Lyman continuum photons escaping the galaxy
    f_esc = 0.0
# Fraction of Lyman continuum photons absorbed by dust
    f_dust = 0.5
# Line width in km/s
    lines_width = 300.0
# Include nebular emission.
    emission = True

[[dustatt_calzleit]]
# E(B-V)*, the colour excess of the stellar continuum light
# for the young population.
    E_BVs_young = 0.3
# Reduction factor for the E(B-V)* of the old population compared
# to the young one (<1).
    E_BVs_old_factor = 1.0
```

```
# Central wavelength of the UV bump in nm.
    uv_bump_wavelength = 217.5
# Width (FWHM) of the UV bump in nm.
    uv_bump_width = 35.0
# Amplitude of the UV bump. For the Milky Way: 3.
    uv_bump_amplitude = 2.0
# Slope delta of the power law modifying the attenuation curve.
    powerlaw_slope = 0.0
# Filters for which the attenuation will be computed and
# added to the SED information dictionary. You can give
# several filter names separated by a & (don't use commas).
    filters = XMMV & XMMB & XMMU & XMMW1 & XMMM2 & XMMW2

[[dale2014]]
# AGN fraction. It is not recommended to combine this AGN emission
# with the of Fritz et al. (2006) or SKIRTOR models.
    fracAGN = 0.0
# Alpha slope. Possible values are: 0.0625, 0.1250, 0.1875, 0.2500,
# 0.3125, 0.3750, 0.4375, 0.5000, 0.5625, 0.6250, 0.6875, 0.7500,
# 0.8125, 0.8750, 0.9375, 1.0000, 1.0625, 1.1250, 1.1875, 1.2500,
# 1.3125, 1.3750, 1.4375, 1.5000, 1.5625, 1.6250, 1.6875, 1.7500,
# 1.8125, 1.8750, 1.9375, 2.0000, 2.0625, 2.1250, 2.1875, 2.2500,
# 2.3125, 2.3750, 2.4375, 2.5000, 2.5625, 2.6250, 2.6875, 2.7500,
# 2.8125, 2.8750, 2.9375, 3.0000, 3.0625, 3.1250, 3.1875, 3.2500,
# 3.3125, 3.3750, 3.4375, 3.5000, 3.5625, 3.6250, 3.6875, 3.7500,
# 3.8125, 3.8750, 3.9375, 4.0000
    alpha = 2.0

[[skirtor2016]]
```

```
# Average edge-on optical depth at 9.7 micron; the actual one along
# the line of sight may vary depending on the clumps distribution.
# Possible values are: 3, 5, 7, 9, and 11.
    t = 7
# Power-law exponent that sets radial gradient of dust density.
# Possible values are: 0., 0.5, 1., and 1.5.
    pl = 0.5
# Index that sets dust density gradient with polar angle.
# Possible values are:  0., 0.5, 1., and 1.5.
    q = 1.5
# Angle measured between the equatorial plan and edge of the torus.
# Half-opening angle of the dust-free cone is 90°-oa. Possible
# values are: 10, 20, 30, 40, 50, 60, 70, and 80
    oa = 40
# Ratio of outer to inner radius, R_out/R_in.Possible values are:
# 10, 20, and 30
    R = 20
# fraction of total dust mass inside clumps. 0.97 means 97% of total
# mass is inside the clumps and 3% in the interclump dust. Possible
# values are: 0.97.
    Mcl = 0.97
# inclination, i.e. viewing angle, position of the instrument w.r.t.
# the AGN axis. i=[0, 90°-oa): face-on, type 1 view; i=[90°-oa, 90°]:
# edge-on, type 2 view. Possible values are: 0, 10, 20, 30, 40,
# 50, 60, 70, 80, and 90.
    i = 30
# AGN fraction.
    fracAGN = 0.5
# The extinction law of polar dust: 0 (SMC), 1 (Calzetti 2000), or 2
```

```
# (Gaskell et al. 2004)
    law = 1
# E(B-V) for extinction in polar direction
    EBV = 0.1
# Temperature of the polar dust in K
    temperature = 100.0
# Emissivity index of the polar dust
    emissivity = 1.6

[[xray]]
# The photon index (Gamma) of AGN intrinsic X-ray spectrum.
    gam = 1.8
# Maximum deviation of alpha_ox from the empirical
# alpha_ox-Lnu_2500A relation (Just et al. 2007), i.e.
# |alpha_ox-alpha_ox(Lnu_2500A)| <= max_dev_alpha_ox.
# alpha_ox is the power-law slope connecting L_nu at rest-frame
# 2500 A and 2 keV, defined as alpha_ox =
# 0.3838*log(Lnu_2keV/Lnu_2500A), which is often modeled as
# a function of Lnu_2500A. The # alpha_ox-Lnu_2500A relation has a
# 1-sigma scatter of ~ 0.1.
    max_dev_alpha_ox = 0.2
# The photon index of AGN low-mass X-ray binaries.
    gam_lmxb = 1.56
# The photon index of AGN high-mass X-ray binaries.
    gam_hmxb = 2.0

[[redshifting]]
# Redshift of the objects. Leave empty to use the redshifts from the
# input file.
```

```
redshift = 0.03271
```